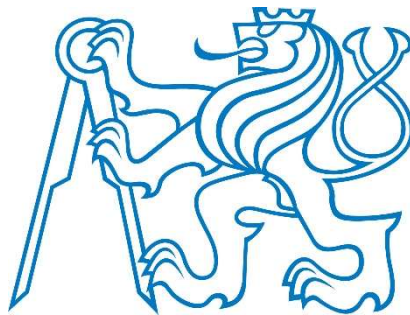


CZECH TECHNICAL UNIVERSITY IN PRAGUE

Faculty of Mechanical Engineering

Department of Instrumentation and Control Engineering



MASTER THESIS

**NUMERICAL SIMULATION OF THE EYE
STRUCTURE UNDER ENDOSCOPIC
TREATMENT**

Jarno Mastomäki

2020

Statement

I declare that I have worked out this thesis independently assuming, that the results of the thesis can also be used at the discretion of the supervisor of the thesis as its co-author. I also agree with the potential publication of the results of the thesis or of its substantial part, provided I will be listed as the co-author.

Prague, 2020

.....
Signature

Acknowledgements

I would like to express my sincere gratitude to my advisor, Doc. Ing. Jan Hošek PhD who advised and motivated me during my research work. Most importantly, for bringing up the topic and had been there always for those invaluable discussions. His enthusiasm for his work act as a source of inspiration for me. I have been fortunate to have a supervisor who cared so much about my work and was there for my questions so promptly.

Special thanks for,

Ing. Šárka Němcová PhD who works tirelessly for the best of the students and who willingly provided all the information I needed for my thesis. I also want to thank Ing. Daniel Hadraba PhD for helping me with the experimental setup and his knowledge of testing biological samples.

I also want to thank following individuals,

MUDr. Martina Nemčoková, MUDr. Martin Penčák, Ivan Kašík PhD, MSc Ilkka Mikkonen, Ing. Josef Šepitka and doctoral students Ing. Petr Zvolan and Ing. Zdenek Krtous for providing their expertise to my use.

Lastly, I want to thank all my school and work friends for supporting me during my studies. Without you, I would not have reached my goals.

Abstract

This thesis work was assigned by Czech Technical University in Prague, further CTU. It is a leading technical University in the Czech Republic, located in the capital of the country, Prague.

The purpose of this study was to investigate the stresses and displacements in the human eye and instrument during endoscopy. The results of the calculations will be used on developing the instrument for ophthalmic operations. While developing a new, more compact instrument with a better resolution image, a new problem aroused from the endurance point of view. The instrument might be not robust enough to handle some extreme conditions while being operated freehand by the surgeon. Therefore, there was a need to study how much the critical parts can hold a load during the operation in order to optimise the design without having to compromise between the wanted qualities and strength.

During the ophthalmic operation, the eye is penetrated by a needle-like endoscope to visually study the inner parts of the eye. The surgeon needs to move the endoscope inside the eye in all directions in order to see all the critical parts for the operational point of view. Even though the human eye is a very fragile organ and therefore requires extreme care during the surgical procedure, there might occur some forces high enough to damage the weakest parts of the instrument structure. One of the main problems in this study was that the tool is operated directly by the surgeon's hand, and therefore, the range of operational loading was wide and hard to define.

This work is divided into six main sections. First part encloses the introduction to the topic. The second part covers the theory of building the mathematical model of the human eye. The third part reviews the actual model and its details, while the fourth part is dedicated to the experimental measurements. Results of the modelling and measurements are presented in the fifth part. In the sixth part, we discuss the results and compare them to the previously published results in related literature.

Keywords

ophthalmology, endoscopy, FEA, biomechanical engineering, optomechanics

Abstrakt

Tato magisterská diplomová práce vznikla pro České vysoké učení technické, dále ČVUT. Univerzita ČVUT patří mezi přední univerzity technického zaměření v České republice, a je situována v jejím hlavním městě, v Praze.

Účelem této diplomové práce byl výzkum napětí a deformací lidského oka a hlavice endoskopu průběhu endoskopických lékařských zákroků. Výsledky výpočtů budou dále použity při vývoji dalších lékařských nástrojů užívaných k oftalmologickým operačním zákrokům.

V průběhu vývoje nového, kompaktnějšího lékařského endoskopu, který by disponoval lepší rozlišovací schopností se vynořil problém potýkající se odolností samotného endoskopického nástroje. Mohlo by se stát, že nástroj by nemusel být dostatečně odolný k tomu, aby zvládl některé extrémní podmínky zatížení, které mohou nastat v průběhu operace vedené volnou rukou oftalmochirurga. Právě z tohoto důvodu bylo třeba provést výzkum, který by zodpověděl otázky, jaké zatížení mohou ony kritické části nástroje unést v průběhu operace tak, aby bylo možné optimalizovat jejich navržení bez toho, aniž bychom museli dělat kompromis mezi požadovanými kvalitami a pevností nástroje. V průběhu oftalmologického operačního zákroku je lidské oko penetrováno jemnou jehlou endoskopu, a to za účelem vizuálního prozkoumání vnitřních částí oční bulvy. Výkonný operátor potřebuje v tento moment pohybovat endoskopem uvnitř oka, a to všemi směry tak, aby mohl jasně vidět všechny kritické části orgánu, které z pohledu operátora potřebuje. Ačkoliv je lidské oko velice křehký orgán, a proto potřebuje výjimečně obezřetnou péči při operacích, mohou se uvnitř oční bulvy vyskytovat takové síly, které jsou dostatečně vysoké na to, aby došlo k mechanickému poškození nejjemnějších součástí struktury operačního nástroje - endoskopu. Jedním ze stěžejních problémů tohoto výzkumu byl fakt, že samotný nástroj je využíván napřímo rukou operátora, a proto byl rozsah provozního zatížení velice široký a těžko definovatelný.

Tato diplomová práce je rozdělena do šesti hlavních kapitol. V první části se nachází zevrubný a obsažný úvod do problematiky tohoto tématu. V části druhé je pokryta teorie matematického modelu lidského oka, resp. oční bulvy. Ve třetí části je shrnut konkrétní model

se všemi jeho detaily, zatímco ve čtvrté části jsou již popisovány výsledky samotného modelování. V páté části jsou popsány výsledky modelací a výsledky dosažené měření. V šesté, závěrečné části jsou srovnávány naše dosažené výsledky s dříve publikovanými výsledky v související odborné literatuře.

Klíčová slova

Oftalmologie, endoskopie, FEA, biomechanické inženýrství, optomechanika

Annotation List

Authors Name:	Jarno Mastomäki	
Name of Master's Thesis:	Numerical Simulation of the Eye Structure Under Endoscopic Treatment	
Year:	2020	
Field of study:	Instrumentation and Control Engineering	
Department:	Faculty of Mechanical Engineering	
Supervisor	doc. Ing. Jan Hošek, Ph.D.	
Bibliographical data:	Number of pages	149
	Number of figures	70
	Number of tables	32
	Number of attachments	12

Keywords: ophthalmology, endoscopy, FEA, biomechanical engineering, optomechanics

TABLE OF CONTENTS

Abstract	i
Keywords	i
Abstrakt	ii
Klíčová slova	iii
Annotation List	iv
List of figures	ix
List of tables	xii
List of symbols, units, and abbreviations	xiv
1 INTRODUCTION	18
1.1 Endoscope Prototype	19
1.2 GRIN Lens	21
1.3 Ophthalmic Surgery	22
1.4 Human Eye	23
2 MODELLING METHODS	25
2.1 The Finite Element Method	25
2.1.1 Nodes	26
2.1.2 Elements	27
2.1.3 Boundary Conditions	28
2.1.4 Assembly of the Global Systems.....	28
2.2 Mechanical Properties of the Eye	31

2.2.1	Hyperelastic Models	32
2.2.2	Mooney-Rivlin Models.....	37
2.2.3	neo-Hookean Model	42
3	MODEL	43
3.1	CAD Model	43
3.2	Element Model.....	48
3.2.1	Initial mesh quality study.....	52
3.2.2	Modelling Zinn’s membrane	56
3.3	Material Testing	59
3.3.1	Elastic properties of combined sclera tissue	59
3.3.2	Elastic properties of GRIN lens	62
3.4	Material Models.....	64
3.5	Contacts.....	67
3.5.1	Contact Algorithms.....	70
3.6	Contacts in the model.....	72
3.7	Boundary conditions	74
3.8	Solver	77
3.9	Mesh convergence study	78
4	EXPERIMENTAL MEASUREMENTS.....	80
4.1	FEA verification setup	80
4.2	Test sequence	86
4.2.1	Determination of measurement uncertainty of stress	87

4.3	3D-scanning of the specimens.....	92
4.4	Sclera thickness measurement	94
5	RESULTS	96
5.1	Dimensions of sclera and cornea.....	96
5.2	Probe curvatures	97
5.3	Port dislocation under loading.....	101
5.4	Reaction forces.....	102
5.5	Strain gauge measurement	107
6	CONCLUSIONS.....	119
7	RECOMMENDATIONS.....	124
8	References.....	127
	Appendices	134
	Appendix 1. Phynox Data Sheet 1(1).....	134
	Appendix 2. BD Microlance™ 3 hypodermic needle Technical Data Sheet 1(2).....	135
	Appendix 3. Probe curvature measurements 1(1)	137
	Appendix 4. Linear elastic material data for nH model and MR models 1(2).....	138
	Appendix 5. Test data for fitting the MR material models (uniaxial) 1(1)	140
	Appendix 6. Test data for fitting the MR material models (uniaxial) 1(1)	141
	Appendix 7. Port dislocation measurements 1(1)	142
	Appendix 8. Example calculation for measurement uncertainty. 1(1).....	143
	Appendix 9. Cantilever beam bending 1(3)	144
	Appendix 10. Port dislocation data 1(1).....	147

Appendix 11. Probe reaction forces	1(1)	148
Appendix 12. Surface flaws geometrical effect on induced stress	1(1).....	149

List of figures

Figure 1. The prototype of the endoscope (Němcová, Modified).....	19
Figure 2. USAF 1951 test of the endoscope prototype (Němcová, modified)	20
Figure 3. GRIN lens and conventional lens (Grintech GmbH, modified).....	21
Figure 4. Main parts of the human eye (Clusters, modified).....	24
Figure 5. Main domain divided into three subdomains. (Madensi et al., modified).....	26
Figure 6. Stress-strain curve of standard hyperelastic material (Ansys, Modified).....	33
Figure 7. Used material models grouped into two main categories.....	34
Figure 8. Unstable material model under horizontal loading (SimScale GmbH, modified) .	36
Figure 9. Testing scene setup, screenshot (Hošek, modified).....	43
Figure 10. Schematic 3D model of the endoscope testing situation.....	44
Figure 11. Endoscope test with characteristic dimensions.	44
Figure 12. Fixing of the eye to the holder (Hošek, modified).	45
Figure 13. Port dimensions, measured from the picture, tube outer diameter (0,728 mm)(Hošek, Modified).....	46
Figure 14. Terminal inner dimensions measurement report (Hošek, modified).....	47
Figure 15. Terminal for the probe.....	47
Figure 16. Mesh creating flow chart.....	48
Figure 17. Eye element model.	49
Figure 18. Detail from the endoscope element model.....	49
Figure 19. Vectors for defining the orthogonal quality. (Ansys, modified)	53
Figure 20. Orthogonal quality of the mesh.....	54
Figure 21. The skewness of the mesh.....	55
Figure 22. Mesh elements with low orthogonal quality (< 0.25)	56
Figure 23. Lens supporting linear spring elements.....	59

Figure 24. Force respect to displacement curve, fused quartz (Šepitka, modified).....	61
Figure 25. Data and fitting for sclera 2-term MR	66
Figure 26. Data and fitting for cornea 3-term MR.....	66
Figure 27. Different materials visualized in the geometry.	67
Figure 28. Contact characteristics (Ansys, modified).....	70
Figure 29. Frictionless contacts	72
Figure 30. Bonded contacts.....	73
Figure 31. Frictional contacts	73
Figure 32. Remote Displacement.....	75
Figure 33. Pressure load inside of the eye.	76
Figure 34. Joint constraint.....	76
Figure 35. Mesh convergence curve.	79
Figure 36. Tested scenario illustration.....	81
Figure 37. Quarter-bridge connection (All about circuits, modified).....	82
Figure 38. Test setup from up	83
Figure 39. Test setup from upright	84
Figure 40. Holder and needle used in the experiment.	84
Figure 41. Amplifier and power source used in the experiment.....	85
Figure 42. Flow chart of the measuring protocol.....	87
Figure 43. Uncertainty sources for strain measurements (Dokoupil, modified).....	88
Figure 44. Setup for 3D-scanning.....	93
Figure 45. Sliced eye model in SpaceClaim -program.	94
Figure 46. Sclera measurement setup	95
Figure 47. Three-point curve fitting in ImageJ.....	98
Figure 48. Sliced deformed models.	99

Figure 49. Probe curvature evaluation	100
Figure 50. Port dislocation measurement from still image	101
Figure 51. Probe deflection measurement.	103
Figure 52. Probe angle measurement.....	103
Figure 53. Measured strains from 14 samples	108
Figure 54. Measured stresses with measuring uncertainties.....	109
Figure 55. Approximating the position of the strain gauge $x = 0.9 \pm 0.1$ (mm).....	110
Figure 56. von-Mises stress in Phynox tube, nH (414.93 MPa).....	110
Figure 57. von-Mises stress in GRIN -lens surface, nH (128.36 MPa).....	111
Figure 58. Stress plot area on the level of the probe neutral axis. Plotting direction from 1 to 2.....	111
Figure 59. von-Mises stresses plotted along the path (317.52 MPa).....	112
Figure 60. Terminal and probe contact reaction force resultant vector.	113
Figure 61. von-Mises stress in Phynox tube, MR.c (407.21 MPa).....	114
Figure 62. von-Mises stress in GRIN -lens surface, MR.c (125.19 MPa).....	114
Figure 63. von-Mises stresses plotted along the path (308.17 MPa).....	115
Figure 64. von-Mises stress in Phynox tube, MR.f (591.83 MPa)	115
Figure 65. von-Mises stress in GRIN -lens surface, MR.f (183.71 MPa).	116
Figure 66. von-Mises stresses plotted along the path (450.64 MPa).....	117
Figure 67. Stress-strain behaviour between linear elastic model and Mooney-Rivlin solids (Wikipedia, modified).....	122
Figure 68. Collagen fibres orientation in the measured eye (Hadraba, Modified)	124
Figure 69. SEM picture of GRIN lens	125
Figure 70. Regular optical fibre in SEM.....	126

List of tables

Table 1. Characteristic dimensions of the human eye.	24
Table 2. Main element types used in FEA.	27
Table 3. Material test options to use for curve fitting.	35
Table 4. Mesh quality scales.	50
Table 5. Used element types and their quantities.	51
Table 6. Orthogonal value evaluation scale (Ansys, modified).....	53
Table 7. Skewness value evaluation scale (Ansys, modified).....	54
Table 8. Linear elastic properties of Zonular fibres.....	58
Table 9. System configuration	60
Table 10. Elastic modulus of the combined body.....	62
Table 11. GRIN lens material properties	63
Table 12. Linear elastic material models.	64
Table 13. Material parameters for the nH hyperelastic material	65
Table 14. MR material parameters.....	65
Table 15. Contact types and their characteristics.....	68
Table 16. Contact details.....	74
Table 17. Used solver settings	78
Table 18. Mesh data.....	79
Table 19. Instruments used in the FEA verification	85
Table 20. Sources of strain measurement uncertainties.....	89
Table 21. Coverage factor values and corresponding probabilities.....	92
Table 22. Instruments used in curvature measurement.....	93
Table 23. Instruments used in the thickness measurements	95

Table 24. Measured specimen curvatures.....	96
Table 25. Measured probe curvatures.....	98
Table 26. Probe deformation results.....	100
Table 27. Port dislocation, measured and FEA.....	102
Table 28. Probe angle results.....	104
Table 29. Measured deflection and length values.....	105
Table 30. Geometric and elastic values of the tested probes.....	106
Table 31. Reaction forces.....	106
Table 32. Stress results.....	118

List of symbols, units, and abbreviations

Abbreviations

CTU	Czech Technical University in Prague
FEA	Finite Element Analysis
FEM	Finite Element Method
DOF	Degrees of Freedom
GRIN	Gradient Index Lens
MR	Mooney-Rivlin material model
nH	neo-Hookean material model
CAD	Computer-Aided Design
MPC	Multipoint Contact
SEM	Scanning Electron Microscope

Symbols

E	[MPa]	Young's Modulus
ν	[1]	Poisson's ratio
V	[mm ³]	Volume
V_0	[mm ³]	Initial volume
G	[MPa]	Shear Modulus
G_0	[MPa]	Initial Shear Modulus
I_1, I_2, I_3	[1]	Strain invariants
W	[1]	Strain energy potential
ε_{eng}	[1]	Engineering strain
σ	[MPa]	Stress
B	[1]	Strain displacement
K	[MPa]	Bulk modulus
$\lambda_1, \lambda_2, \lambda_3$	[1]	Stretch ratios
λ_{lame}	[1]	Lamé 1 st parameter
μ_{lame}	[1]	Lamé 2 nd parameter
D_1	[Pa ⁻¹]	Compressibility factor
C_{10}	[Pa]	Mooney-Rivlin 1 st parameter
C_{01}	[Pa]	Mooney -Rivlin 2 nd parameter
C_{11}	[Pa]	Mooney -Rivlin 3 rd parameter

S	[1]	Slope
P	[N]	Applied force
A	[mm ²]	Contact area
h	[μm]	Probe dislocation
R_c	[μm]	Intender tip curvature radius
δ	[mm]	Deformation
S	[mm ³]	Bending section modulus
M_{max}	[Nmm]	Maximum bending moment
ρ_{min}	[mm]	Minimum bending curvature
I_z	[mm ⁴]	Second moment of area
y	[mm]	Position from the neutral axis
F	[N]	Force
k	[N/mm]	Spring constant
l	[mm]	Characteristic length
Δl	[mm]	Change in characteristic length
F_{normal}	[N]	Contact force
k_{normal}	[N/mm/mm ²]	Contact stiffness
x	[mm]	Contact penetration depth
$\lambda_{lagrange}$	[1]	Lagrange term
δ	[1]	Error

C_x	[1]	Sensitivity coefficient
u_x	[1]	Sub-uncertainty
U_x	[MPa]	Coverage corrected uncertainty
Z_{max}	[MPa]	Maximum tolerance value for material elastic properties
χ	[1]	Distribution
c	[1]	Coverage factor
D	[mm]	Outer diameter
d	[mm]	Inner diameter

1 INTRODUCTION

In this chapter, the background of endoscopes and technology related to ophthalmic operations is gone thru. Also, in the last part, a quick review is taken to the schematic model of the human eye.

Story of ophthalmic applications of endoscopy can be dated time between the great world wars. In the year 1934 procedure was first described by Dr. Harvey E. Thorpe, a native Latvian who immigrated to the U.S. in Pittsburgh in 1906. According to Pittsburgh Ophthalmology Society [1], Thorpe received his bachelor degree from electrical engineering and did his post-graduate work in ophthalmology in New York City as a truly interdisciplinary, Thorpe designed an instrument which combines Galilean telescope and an illumination source. The whole instrument shaft (6.5 mm) was inserted to eye thru 8 mm scleral incision [2].

Thorpe's design was revisited in 1978 with slight modifications by J.L Norris & G.W Cleasby. They improved [3] the original design with smaller rigid shaft (1.7 mm) At 1990 [4], V, V Volkov et al. introduced three types of flexible ophthalmic endoscopes which could be used directly to examine the interocular structures. Soon [5] after that, the laser units were implemented to the endoscopes and therefore, made possible it to proceed surgical operations with the same instrument. From that point on the prototypes had developed rapidly. All the components had been optimized, and the image resolution had improved significantly [6].

1.1 Endoscope Prototype

Schematic figure of the endoscope prototype, which mechanical endurance is studied in this work, can be seen in the (Figure 1). In the structure, there is utilized 0,5 mm gradient index lens in 23 G tube. GRIN lens is used because it reduces aberrations, and it is easier to mount in the correct place accurately. The shape of the lens helps the mounting process to be accurate in the small tube. Because of the variable refractive index on the face of the lens, it allows to keep the geometry of the lens flat.

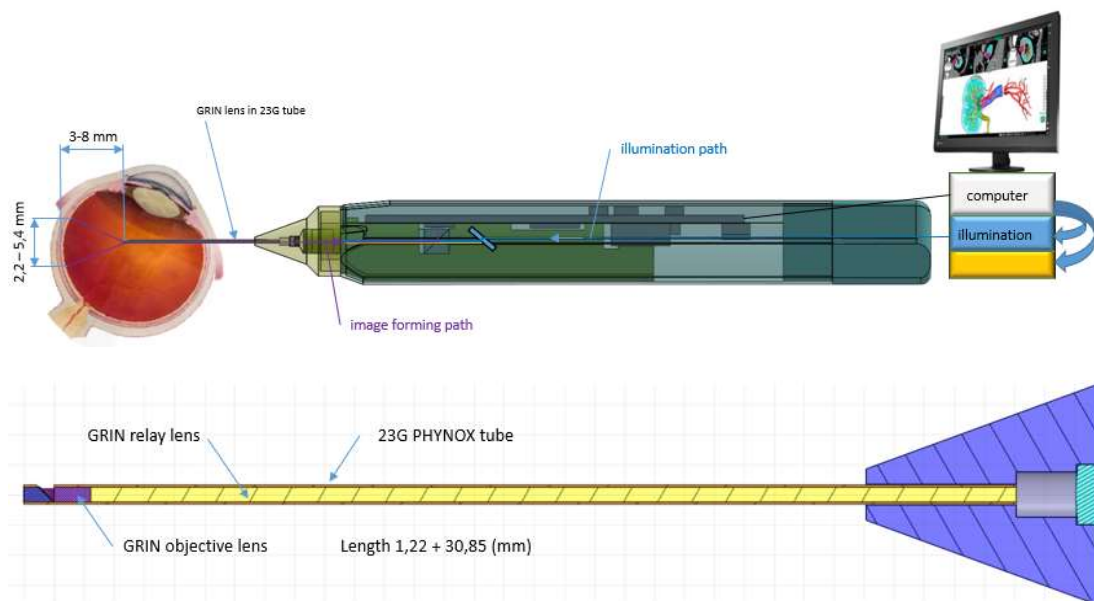


Figure 1. The prototype of the endoscope (Němcová, Modified)

The endoscope has a light source and processor for image forming. It is able to produce a high-resolution image with a measured resolution capability of (25,4) lines in a millimetre. The resolution was determined by the USAF 1951 test, as we can see from the following (Figure 2) [7].

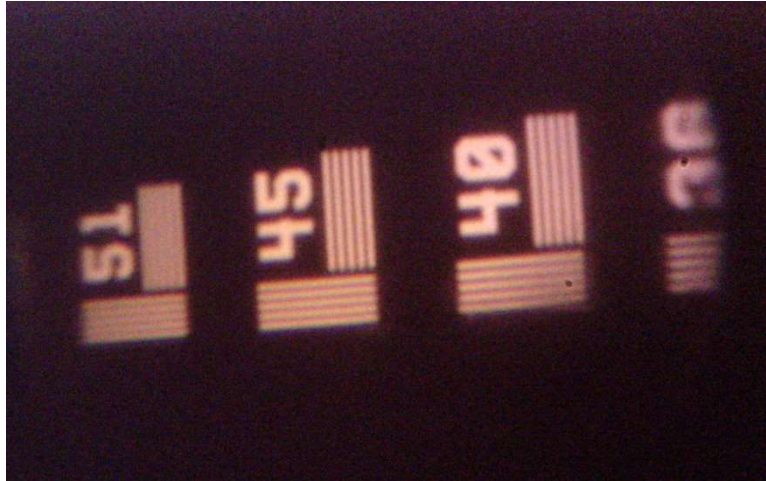


Figure 2. USAF 1951 test of the endoscope prototype (Němcová, modified)

The resolution (line frequency) can be calculated by using the following formula (1) [7],

$$\text{Line frequency (lp/mm)} = 2^{\text{group}+(\text{element}-1)/6} . \quad (1)$$

When we insert the values we get,

$$2^{4+(5-1)/6} = 25,3984 .$$

Therefore, the line frequency is,

$$\text{Line frequency} = 25,4 \text{ lp/mm} .$$

1.2 GRIN Lens

The function of the lens is to produce a radially varying delay to the optical phase of a beam, thus resulting in the wavefront to curvature. This phenomenon makes the beams to either converge or diverge after the lens. In traditional lenses, this is produced by varying the thickness of given refractive index material [8]. In GRIN (gradient index lens), the thickness is constant while the refractive index is varying in the radial direction. A typical application for this type of lens is fused with optical fibre where it collimates the light [9]. A schematic figure of the differences between a GRIN lens and a conventional lens can be seen in figure (3) [8].

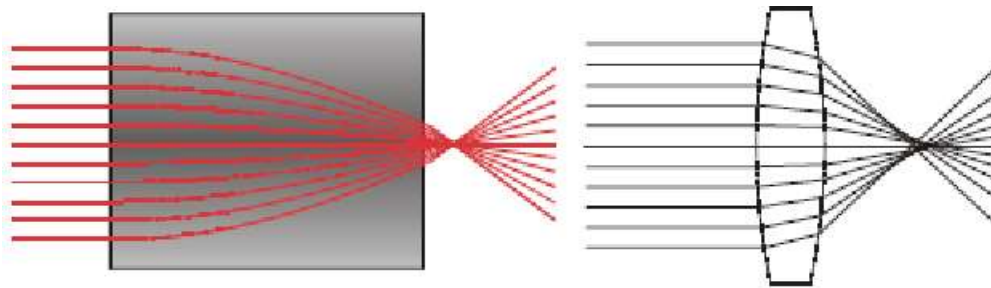


Figure 3. GRIN lens and conventional lens (Grintech GmbH, modified)

The lens used in this application is produced by silver ion exchange on the face of the glass rod [10]. In this technique, the glass is immersed in a liquid with silver ions. Because of the diffusion, the sodium ions in the glass are partially exchanged with the silver ones. The ion charge is more significant in the edges than in the middle. Thus, the base material obtains a gradient material structure and therefore, the corresponding gradient of the refractive index [11].

1.3 Ophthalmic Surgery

One of the main problems in this study was that the operated instrument (endoscope) is controlled directly by the surgeon's hand, and therefore the range of operational loading is extensive and hard to define. During the ophthalmic operation, the surgeon needs to move the endoscope inside the eye in all directions. Even though the human eye is a very fragile organ and therefore requires extreme care during the surgical procedure, there might occur some forces high enough to damage the weakest parts of the instrument structure.

Although the ophthalmic endoscopes have been around for 1934, according to Marra, K et al., the popularization of ophthalmic endoscopy has been promoted by recent technological advancements that increased the number of indications for endoscopy [6]. Dr. Martina Nemčoková, who is a doctor of Ophthalmology from Charles University, said that according to their experience, the endoscopic examinations are mainly done for infants. Because of natural reasons, every move is made with high care [12]. Even though that the endoscopic view provides two fundamental advantages, it is a relatively rarely used tool in ophthalmological operations. These advantages are; firstly, it reaches areas that usually are not so easy to examine because it passes anterior segment and secondly, it eases the visualization of anterior structures like ciliary bodies and sub-iris space. Together these two advantages provide a steady base for surgery.

1.4 Human Eye

The schematics of a human eye have been researched over 400 years. In the early 17th century Christoph Scheiner, a Jesuit priest, and physicist introduced a semantic model of the human eye by using his knowledge from studying the eyes of animals [13]. Since that, many scientists have researched the characteristics of an eye. Gullstrand received his Nobel from his work "Einführung in die Methoden d. Dioptrik d. Auges d. Menschen" in 1911. Even today, the Gullstrand's model exists, and it is still used, sometimes with slight modifications.

In this thesis, the focus is on the schematic eye model instead of the more realistic human eye models. This means that we were paying interest for the curvatures, thicknesses and spacings between each physical component of the eye. For this purpose, the Gullstrand's eye model came handy. Because the interest was not particularly on the eye in the optical point of view, it made the simplification of the model relatively easy. In the model, it was assumed that the shapes are spherical instead of prolate and oblate. The characteristic dimensions were based on the Gullstrand's eye model, and the modifications were presented by Atchison D A & Smith G [14] and Vurgese S et al. [15].

From the following table (1), we can see the initial characteristic dimensions of the eye modelled for the thesis. The annotations follow the ones seen in figure (4) [16].

Table 1. Characteristic dimensions of the human eye.

Annotation	Dimension	Unit	Source
1.	24	mm	[14]
2.	16	mm	[14]
3.	3,5	mm	[14]
4.	3,3	mm	[14]
5.	0,5	mm	[14]
6.	7,7	mm	[14]
7.	6,8	mm	[14]
8.	6	mm	[14]
9.	11	mm	[14]
10.	0,94	mm	[15]

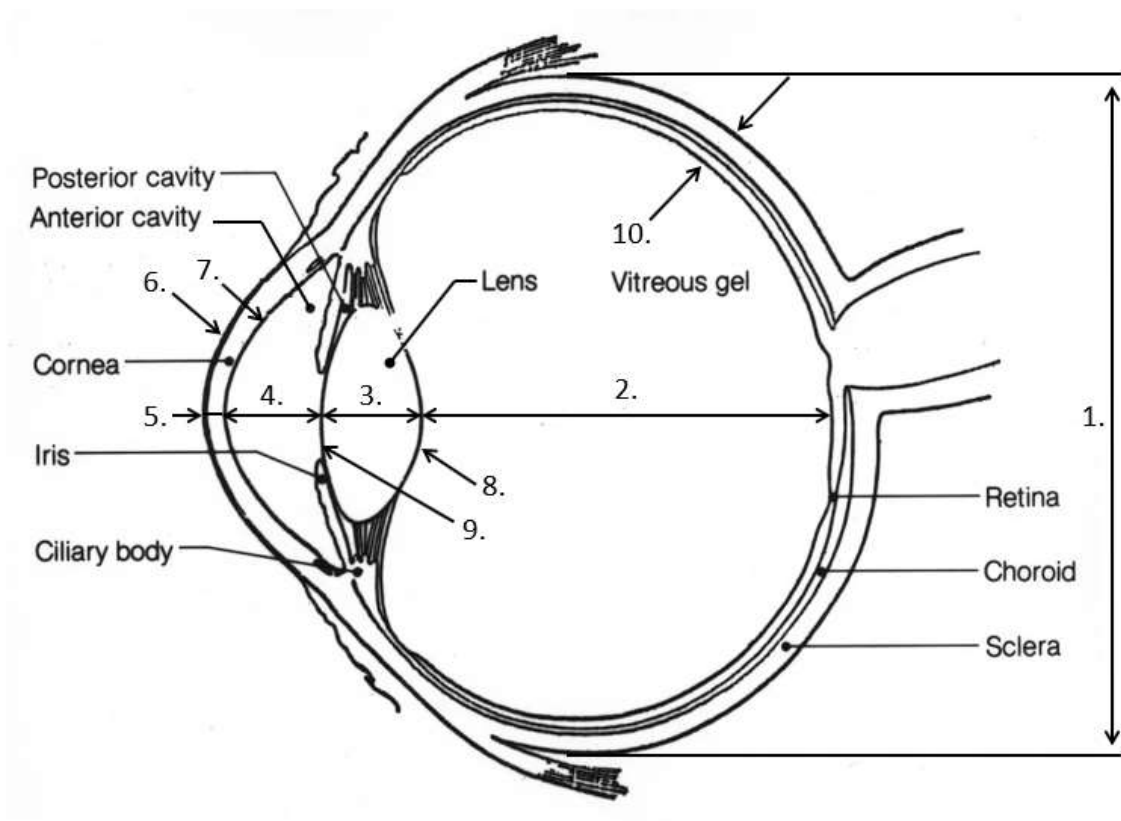


Figure 4. Main parts of the human eye (Clusters, modified)

2 MODELLING METHODS

In this chapter, the theoretical side of the modelling methods, used in this thesis, is reviewed. The first part describes the finite element method in general; the second one explains the theory of nodes, the third one defines the concept of elements, the fourth one interprets the meaning of boundary conditions briefly, and in the last part the assembly of a global system model is derived.

2.1 The Finite Element Method

The Finite Element Analysis, further FEA, was introduced in 1956 by Turner et al. [17]. This powerful computational method was developed to approximate the results in real-life engineering problems. The article was first published in the Journal of Aeronautical Sciences, and the technique was, therefore, specially developed for complicated stiffness and deflection analysis in Aerospace engineering. The present of high-speed aircrafts was creating numerous problems in the field of design of the aircraft structures. The issue, which raised above all was the prediction of the behaviour of the elastic structure under dynamic loading. The difficulties led to the non-stable dynamic behaviour of the plane, which was caused by unpredicted vibrations and flutter [18].

When the composite materials started to rule in the aerospace industry, the problems begun to be even more complicated than what the engineers had used to handle. The elementary theories of flexure and torsion could not be analysed anymore by using analytical methods. Even though the structures could be still tested physically in the world of growing demand, time and money were limited. By using the FEA, the engineers were able to predict complex structural phenomena, and therefore, the timeline from the prototype building and product development to actual production were shortened up significantly. In the problems where FEA has applied, a continuum of the matter usually occurs. This means liquid, gas or solid continuum mechanics. In FEA the problem is divided into the finite number of small subdomains which are called elements. The systematic solution is constructed by applying analytical means to each element separately. This weighted residual method is interpolating

the functions over every element and plotting the results in the nodes, which are located in the corners of the elements. The boundary conditions are given to those nodes by their connection to other nodes or according to the interaction functions between the different main domains (bodies).

The ability to discretize the irregular domains with finite elements makes the method extremely usable to engineering problems. From figure (5) [18], one can see the basic principle of division of a domain into three subdomains (elements).

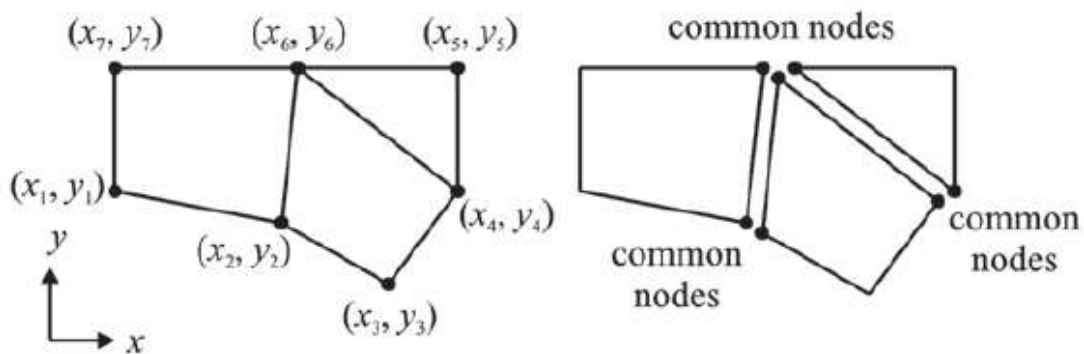


Figure 5. Main domain divided into three subdomains. (Madensi et al., modified)

2.1.1 Nodes

A node is a coordinate location in space (2D or 3D) where the degrees of freedom, further DOF, is defined. These defined DOFs represents the possible movement of this point due to the applied loading. They also represent the forces and moments which are transferred from point to another. The results of FEA is plotted in the element nodes.

In the body of the real application, without any boundaries, can move in six different directions; thus, it has six DOFs. These are translational and rotational directions. The translational movement happens along the X, Y and Z axis, whereas rotational movements are round those same axes. In FEA, the node movements can be limited for a variety of reasons.

One of these is to prevent the rigid body motion during the analysis. This is also related to the types of forces and restrains the node can transmit forward.

An axial or shear force is equivalent to a translational movement while the moment is equivalent to a rotational movement. Therefore, in order to transfer the moment through particular axis, the node must have rotational DOF about the axis.

2.1.2 Elements

An element is the basic building block of FEA. There are several basic types of elements used in FEM. In the following table (2) we have listed six of them [19].

Table 2. Main element types used in FEA.

Element types	Translational			Rotational		
	X	Y	Z	X	Y	Z
Truss, Spring	YES	YES	YES	-	-	-
Beam	YES	YES	YES	YES	YES	YES
2-D	-	YES	YES	-	-	-
Membrane	YES	YES	YES	-	-	-
Shell	YES	YES	YES	YES*	YES*	-
Solids	YES	YES	YES	-	-	-

*Rotational DOFs are defined by local coordinates instead of global ones.

From here, one can see that the element is, de facto, the mathematical definition of how the DOF of a node is related to the next node. It also relates how deflection creates stress.

2.1.3 Boundary Conditions

The boundary condition is basically a set of known value for displacement or applied force. Boundary conditions are necessary for the solution of a boundary value problem. It is a set of differential equations to be solved when the conditions are known. This shall not be confused with the initial value problem where only the conditions of one extreme are known.

2.1.4 Assembly of the Global Systems

When modelling an engineering problem with a finite element method, we need to define the element characteristics. The characteristics are described by stiffness matrices. These matrices are multiplied by nodal unknowns in a vector form while the right-hand side of the equation is the applied force matrix. We can derive the stiffness matrix by using the stress-strain relation. For this, one needs to have the elastic properties of the materials in the analysis. Therefore, Hooke's law can be written in matrix form as following (2) [20]

$$\{\sigma\} = [E] \times \{\varepsilon\}, \quad (2)$$

from the Hooke's law can be seen that the stress (σ) is directly proportional to the strain (ε) while E is Young's Modulus and therefore remains constant when the temperature is assumed to be constant. The strain vector can be written as following (3) [21]

$$\{\varepsilon\} = [B] \times \{\delta\}, \quad (3)$$

where B is the strain displacement matrix $[B] = \partial[N]$. If the Hooke's law is re-written with the help of the definition of the strain, we obtain (4),

$$\Rightarrow \{\sigma\} = [E] \times [B] \times \{\delta\}. \quad (4)$$

Potential energy is integrated over the volume of the elements (5) [21],

$$\Pi = \int \{\varepsilon\}^T \times \{\sigma\} dV - \{\delta\}^T \times \{F\}. \quad (5)$$

The nodal displacements are taken out of the integration and in order to find the minimal potential energy one need to set the partial derivatives to zero as following (6) [21],

$$\frac{d\Pi}{dt} \times \{\delta\} = \int [B]^T \times [E] \times [B] dV \times \{\delta\} - \{F\} = \{0\}. \quad (6)$$

This comes down to the well-known spring equation, where the spring constant is a local element stiffness matrix (7) [21].

$$[k] = \int [B]^T \times [E] \times [B] dV. \quad (7)$$

The above equation (7) is used to find the local element stiffness matrix when the elastic properties and nodal locations are given. Then the local matrices are assembled as a global system. This can be seen from the following formula (8) [18] from where one can see the spring analogy,

$$[K] \times \{\delta\} = \{F\}, \quad (8)$$

where $[K]$ is the assembly of stiffness matrices and $\{F\}$ represents the global force vector. In the previous formula $\{\delta\}$ is the unknowns, i.e. displacement vector. The global $[K]$ is assembled from local (elemental) stiffness matrices as following (9) [18],

$$[K] = \sum_{e=1}^n [k]^{(e)} = [k]^{(1)} + [k]^{(2)} + \dots + [k]^{(n)}, \quad (9)$$

where $[k]^{(e)}$ is the local stiffness matrix. Similarly, performed the assembly of the global force vector. This can be seen from the following formula (10) [18],

$$\{F\} = \sum_{e=1}^n \{f\}^{(e)} = \{f\}^{(1)} + \{f\}^{(2)} + \dots + \{f\}^{(n)}. \quad (10)$$

In order to have a unique solution for the system of differential equations, each determinant of the global stiffness matrix $[K]$ must be nonzero. If any of the eigenvalues appear to be zero, it means that the result is not possible, i.e. the matrix is singular. The global system matrix is modified in order to eliminate the zero eigenvalues by applying the boundary conditions. These boundary values are introduced to suppress the DOFs of the corresponding zero

eigenvalues. From the eigenvalues, we get the corresponding eigenvectors (δ) which each of them is representing a possible solution.

2.2 Mechanical Properties of the Eye

The mechanical properties of the human eye are relatively hard to define unequivocally. This is because the tissues are heterogeneous and porous. There is a wide range of different approaches on how to model human eye materials in the literature. The most significant problem of those models is that not many of them have been used in the verified simulation experiments. Thus, we cannot know how nicely those material models are performing under complicated loads. Therefore, one of the main tasks was to find the simplest possible material model which would describe the material behaviour best under the applied load. Because the real-life tissues have highly non-linear behaviour, we cannot expect them to be characterised by any linearized models. The only possibility, in linearized materials, would be some sort of multilinear material model which has multiple different linear regions. This type of model described on the previous sentence would require multiple linearization's, and thus the final accuracy would suffer much. Hence, it is not merely worth seeing much of unnecessary work for unreliable results.

2.2.1 Hyperelastic Models

Instead of linear elastic models, many previous researchers have applied various types of hyper-elastic material models when trying to describe the behaviour of human tissues [22] [23]. The hyperelastic models are highly non-linear, and they were developed on the base of elastomers. Elastomers are a top category for natural and synthetic rubbers, which are amorphous and comprised of long molecular chains. Because of the nature of those molecular chains, they usually occur twisted and randomly oriented. When a tensile load is applied, those chains tend to partially straighten, but when the load is removed, the chains revert back to their original form. The material strengthens when the deformation is high enough to create crosslinking of the molecular chains, and therefore their resistivity due to the dislocations are increased [24]. In generally the hyperelastic materials can undergo huge elastic deformations. The scale is in order of 100 to 700 (%). Because there is just a little volume change under the applied load, the elastomers are considered as an incompressible material. One significant feature of the hyperelastic materials is that they can have multiple hardening regions in the stress-strain curve. From figure (6) [24], we can see an example of the measured stress-strain curve for a hyperelastic material (rubber). In the curve, we can see the presence of hysteresis and stress softening. In this work, it was assumed that the materials are homogenous, isotropic and hyperelastic.

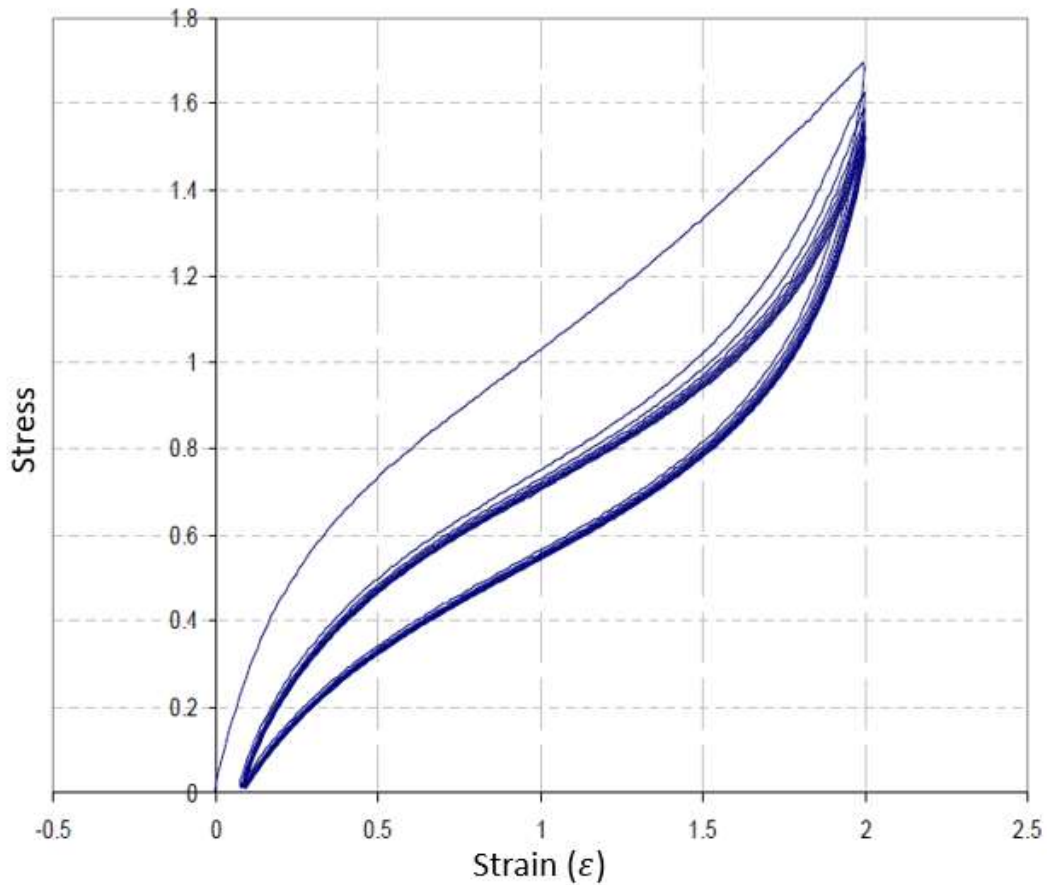


Figure 6. Stress-strain curve of standard hyperelastic material (Ansys, Modified).

In the theory of hyperelasticity, the constitutive material model is described through a strain energy potential function. Unlike linear plastic-elastic models, the stresses and strains are not described through elastic modulus and Poisson's ratio but instead with strain energy potential. Hyperelastic models, used in this study, can be roughly grouped in two main categories. Those categories can be seen from the following figure (7).

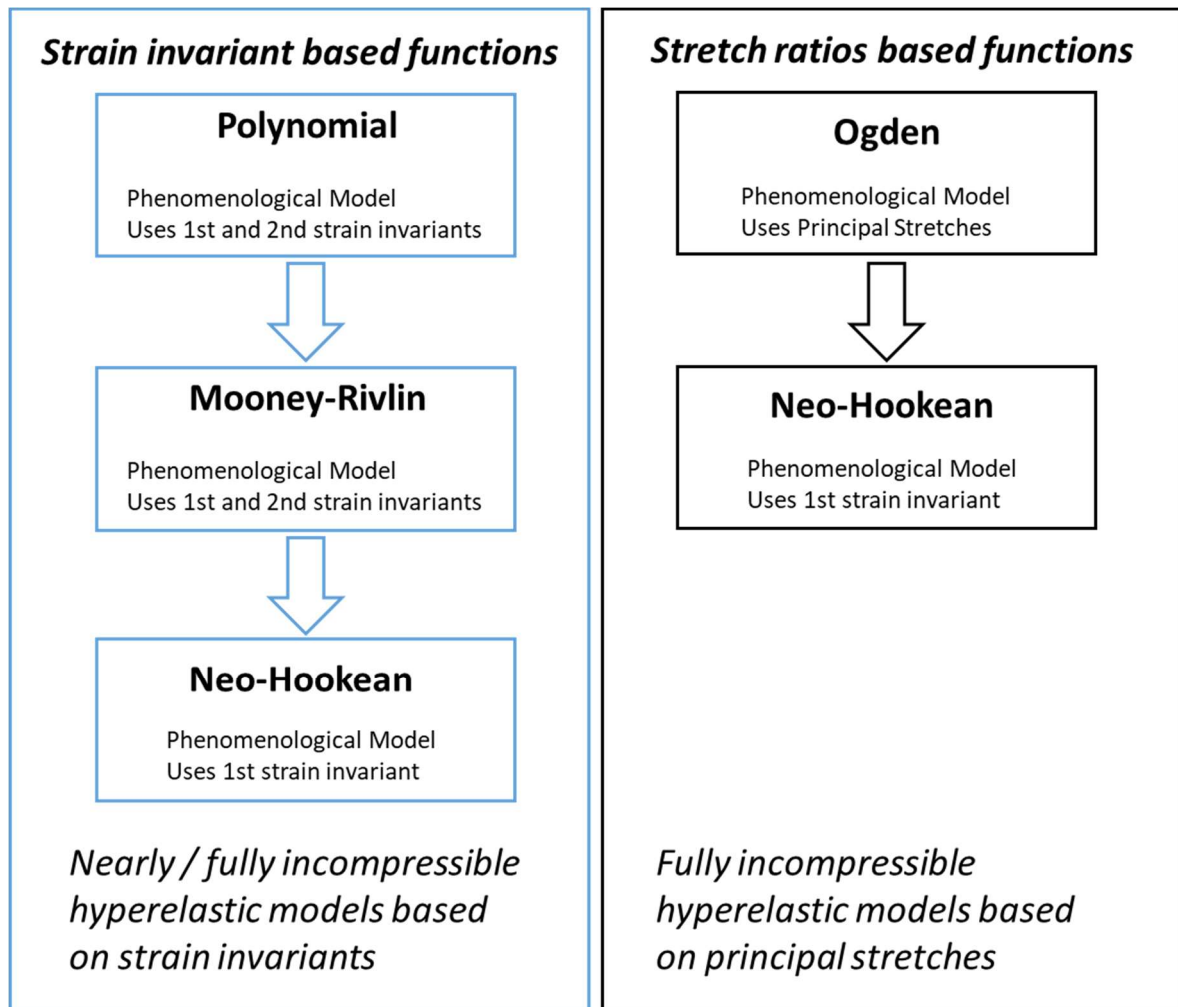

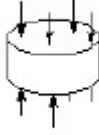
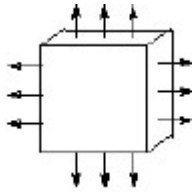
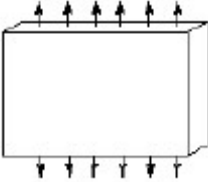



Figure 7. Used material models grouped into two main categories.

While there is plenty of pre-defined material models to choose, mostly the rough decision is made by using the following categorizations. Firstly, the type of material needs to be considered, secondly the loading conditions, i.e. what is the expected total strain under loading and lastly the available material test data. We can say that in general, the best strain energy function is the one which produces the closest curve fit to test data. The test data comes typically from one or more of the tests we can see from the following table (3) [25].

Table 3. Material test options to use for curve fitting.

Test type	Description	Schematic
Uniaxial Tension	Simple tension in one axis	
Uniaxial Compression	Simple compression in one axis	
Biaxial Tension	Tension in two axes simultaneously	
Planar Shear	Pure shear specimen dimension (10:1)	
Volumetric Test	Cylindrical specimen under compression	

Often two or more models produce similar results in the analysis, but in some applications, there might be only one function that is appropriate to describe the material behaviour. The general rule is that data from one material test is enough to create a valid nH material model; two is needed for MR and three for full Ogden model [26]. When making exceptions from this, previously mentioned rule of thumb, one can obtain non-stable model behaviour. This is highly depending on the chosen material parameters, but model can be either always-,

conditionally stable or unstable. This is related to the loading and the caused relative displacement magnitude. An unstable model might cause an unphysical response of the model and therefore corrupts the results. An example of this behaviour can be seen in the following figure (8) [26].

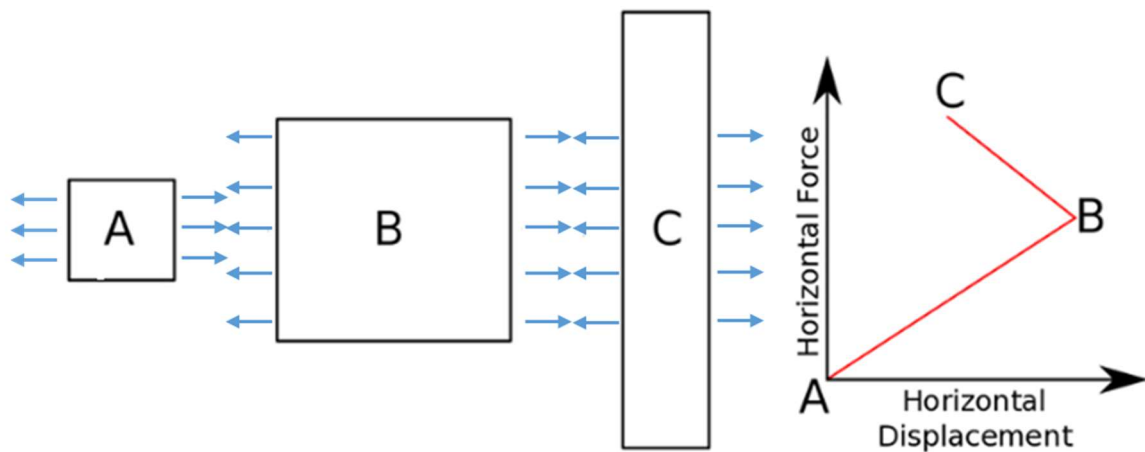


Figure 8. Unstable material model under horizontal loading (SimScale GmbH, modified)

According to SimScale general guideline for choosing a material, a model is that neo-Hookean is always stable, but it has some limitations on describing large relative strains whereas full Ogden model stability depends on parameters but in contrary it is fully capable of covering strains from zero to failure [26].

2.2.2 Mooney-Rivlin Models

Mooney-Rivlin models, MR in future, were introduced by Melvin Mooney in 1940 whom theorem was expressed in terms of invariants by Ronald Rivlin in 1948 [27] [28]. It is essential to realize that the MR model does not give any specific insight into the material behaviour. Mooney-Rivlin is a curve fits of a polynomial to test data. The numerical values of coefficients are results from the curve-fits. These coefficients are given to the FE analysis, and they define how stiff the material is under the applied load. The two-term MR model is equivalent to the polynomial form when the order of the polynomial fitting is first.

The two-term M.R. model is most commonly used. The model describes the behaviour of the material when the following conditions are filled [29] [26].

- Valid up to 90-200 (%) relative tensile strains.
- Will not account strain stiffening behaviour.
- Pure shear behaviour may be characterized up to 80 (%)
- Compression behaviour can be characterized to 30 (%)

Hyperelasticity of the material models is defined with a strain energy potential. Sometimes term strain energy function is used. Strain energy potential is commonly denoted as (W), and it can be expressed as a function of the principal strain invariants as following (11) [24],

$$W = W(I_1, I_2, I_3). \quad (11)$$

If we assume that the material is isotropic then the I_3 term always equals 1. This is because when the $\varepsilon = 0$ and stretch ratio $\lambda = 1$. This is caused by the initial assumption of isotropic material. From the following equation (12) [30], one can see why the third invariant is one,

$$I_3 = \lambda_1^2 \cdot \lambda_2^2 \cdot \lambda_3^2 = \left(\frac{V}{V_0}\right)^2. \quad (12)$$

In equation (12) the $\frac{V}{V_0}$ represents the volume ratio. The rest of the invariants are expressed as following (13 & 14) [30],

$$I_1 = \lambda_1^2 + \lambda_2^2 + \lambda_3^2, \quad (13)$$

$$I_2 = \frac{1}{\lambda_1^2} \cdot \frac{1}{\lambda_2^2} \cdot \frac{1}{\lambda_3^2}. \quad (14)$$

As we can see from the previous equations (3,4 & 5) the main invariants are defined by stretch ratios (λ) which are the ratios of initial lengths in the principal local directions (1, 2, 3). The stretch ratio can be expressed thru the relative strain, commonly known as an engineering strain (15) [30].

$$\lambda = 1 + \varepsilon_{eng} \quad (15)$$

In the previous equation (15) the sub-note (*eng*) indicates the engineering, i.e. relative strain. The polynomial form, sometimes called as a generalized M.R. model, is based on the first and second invariants and its general form can be seen in following (16) [24],

$$W = \sum_{i+j}^N C_{ij} \cdot (I_1 - 3)^i \cdot (I_2 - 3)^j + \sum_{k=1}^N \frac{1}{D_1} \cdot \left(\frac{V}{V_0} - 1\right)^{2k}. \quad (16)$$

The two-term MR is equivalent to the general polynomial form when we substitute the constants as following (17) [24],

$$W = C_{10} \cdot (I_1 - 3) \cdot C_{01} \cdot (I_2 - 3) + \frac{1}{D_1} \cdot \left(\frac{V}{V_0} - 1 \right)^2 \quad (17)$$

The constant C and be expressed with the help of Lamé 2nd coefficient μ_{lame} as following (18) [31],

$$C_{10} = \frac{\mu_{lame}}{2}, \quad (18)$$

where the C_{10} is considered as the first MR term. The second MR term can be expressed with the help of the initial shear modulus (G_0) as following (19) [32],

$$G_0 = 2 \cdot (C_{01} + C_{10}) \quad (19)$$

Because this work is dealing with isotropic material, the shear modulus can be calculated from the other elastic properties of the material as following (20) [32],

$$G = \frac{E}{2 \cdot (1 + \nu)} \quad (20)$$

Therefore, the second MR parameter (C_{01}) can be calculated as following (21),

$$\Rightarrow C_{01} = \frac{E}{4 \cdot \nu + 4} - C_{10}. \quad (21)$$

The compressibility term (D_1) can be described with the help of Lamé 1st coefficient (λ_{lame}) as following (22) [31],

$$D_1 = \frac{\lambda_{lame}}{2}. \quad (22)$$

The compressibility term can be defined by specifying nonzero values for D_i by setting the Poisson's ratio less than (0.5). Then we can use the following relation (23) [31],

$$D_1 = \frac{2}{K_0} = \frac{3 \cdot (1 - 2 \cdot \nu)}{G_0 \cdot (1 + \nu)} \quad (23)$$

Bulk modulus can be explained by the help of the Lamé coefficients. Bulk modulus describes how resistant the material is for compression (24) [32],

$$K = \lambda_{lame} + \frac{2}{3} \cdot \mu_{lame}. \quad (24)$$

The Bulk Modulus can be written with the help of Young's Modulus and Poisson's as one can see from the next equation (25) [32],

$$K = \frac{E}{3(1 - 2 \cdot \nu)}. \quad (25)$$

Also, Lamé's first parameter (sometimes called as Lamé modulus) can be re-written by Young's modulus and Poisson's ratio as following (26) [32],

$$\lambda_{lame} = \frac{E \cdot \nu}{(1 + \nu) \cdot (1 - 2 \cdot \nu)}. \quad (26)$$

By using these previous formulas (25 & 26), we can derive the Lamé's second parameter (μ) as following (27),

$$\Rightarrow \mu_{lame} = \frac{3 \cdot (K - \lambda_{lame})}{2}. \quad (27)$$

2.2.3 neo-Hookean Model

While MR with two terms is valid up to 90-100 (%) relative tensile strains, the neo-Hookean (further nH) model is capable of capturing only 30-40 (%) of the relative tensile strains in uniaxial tension [24]. nH model is considered the simplest hyperelastic material model. nH model can be thought as a subset of the first polynomial form, where the constants $C_{01} = 0$ and $C_{10} = \frac{\mu}{2}$.

The two-term MR model is most commonly used. The model describes the behaviour of the material when the following conditions are filled [29] [26].

- Valid up to 100 (%) relative tensile strains.
- Will not account strain stiffening behaviour.
- Pure shear behaviour may be characterized up to 80 (%)
- Compression behaviour can be characterized to 30 (%)

nH model requires an initial shear modulus (G_0) which is defined as following (28) [24],

$$G_0 = 2 \cdot C_{10} . \quad (28)$$

Strain energy potential for nH model is defined in the following way (29) [24],

$$W = \frac{\mu_{lame}}{2} \cdot (I_1 - 3) + \frac{1}{D_1} \cdot \left(\frac{V}{V_0} - 1 \right)^2 \quad (29)$$

3 MODEL

In this chapter, the steps of building a finite element model are gone through. The first part conceals the CAD-model, the second one describes the building of the element model, in the third part, there is defined the materials for the elements and in the fourth part, describes the contacts between the bodies.

3.1 CAD Model

Like it was earlier mentioned in the chapter (1.4) the eye model in this thesis is based on the Gullstrand's schematic eye model. All the dimensions can be found from the table (1). The model assembly imitates the testing scene setup, which can be seen from the figures (9) [33] and (10). All the modelling was done by a program called SpaceClaim. From figure (11), one can see the cross-section of the final model with the endoscope probe with the characteristic dimensions of the setup.

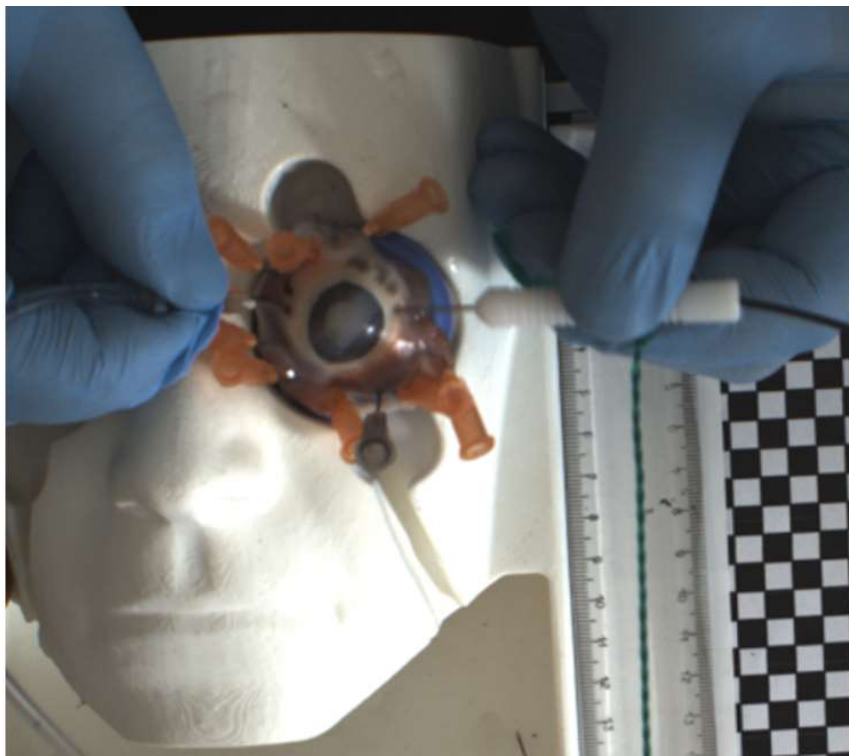


Figure 9. Testing scene setup, screenshot (Hošek, modified)

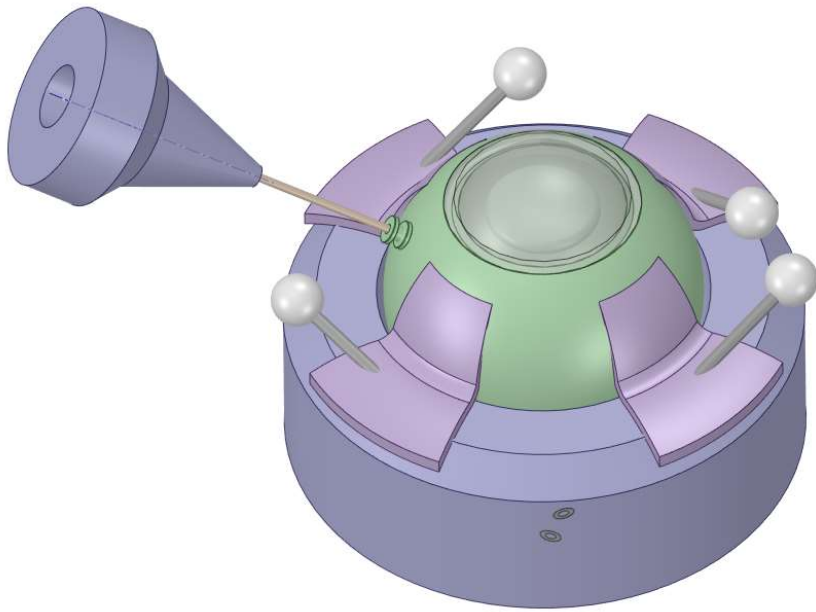


Figure 10. Schematic 3D model of the endoscope testing situation.

From the following figure (11), we can see the characteristic dimensions of the initial setup of the testing situation.

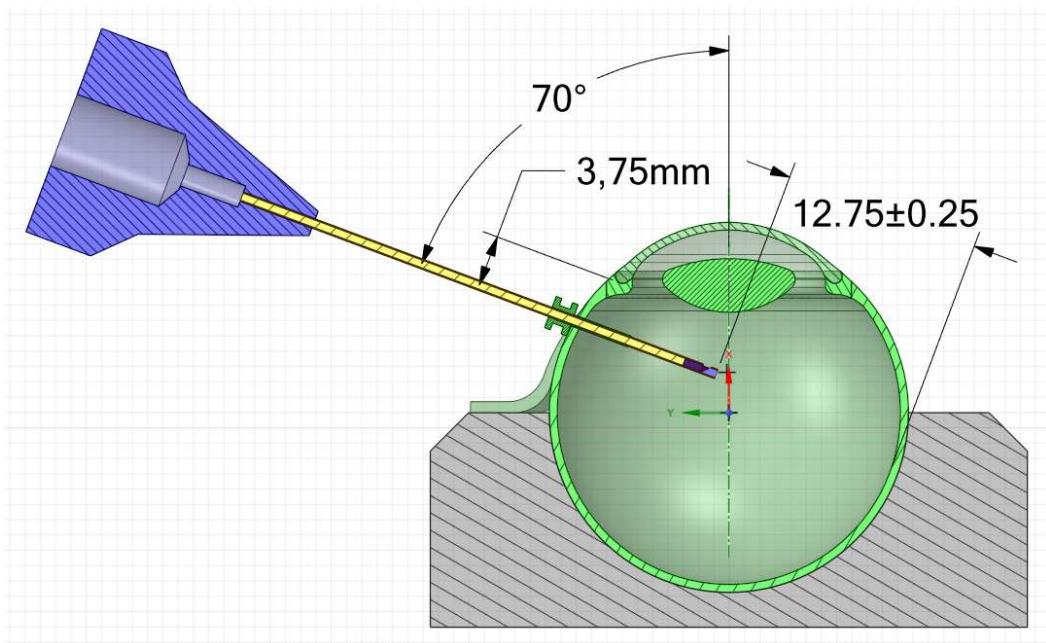


Figure 11. Endoscope test with characteristic dimensions.

The distance between the end of the endoscope and retina comes from the worst-case scenario because we wanted to have the biggest possible moment reaction to the probe during normal surgical use. In all other cases, the dimensions are evaluated by operational surgeon said MD Martin Penčák from the University Hospital Kralovske Vinohrady [34]. According to him, the penetrating point is usually located 3.75 ± 0.25 mm from the limbus (the part where the cornea changes into sclera) for pseudophakic eye and 4 mm for the phakic eye [34]. The angle is usually between 10° to 90° . In this case, the initial angle was ruled by coincidence plane of the external insertion and the eye curvature.

The fixing of the eye can be seen from the following figure (12) [33]. The needles are penetrating the eye and the silicon holder in the 3D- printed dummy face. This setup simulated the situation where the surgeon is holding the eye still while committing the operation. In the front of the eye, a port for the endoscope can be seen. Right opposite the endoscope terminal at the other side of the eye is located a tube which is used for pressurizing the eye during the operation. Ophthalmologists are using pressurizing to remain constant pressure in the eye, which corresponds to the level of the healthy eye (15 mmHg) [34].

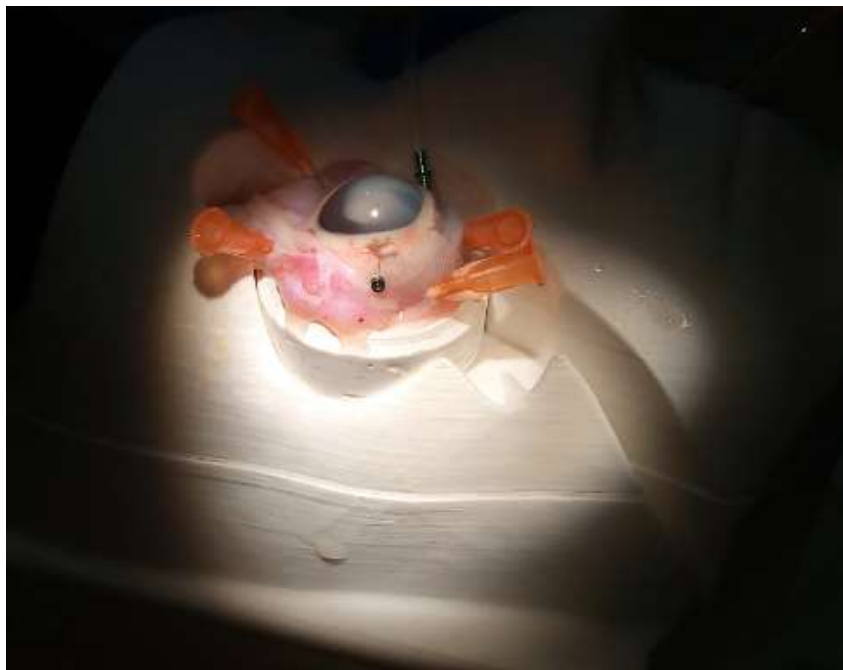


Figure 12. Fixing of the eye to the holder (Hošek, modified).

When the eye is penetrated, the surgeons are using a special terminal, so the moving of the endoscope does not harm the eye tissue around the penetration point. The terminal insertion also ensures the proper closing of the surgical wound in the eye. From the following figure (13) [33] we can see the outer dimensions of the surgical terminal, which is inserted to the eye.

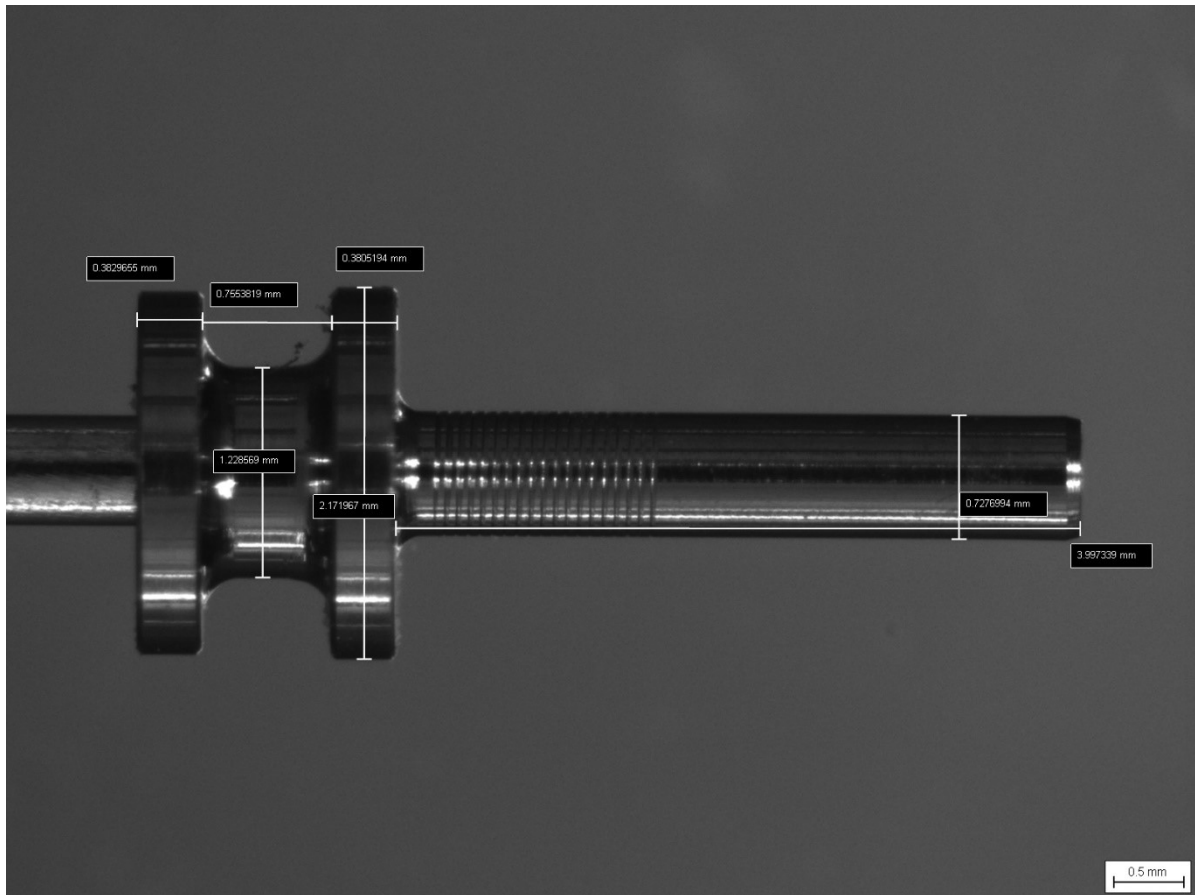


Figure 13. Port dimensions, measured from the picture, tube outer diameter (0,728 mm)(Hošek, Modified)

Like in every moving machine element, there is some endplay between the probe and the terminal. The terminal roundness and inner diameter can be seen in the following figure (14) [33]. Measurements proceeded in the CTU (13th of March 2019).

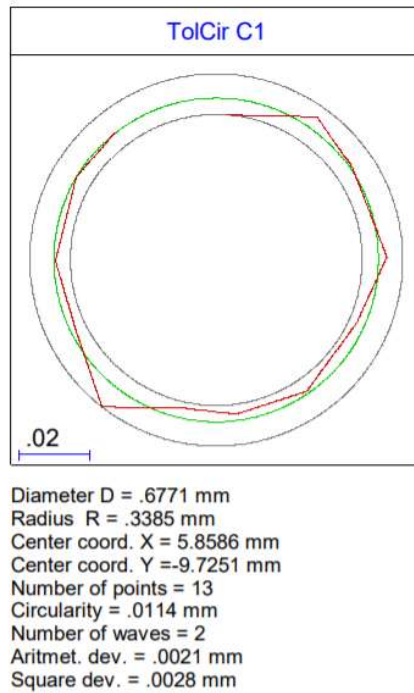


Figure 14. Terminal inner dimensions measurement report (Hošek, modified)

The terminal insertion in the CAD model can be seen from the following figure (15).

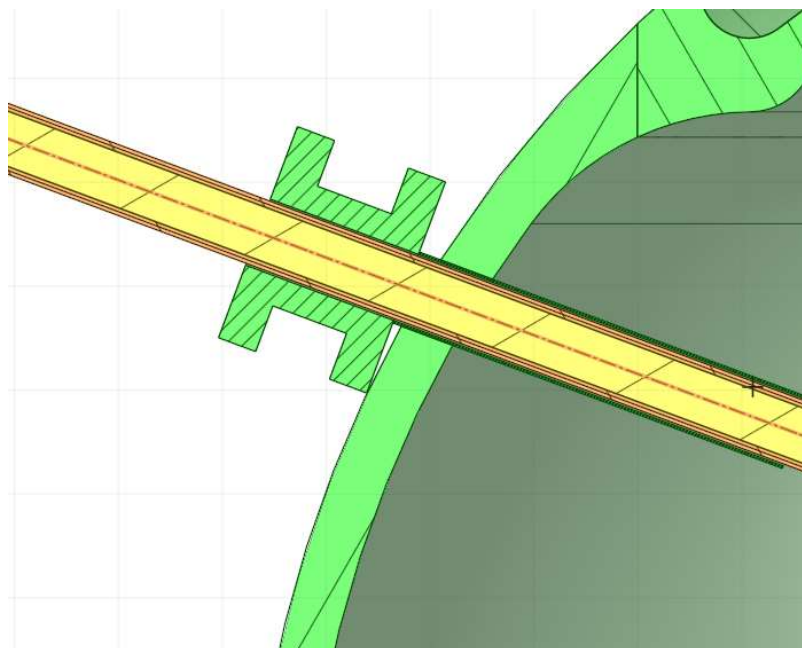


Figure 15. Terminal for the probe

Since the port is inserted in the eye through a cutting wound which is zigzag-shaped, it helps to create pressure in the interface between the port and the sclera tissue. After the port is removed, the cutting wound closes itself, and therefore the healing process is faster than with straight cut wound.

3.2 Element Model

When creating an element model from an object in analysis, the shapes and thicknesses need to be concerned carefully. The mesh needs to represent geometry as good as possible. Most of the time, the mesh controls are ruled by calculation time, area of interest, the topology of the geometry and thickness of the solids. Creating an optimal element model is an iterative process which follows the flow chart presented in figure (16).

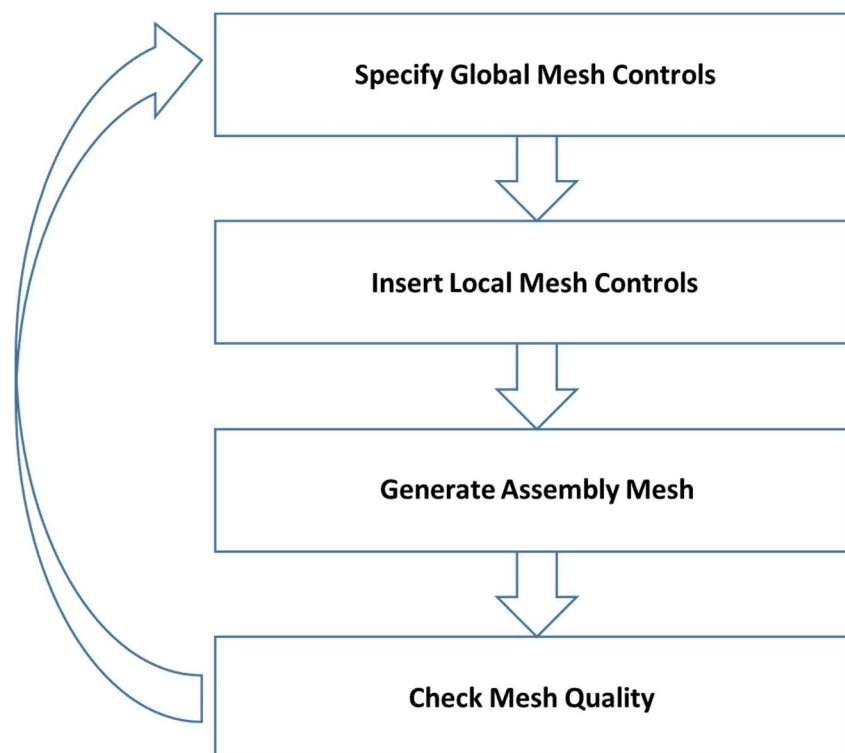


Figure 16. Mesh creating flow chart

From the following figure (17), we can see the element model of the eye experiment. From the figure (18), we can see a detail of the endoscope probe mesh encircled with red on the figure (17).

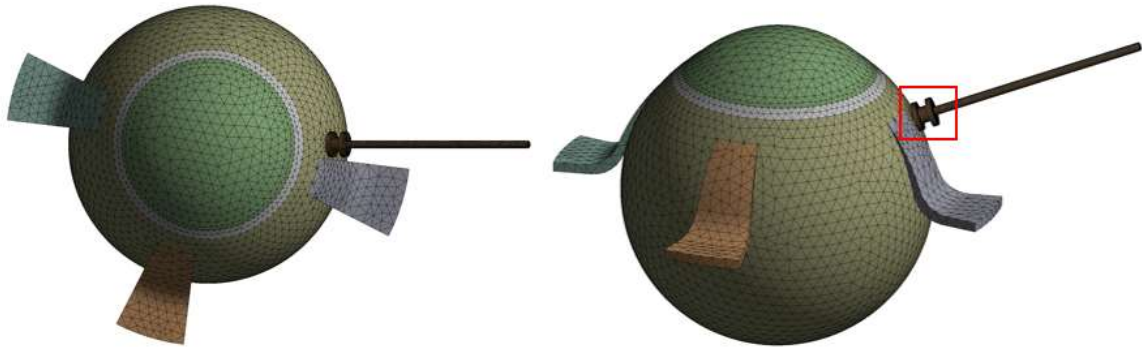


Figure 17. Eye element model.

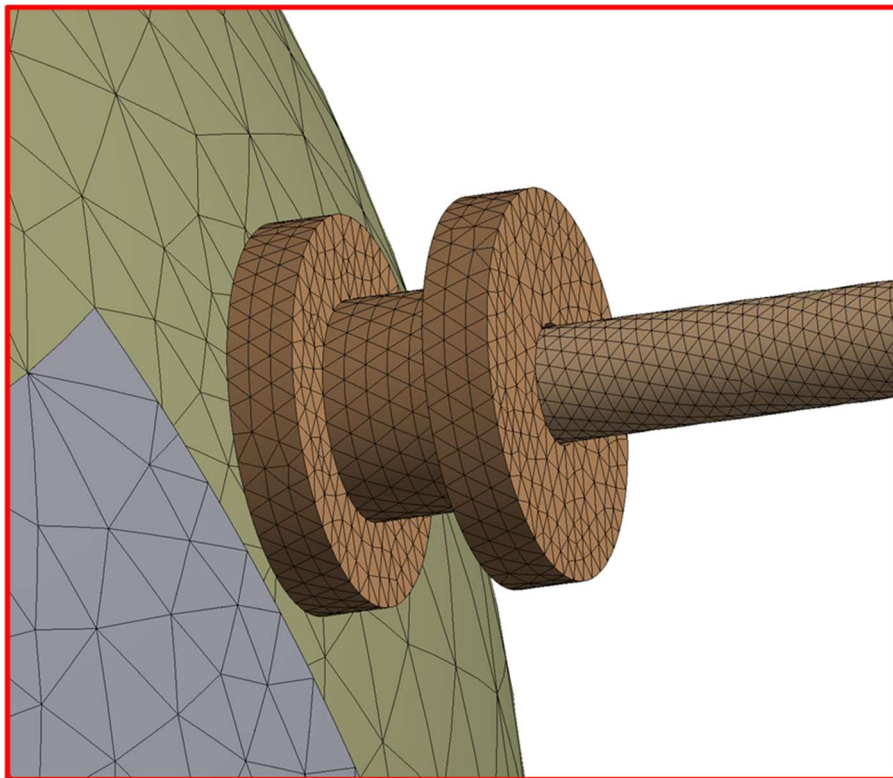


Figure 18. Detail from the endoscope element model.

The mesh can be evaluated by numerous criteria. All the criteria can be seen from the following table (4) [35].

Table 4. Mesh quality scales

Criteria		Optimal value	Bad value
Element quality		1	0
Aspect ratio		1	20
Jacobian ratio		1	30
Warping ratio	shell elements	0	1
	solid elements	0	0.4
Parallel Deviation		0	170
Corner Deviation	three nodes	60	165
	four nodes	90	180
Skewness		0	1
Orthogonal Quality		1	0

The elements can be divided into two main categories, 2-dimensional and 3-dimensional elements. 2-dimensional elements are used to model structures in cases where the two dimensions are much higher than the third one. In these cases, the change of the analysed feature across this third direction can be neglected. The rule of thumb is that three to four linear elements are required across the feature thickness to capture the changes with appropriate numerical accuracy. With quadratic elements, two is considered to be enough.

Sometimes it is necessary to favour some other element type over the most obvious one. Like in the thesis case, it was inevitable to use tetrahedral elements over hexahedral since hexahedral element type does not support the contacts with some 2-dimensional beam type elements. All the used elements can be seen in the following table (5). Below the table, there is a brief description of the listed elements [36].

Table 5. Used element types and their quantities.

Element Name	Number of Elements
MASS21	1
SURF154	4914
TARGET170	100334
CONTACT174	102632
LINK180	40
SHELL181	13197
SOLID187	89256
BEAM188	1440
SHELL281	2152
Total	313966

- MASS21 is a structural mass element with six DOF's. Masses and inertias can be defined separately for each coordinate axes.
- SURF154 elements are used for load and surface effect applications.
- TARGET170 elements are used to represent various target surfaces for contact elements.

- CONTACT174 elements are used to represent contacts and sliding between the solid elements.
- LINK180 elements are used to model 2D elements with tension only with 3 DOF's in each node.
- SHELL181 elements are used to model moderately- thick shell structures with four corner nodes.
- SOLID187 is a typical quadratic hexahedral element with ten nodes. Well suitable for incompressible hyperelastic materials.
- BEAM188 elements are based on Timoshenko's beam theory, and they are used to model moderately thick beam structures.
- SHELL281 elements are similar to SHELL181 but with eight nodes.

3.2.1 Initial mesh quality study

Since most of the used elements in this study were solid ones, the most useful indicator for mesh quality was evaluated by using two values. These values were the orthogonal quality and skewness of the elements. First mentioned affects directly to the calculation time and how much iterations are needed for completing the computations. Orthogonal quality is defined for each face of the elements separately. The orthogonality of the cell is the smallest calculated cosine value between angles of vectors. Illustration of definition can be seen in the figure (19) [35].

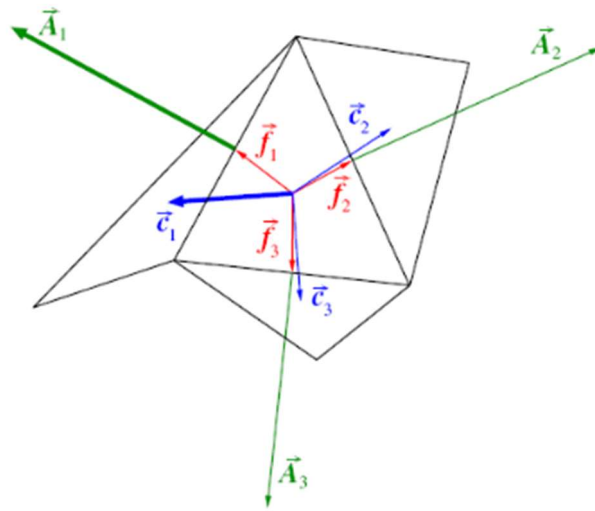



Figure 19. Vectors for defining the orthogonal quality. (Ansys, modified)

Mesh skewness is calculated by the following equation (30) [37],

$$\text{Skewness} = \frac{\text{optimal cell size} - \text{cell size}}{\text{optimal cell size}}, \quad (30)$$


where the value of quality is evaluated by volume deviation. From the following table (6) [37], one can see the illustration of the scale for the orthogonal quality.

Table 6. Orthogonal value evaluation scale (Ansys, modified)

					
Unacceptable	Bad	Acceptable	Good	Very good	Excellent
0-0.001	0.001-0.14	0.15-0.20	0.20-0.69	0.70-0.95	0.95-1.00

From the table (7) [37] can be seen the illustration for the scale of the mesh skewness.

Table 7. Skewness value evaluation scale (Ansys, modified)

					
Excellent	Very good	Good	Acceptable	Bad	Unacceptable
0-0.25	0.25-0.50	0.50-0.80	0.80-0.94	0.95-0.97	0.98-1.00

From the following figure (20), we can see the mesh metrics plotted by using the Ansys Workbench meshing platform.

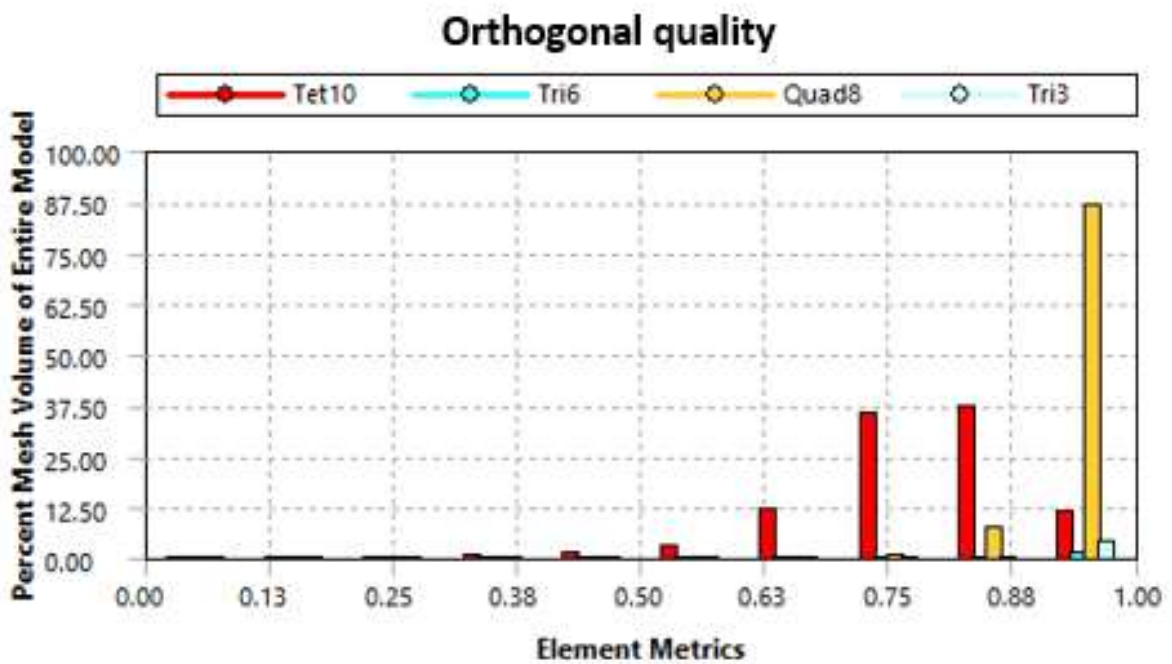


Figure 20. Orthogonal quality of the mesh

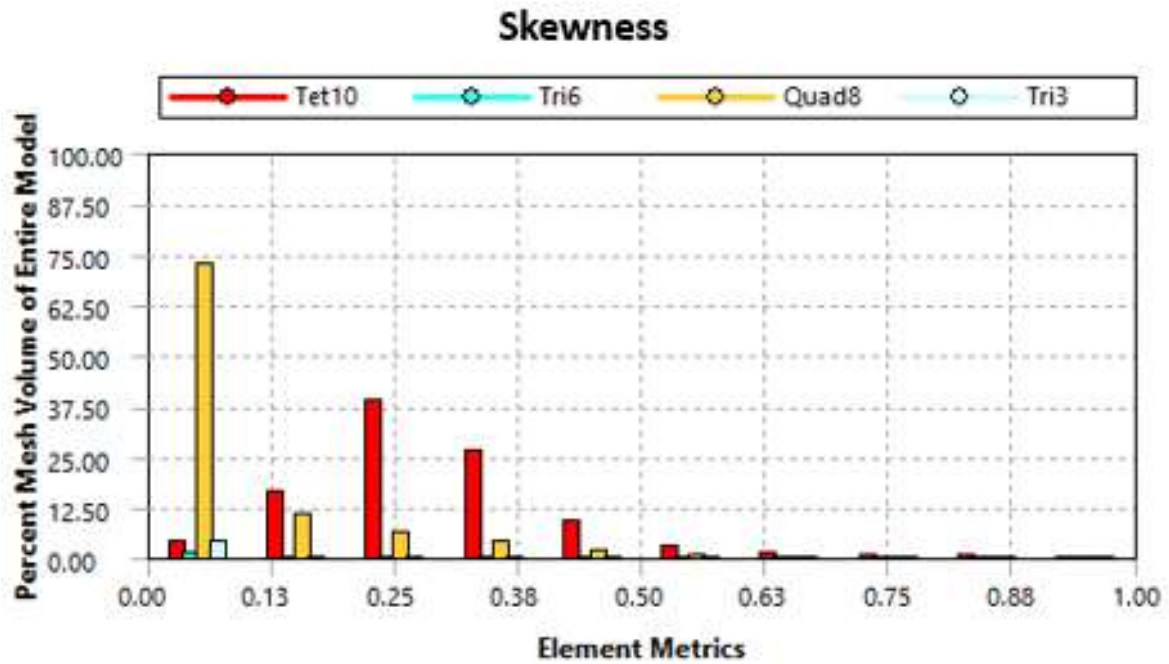


Figure 21. The skewness of the mesh

From the previous figures (21), one can see that the mesh quality can be considered to be in an acceptable range of values when measured with both criteria's, Orthogonal quality and skewness of the mesh. For orthogonal quality, the average numerical value was (0.85614 ± 0.12744) , and for skewness, the average value was (0.20724 ± 0.16002) . Main reasons for low-quality mesh units was the steep transitions in the geometry. Most of the bad quality mesh is obtained in the area of the limbus, which is the area where cornea and sclera are blended. The element model was built in such a way that the element nodes between sclera and cornea can be shared and thus make the mesh conformal. By this procedure, it was made sure that the bad quality mesh does not affect the results since they are sharing the same nodes over the different bodies. Mesh with low (< 0.25) orthogonal quality is plotted in the following figure (22).

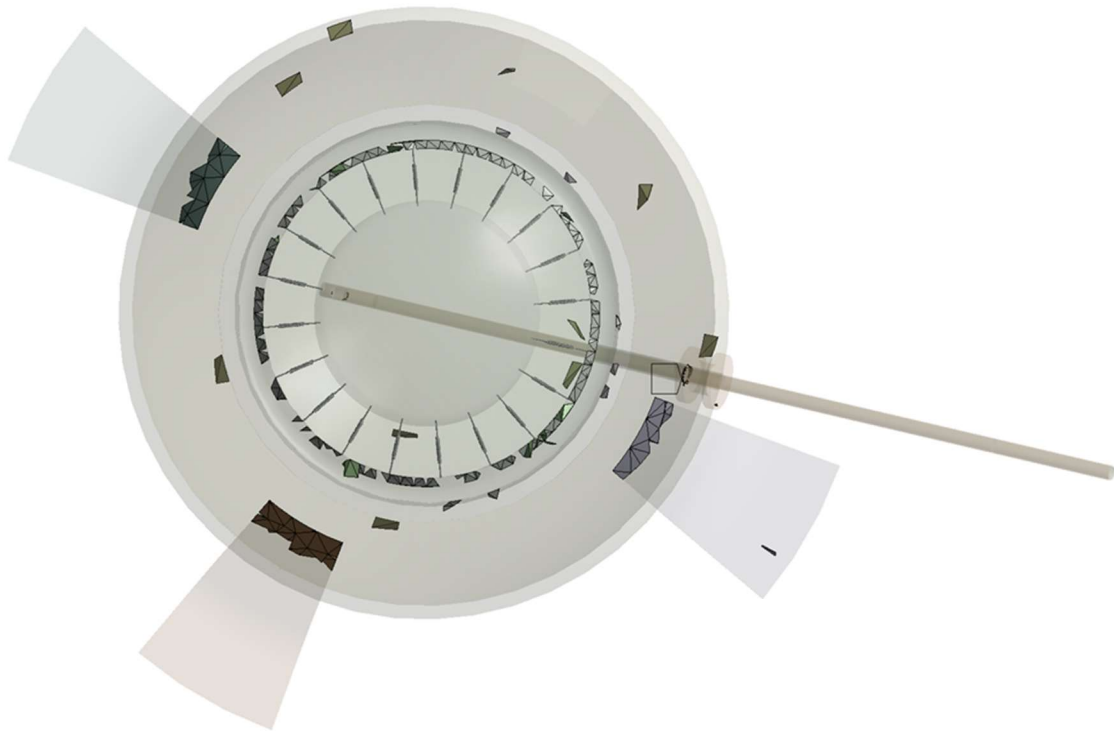


Figure 22. Mesh elements with low orthogonal quality (< 0.25)

3.2.2 Modelling Zinn's membrane

Zinn's membrane was named after German anatomist and botanist Johan Gottfried Zinn. He first described, in his groundbreaking book *Descriptio anatomica oculi humani*, the structure of ligaments holding and adjusting the lens in the human eye. Modelling such membrane which consists of individual zonular fibres may be difficult or impossible, with required numerical accuracy. Therefore, some simplifications were used. Instead of using solid or discrete beam elements to describe the behaviour of the ligaments, spring elements were used. The major difference between beam and spring element is the number of DOF's. While discrete beam element has six DOF's the spring element has only three. LINK180 elements were used to model the ligaments between the lens and the limbus area. LINK180 is a pin-jointed structure, and therefore it does not carry any moment. The speciality of this element, when compared to typical spring elements, is that this one takes load only in one direction. This feature helps to simplify the ligament fibres in the eye.

The spring elements do not carry any information about the material; therefore, in the linear form, it has to have a spring constant defined. Spring constant can be derived from Young's modulus, cross-sectional area and the length of the element. According to the definition of the force acting on the spring, force equals spring constant multiplied by the change of the length (31) [20].

$$F = k \cdot \Delta l \quad (31)$$

From the equation (31) above one can see that,

$$k = \frac{F}{\Delta l}. \quad (32)$$

A ratio between stress and strain defines young's modulus.

$$E = \frac{\sigma}{\varepsilon} \quad (33)$$

Stress can be expressed as force divided in cross-section area,

$$\sigma = \frac{F}{A}, \quad (34)$$

where A is cross-section area. Definition of strain is the ratio between the change in characteristic length and original length.

$$\varepsilon = \frac{\Delta l}{l}, \quad (35)$$

When the definition of Young's modulus is written with the help of (34 & 35), we obtain the following (36),

$$E = \frac{l}{A} \cdot \frac{F}{\Delta l} \quad (36)$$

In the form (36), one can substitute the last term by the definition of the spring constant (32). After substitution and re-arrangement, we obtain the following (37),

$$k = \frac{E \cdot A}{l}. \quad (37)$$

By using the definition (40), one can calculate the spring constant for an element. Weeber et al. used elastic values for zonular fibres, gathered in the following table (8), in their paper [38]. M.I. Kaczurowski defined in his paper that the human eye has 285 individual zonular fibres with an average diameter of 40 to 50 micrometres [39]. The characteristic length of fibres is defined by model geometry.

Table 8. Linear elastic properties of Zonular fibres

	Young's Modulus (MPa)	Poisson's ratio
Zonular fibres	0.35	0.47

By using Kaczurowski's results, geometric data and elastic properties of the fibres, the spring constant can be derived. In the model, forty LINK180 elements were used to model Zonular fibres connecting limbus and lens. Dividing the total cross-sectional area, proposed by Kaczurowski, with the number of elements we obtain a spring constant of 0.00167 (N/mm). From the following figure (23) can be seen the geometry and illustration of the spring elements.

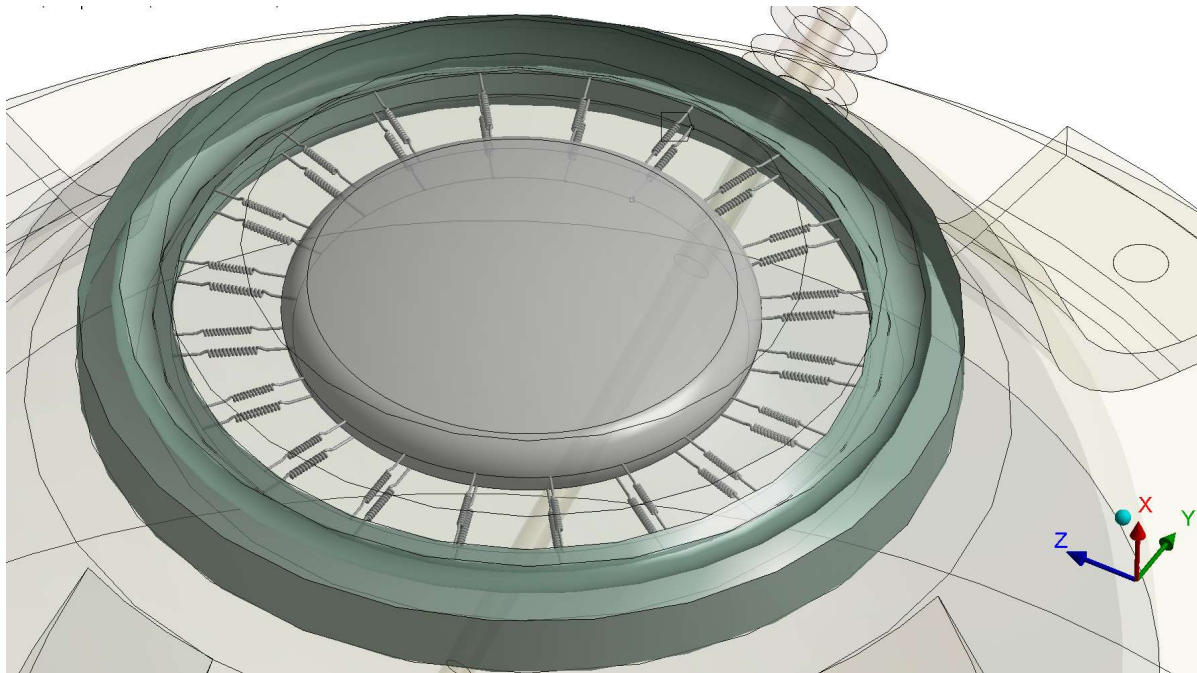


Figure 23. Lens supporting linear spring elements.

3.3 Material Testing

3.3.1 Elastic properties of combined sclera tissue

In analysed case, the material of the eye structure was simplified by assuming that the retina, choroid and sclera were all in one body. There were no given elastic properties for such case in the literature; hence, some material testing was needed. Testing was done by ing. Josef

Šepitka from the nanoindentation laboratories in CTU. The used configuration can be seen from the following table (9) [40].

Table 9. System configuration

Base instrument:	TI 950 TriboIndenter®
Additional Equipment	nanoDMA III
Probes Used	Fluid Cell Cono-Spherical

Used fluid cell tip was 10 (μm), and the specimen was loaded with the harmonic load, which had a 0.5 (μN) amplitude and 200 (Hz) frequency. Four samples were taken, and each of them was analyzed nine times, with 50 (μm) spacing. The Young's Modulus was calculated from the results by using the following equations (38 - 41) [40].

$$S = \frac{dP}{dh}, \quad (38)$$

where S is the slope of the unloading curve, i.e. unloading stiffness. In the equation, P represents the applied force, and h is the probe dislocation.

$$E_r = \frac{S \cdot \sqrt{\pi}}{2 \cdot \sqrt{A}} \quad (39)$$

In the previous equation, A represents the projected contact area of the intention, and it can be calculated for spherical probe as following (40),

$$A = \sqrt{R_C \cdot \delta} \quad (40)$$

where R_C is the radius of the tip curvature. By using these values, we can find the modulus of elasticity through the following equation (41) [40].

$$\frac{1}{E_r} = \frac{(1 - \nu_i^2)}{E_i} + \frac{(1 - \nu_s^2)}{E_s} \quad (41)$$

In equation (41), the subscript i indicates that it is indenter values, and subscript s refers to the specimen values. In the case of soft biological samples, the Poisson's ratio is generally set to (0.5). This is applicable in the instances where the material is assumed to incompressible.

From figure (24) [40], we can see an example of conventional force versus displacement curve for a indenter in fused quartz. In figure (24), there is marked the unloading curve and its slope.

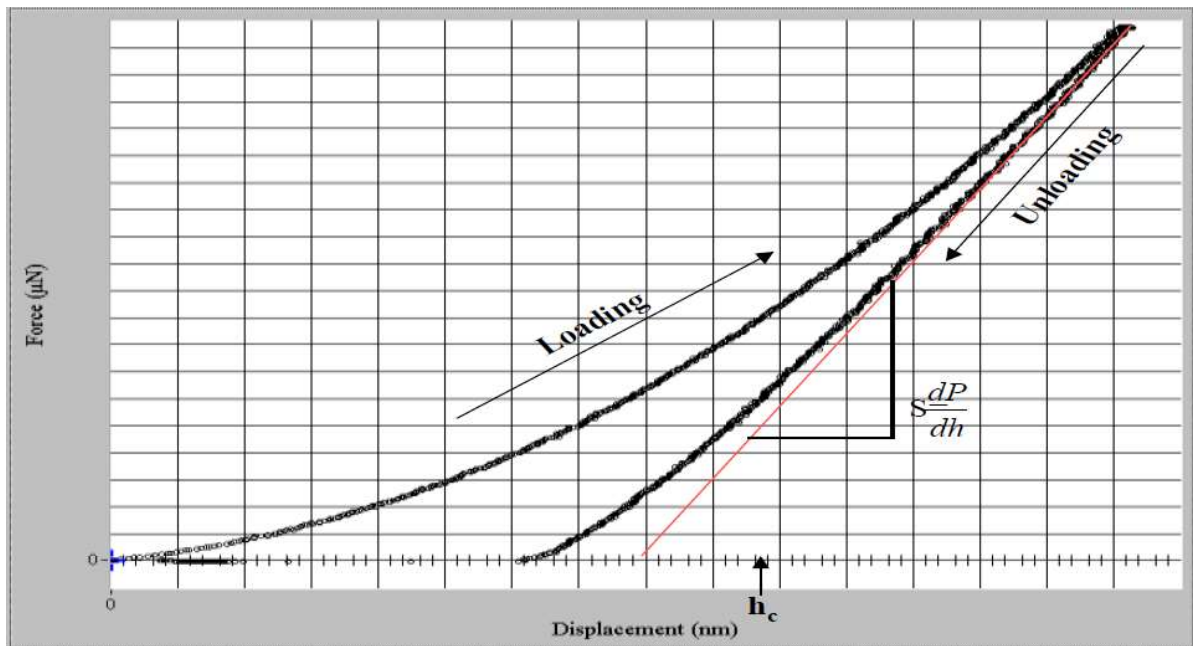


Figure 24. Force respect to displacement curve, fused quartz (Šepitka, modified)

From the table (10) [40] below we can see the results of the test with calculated standard deviation [40]. All collected data is summarized in the chapter (3.4).

Table 10. Elastic modulus of the combined body

Sample	E_s (MPa)	std (MPa)
144_L_BP	9.77	0.25
144_L_BP_UV	9.30	0.42
144_P_BP	9.75	0.68
144_P_BP_UV	19.28	0.35

As we can see from the table (10), the last sample differs from the others quite significantly. This might be caused by multiple factors. In the test, there was no information about the donators. This might be the explanation for the differences since the elastic properties are highly dependent on donors age, sex and medical condition. Grytz et al. measured in their paper which covered the human eye posterior sclera elastic modulus measurements and they ended up to an average elastic modulus of 41.83 ± 23.37 (MPa) from a group of ten donors [41]. All thought this might not explain such of a large difference between samples, but it gives a guide where to look. Therefore, the following conclusion was made, that the difference is due to some sort of sample preparation error or age / medical state of the donor. This conclusion is supported by the fact that there was no specific information about the donors of the samples. After all, the exact reason for the difference between the results cannot be stated.

3.3.2 Elastic properties of GRIN lens

Since the lens makers are using their protected glass compositions and the elastic modulus of the typical optical glass are spread in a broad spectrum, the elastic properties of the lens needed to be tested. Testing was proceeded by doc. Ing. Jan Hošek, PhD and Ing. Šárka Němcová,

PhD from the CTU Faculty of Mechanical Engineering. According to their results, Young's modulus of GRIN lens is $E = (71 \pm 4)$ GPa [42]. They also found that the value fits good in the range of literature values of optical glass elastic properties. Their results are being summarized in table (11) [42].

Table 11. GRIN lens material properties

Young's modulus	Maximum bending moment	Specimen diameter	Minimum bending curvature
E (GPa)	M_{max} (Nmm)	D (mm)	ρ_{min} (mm)
71 ± 4	1.8 ± 0.1	0.475 ± 0.0047	97 ± 6

By using these values, we can calculate the maximum bending stress with the following formula (42) [20].

$$\sigma = \frac{M_{max}}{S} \quad (42)$$

Where S is bending section modulus, and it can be calculated as following (43) [20],

$$S = \frac{I_z}{y} \quad (43)$$

Where I_z is the second moment of area and y is the position of the neutral axis, which in this case lies in the middle of the object. When applying values, the maximum bending stress from the lens surface is obtained ($\sigma_{max} = 171.1_{-4.6}^{+4.2}$ MPa).

3.4 Material Models

In some parts of the global model, linear elastic material models were used. Elastic properties can be seen from the following table (12).

Table 12. Linear elastic material models.

Material	Young's Modulus (MPa)	Poisson's ratio	Density (kg/m ³)	Source(s)
Phynox	203 400	0.31	8300	[43]
Stainless Steel	193 000	0.31	7750	[44]
GRIN lens	71 600	0.21	2600	[42] [45]
Scelera tissue combined	9.6	0.49	997	[40] [46]
Ligaments	0.35	0.5	997	[38]
Lens	0.82	0.47	997	[47] [48]

The rest of the eye was modelled by using hyperelastic materials. This concluded several parts including lens, zonule of Zinn (ligaments), sclera and cornea. All hyperelastic properties were gathered from literature and cross-verified from several sources, if possible. Hyperelastic properties for nH models can be seen from the following table (13). All the numerical data can be found from appendices (Appendix 4)

Table 13. Material parameters for the nH hyperelastic material

Material	D_1 (Pa ⁻¹)	G_0 (Pa)	Source(s)
Sclera	1.53E-07	799319.73	[46] [49]
Cornea	3.31E-06	102112.68	[50] [49] [51]

In the table (14) is listed the material parameters for MR hyperelastic material models. The first values are based on fitting done in Ansys curve fitting tool. The data used for fittings was gathered by Wollensak et al. in their study of stress-strain measurements of human and porcine eyes [52] and Uchio et al. in their study of the simulation model of an eyeball based on finite element analysis on a supercomputer [49]. The second models are derived from linear elastic data given by Uchio et al., Hamilton et al. & Friberg et al. in their papers. The values were derivated by using equations presented in the chapter (2). The models are separated by sub notes (f) and (c), which indicates the way how the data was processed. The data and the fittings can be seen in the following figures (25 & 26). All the numerical data can be found from appendices (

Appendix 5 & Appendix 6)

Table 14. MR material parameters

Model	D_1 (Pa ⁻¹)	C_{10} (Pa)	C_{01} (Pa)	C_{11} (Pa)	Source
Sclera 2-term MR.f	1E-05	-6.9973E+07	9.4547E+07	-	[49]
Cornea 3-term MR.f	1E-05	-1.6435E+06	1.8219E+06	4.2157E+06	[52]
Sclera 2-term MR.c	1.53E-07	3.9966E+05	4.66E-10	-	[49] [46]
Cornea 2-term MR.c	3.31E-06	51056.34	0	-	[50] [49]

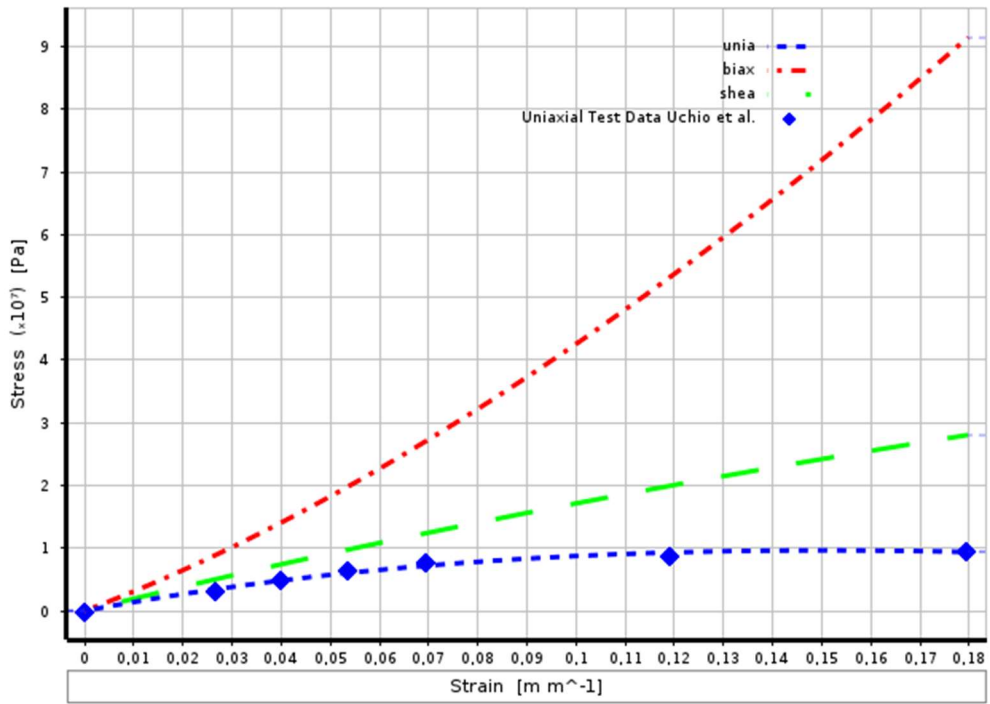


Figure 25. Data and fitting for sclera 2-term MR

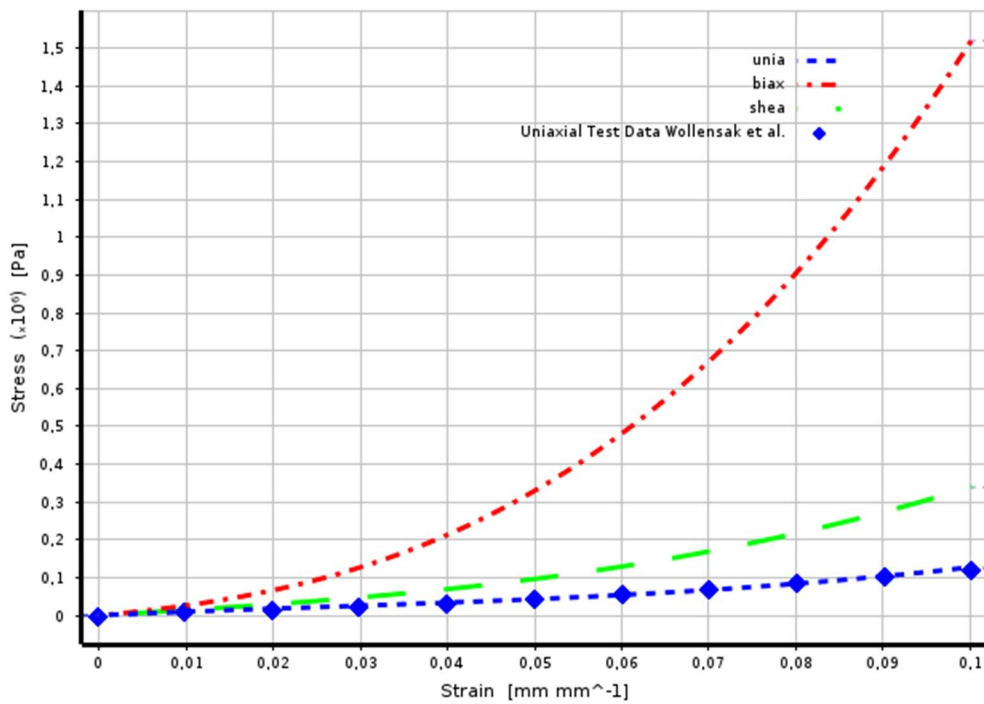


Figure 26. Data and fitting for cornea 3-term MR

From figure (27) can be seen the different material models used in the analysis.

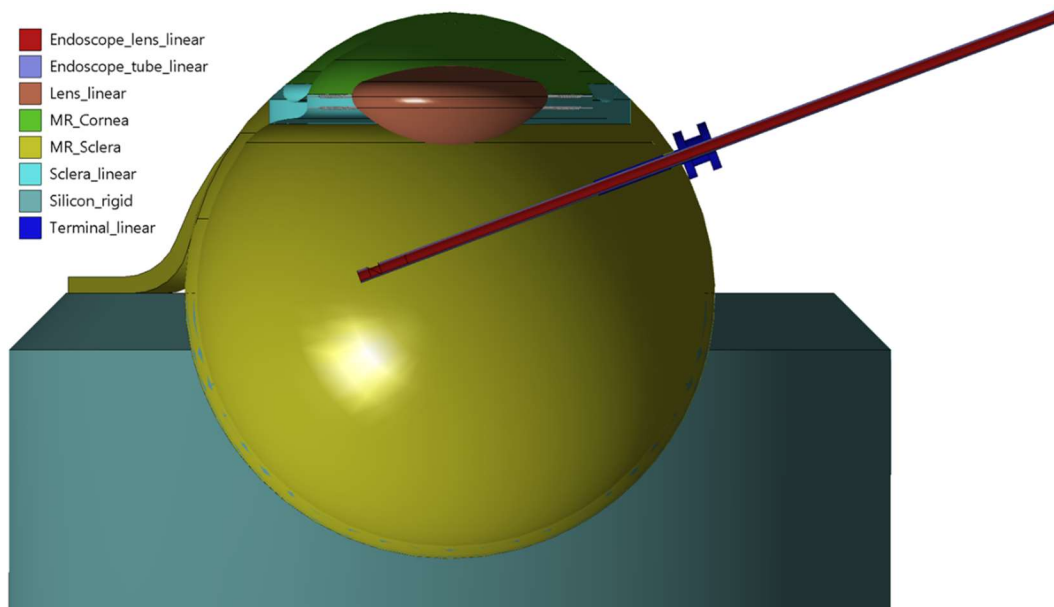


Figure 27. Different materials visualized in the geometry.

3.5 Contacts

A contact is an event when two separate surfaces touch each other and become mutually tangent. In the physical sense, two surfaces which are in contact have few common characteristics. Firstly, they do not interpenetrate. Secondly, they are transmitting normal forces and possibly some tangential forces due to the frictional behaviour, and they often do not transmit tensile forces of any kind. In FEA, contacts are defining the structural interaction between different bodies. However, contacts are typically highly non-linear features in the analysis and therefore, they come with the cost of computational time and convergence problems. Five contact behaviours are available. The different contact types and their characteristics are listed in the table (15) [53] below.

Table 15. Contact types and their characteristics

Contact	Iterations	Normal behaviour	Tangential behaviour
Bonded	1	No gaps	No sliding
No Separation	1	No gaps	Sliding allowed
Frictionless	Multiple	Gaps allowed	Sliding allowed
Rough	Multiple	Gaps allowed	No sliding
Frictional	Multiple	Gaps allowed	Sliding allowed

From the table (15) above we can see that the *Bonded* and *No Separation* contacts are linear and require only one equilibrium iteration, in case there are no other nonlinearities, whereas rest of the options are non-linear.

Contacts are playing a vital role when modelling the interaction between different bodies in FE analysis. They allow bodies movements respect to each other and relief stress from points where stress does not occur in real-life applications; therefore, it is vital to consider carefully different options of available contacts. One of the most significant issues, when modelling contacts between bodies, is to create sufficiently accurate model behaviour with decent calculational time. Understandably, some interactions need to be simplified, sometimes even drastically to achieve even some numerical results. Because of the nature of contacts, their nonlinear effects are always needed to take under consideration when reading the results. Sometimes the results are evaluated, on purpose, too conservative. This type of situation might be caused by a physical problem which is too complex to be modelled with acceptable numerical accuracy. The key factor is to recognise the source of error in boundary conditions and take that into account when reading the final results.

In the analysis many of the contacts were simplified since, modelling a pin fixed rectus muscles would have been too expensive in terms of calculation time. Therefore, benefits gain

from an accurate model would not have provided any value for the model when compared to simplifications. Three contact types were used in the analysis: *frictional*, *frictionless* and *bonded*. From those types only bonded is linear contact and, both, frictional and frictionless were non-linear contact types. These specified contact types were used because the linear counterparts, like *no separation* or *bonded* can stiffen the contact too much and therefore, distorts the results.

Frictionless contact setup is unilateral, which means that the normal pressure equals zero if there is a separation between the contact elements. Hence, gaps may occur between two bodies depending on the boundary conditions. The frictionless solution is non-linear because the area of the contact is not constant. This is hugely dependent on the applied loading. Since the contact type has a friction coefficient equal to zero, some weak springs may be needed to stabilise the model.

In frictional contact setup, two contacting elements can carry shear loading at a certain point. After this limit is crossed the contact setup allows contact elements to slide relative to each other. This point when the applied shear exceeds the limit is called sticking. This may be seen in the solution convergence as a sudden peak. The frictional model defines equivalent shear stress at which sliding on the geometry begins as a fraction of the contact pressure.

Bonded contact is, as the name tells, bonded. In this contact type, the two contact elements are literally glued to each other. Hence, they cannot move or form a gap relative to each other. Bonded contact is a sort of particular contact type since there is no contact, but instead of that, the bodies are behaving like they were one piece. This contact type requires, usually, conformal meshing. This is because the mesh is approximating the transitions of the geometry, and there might occur some infinitely sharp edges or overlapping surfaces which can create a local stress concentration in the result. This might cause some convergence issues too.

3.5.1 Contact Algorithms

In the physical sense, two contacting bodies do not interpenetrate. Therefore, in FE analysis, the contact elements need to have enforced contact compatibility. For this, there are several different contact algorithms available in common FE analysis tools. In this analysis, mostly penalty-based algorithms were used. In bonded contacts multipoint contact, further MPC, formulation was used. The significant difference between MPC and penalty-based contact formulations are the connection between contact element nodes. Penalty-based algorithms are creating spring elements between the contact element nodes, whereas MPC formulation uses rigid beam elements.

In the analysis, penalty-based algorithms were used in the non-linear contacts. This was due to the robust behaviour and better convergence. There are two penalty-based formulations available in Ansys, pure penalty and augmented lagrange. Both of these formulations are based on contact stiffness and allow penetration. Schematic drawing of contact can be seen in the following figure (28) [54].

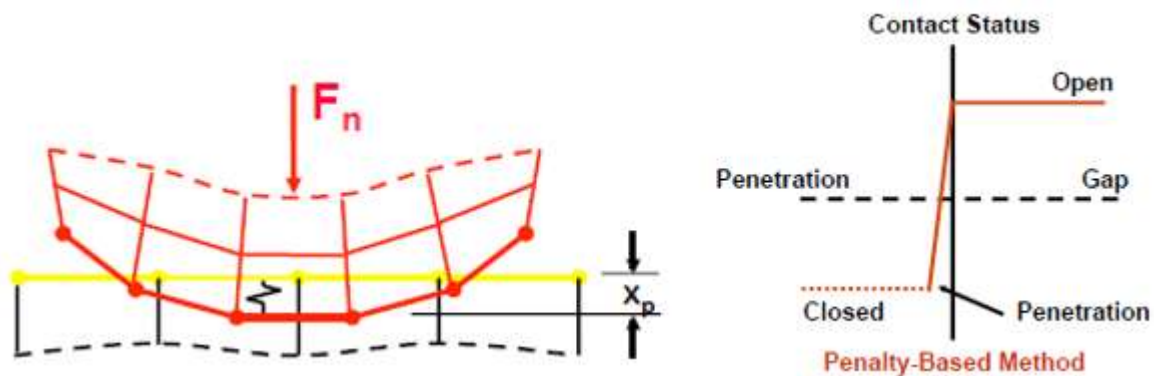


Figure 28. Contact characteristics (Ansys, modified).

Both penalty-based contact formulations can be expressed as following (44) [55].

$$F_{normal} = k_{normal} \cdot x \quad (44)$$

In the equation F_{normal} is the contact force, k_{normal} is the contact stiffness and x represents the penetration depth. In an ideal situation, the penetration depth is zero, but this is not numerically possible with these penalty-based methods, since it would require an infinite stiff contact. By using the normal stiffness, one can control the amount of penetration between contact elements. As long as the penetration is small or negligible, the solution results are accurate. What makes the augmented lagrange so robust is the extra term in the equation (45) [55]

$$F_{normal} = k_{normal} \cdot x + \lambda_{langrange} \quad (45)$$

Because of the extra term in the equation, the formulation is less sensitive to the magnitude of the contact stiffness. The normal contact stiffness is the most important parameter which affects both convergence and accuracy of the results. Too high initial stiffness can cause model instability. This is due when contact stiffness exceeds the applied force, and the contact element pair starts to oscillate when bouncing between the iterations. The contact stiffness is updated automatically between each equilibrium iteration or substep. The program assumes that the initial contact stiffness is equal to one, but in the analysis (0.1) was used as an initial stiffness in penalty-based contact pairs, since the problem is mostly bending dominated. This makes contact easier to convergence but allows more penetration.

3.6 *Contacts in the model*

Contacts used in the analysis can be seen in the following figures (29-31). All the contact details are listed in the tables (16).

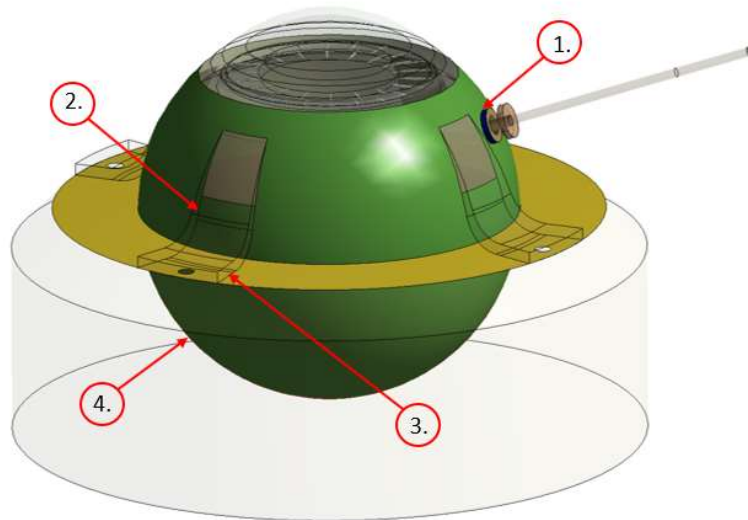


Figure 29. Frictionless contacts

In the model, frictionless contacts were applied between the outer surfaces of the terminal and the sclera (1), rectum muscles and sclera (2), rectum muscles and silicone holder (3) and sclera and silicone holder (4).

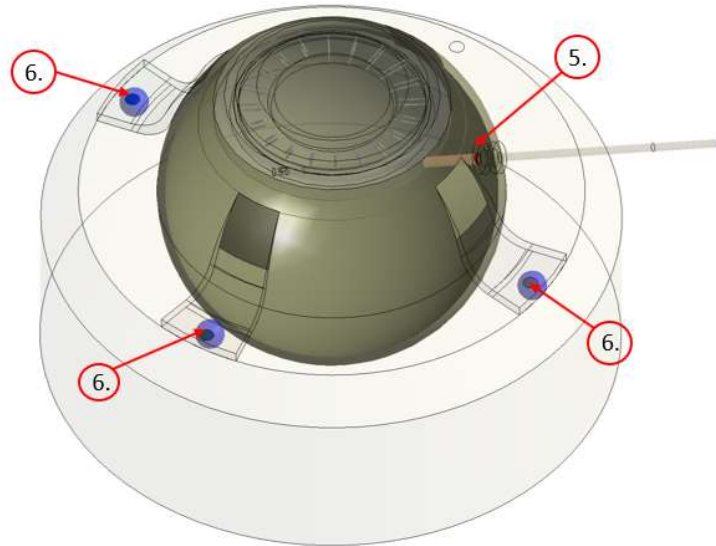


Figure 30. Bonded contacts

Boded contacts were applied between the terminal tube and the sclera (5) and the surface under the rectum muscles and the silicone holder (6). The bonded area between rectum muscles and silicone holder was $0.785 \text{ (mm}^2\text{)}$. In addition to above, bonded contact was also applied surfaces between the endoscope tube and the optical elements.

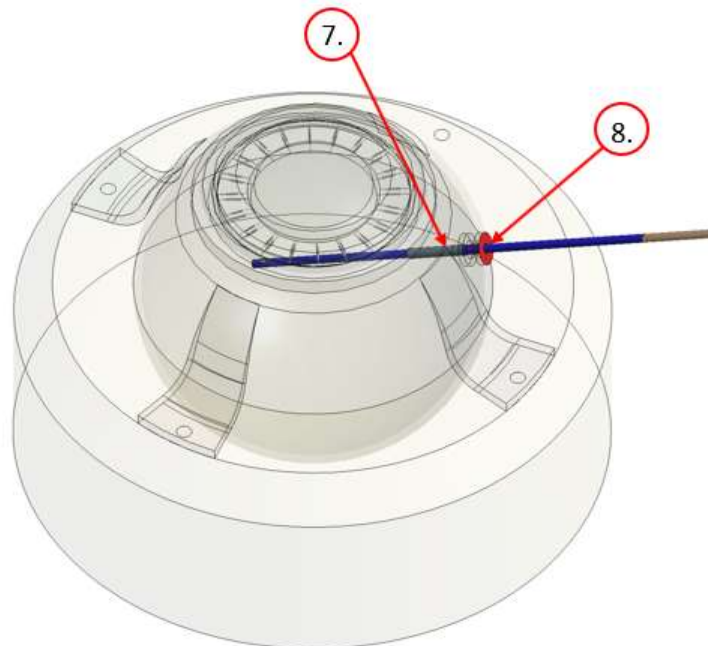


Figure 31. Frictional contacts

Frictional contacts were applied between the endoscope probe and the terminal inner surface (7 & 8).

Table 16. Contact details

Contact	Type	Formulation	Normal stiffness factor	Pinball region [mm]	Interface treatment	Friction coefficient
1	Frictionless	Augmented lagrange	0.1		Touch	
2			0.1		Touch	
3			0.1		Touch	
4			0.1		Touch	
5	Bonded	MPC	-	1	-	
6			-	1	-	
7	Frictional	Augmented lagrange	0.1		Touch	0.2
8			0.1		Touch	0.2

3.7 Boundary conditions

A boundary condition for the model is the setting of known values for displacement or applied load. Therefore, it also considers the constraints that represent the effect of the surrounding environment on the model. In this study, the boundary conditions were defined by the help of the ophthalmologist surgeon who gave some insights into the operational use of the endoscope. Hence, the maximum dislocation of the endoscope probe was defined as a worst-case scenario.

In the analysis, remote displacement was used to simulate the surgeon hand movement. Because the worst-case scenario assumption the connection to the endoscope probe has all the other DOF's locked besides the translational movement on global Z+ direction, which was set to 5 (mm). From the following figure (32), one can see the remote displacement boundary condition and the orientation in the global coordinate system.

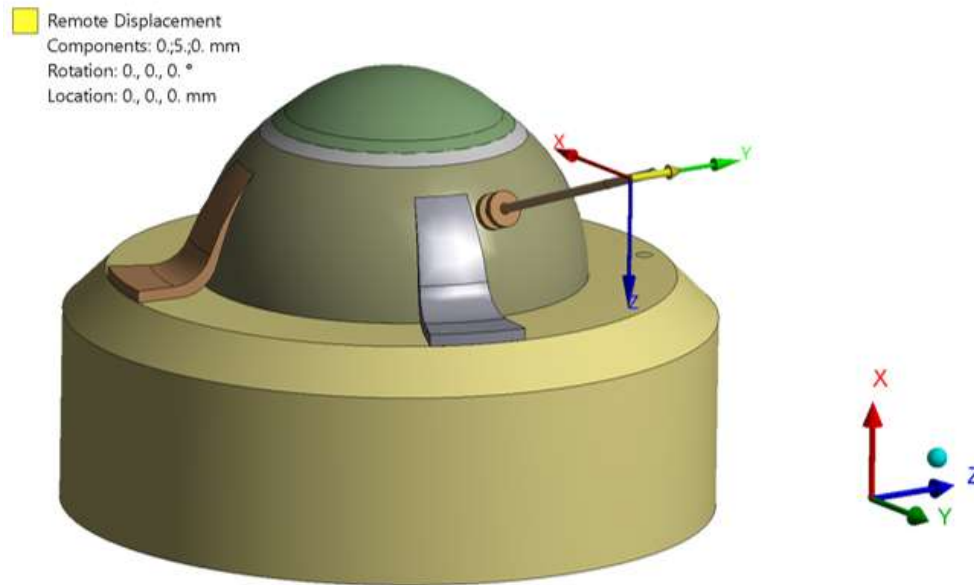


Figure 32. Remote Displacement.

During the surgery, the Vitreous Humor is removed, and it is replaced by some low viscous gas or water. The pressure is kept in the level of a healthy eye, which is 15 (mmHg). In the analysis, the pressure load was applied evenly on the inner surface of the eye. This can be seen from the following figure (33).

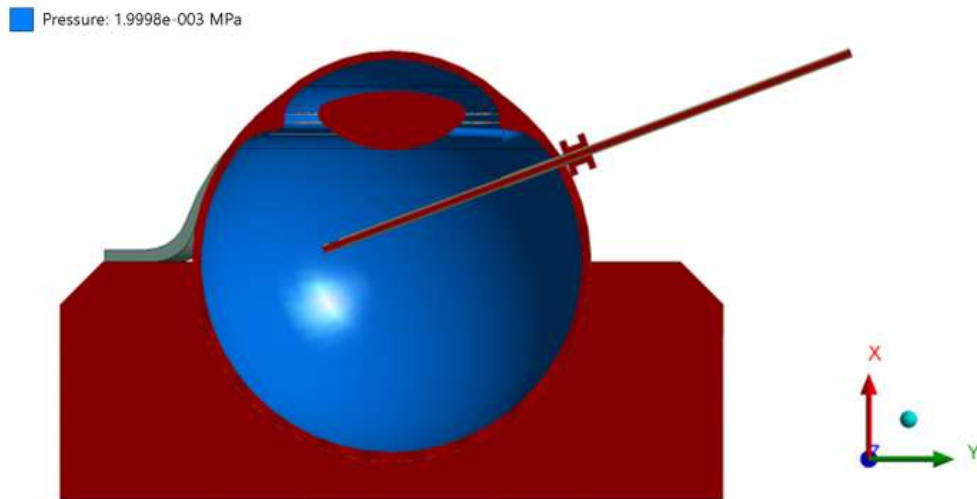


Figure 33. Pressure load inside of the eye.

In the analysis, the eye holder was assumed to be a rigid body because when compared to the elasticity of the eye, the elasticity of the holder can be neglected. This rigid body was fixed to the ground from the bottom by using joint constraint. The joint constraint can be seen from the following figure (34).

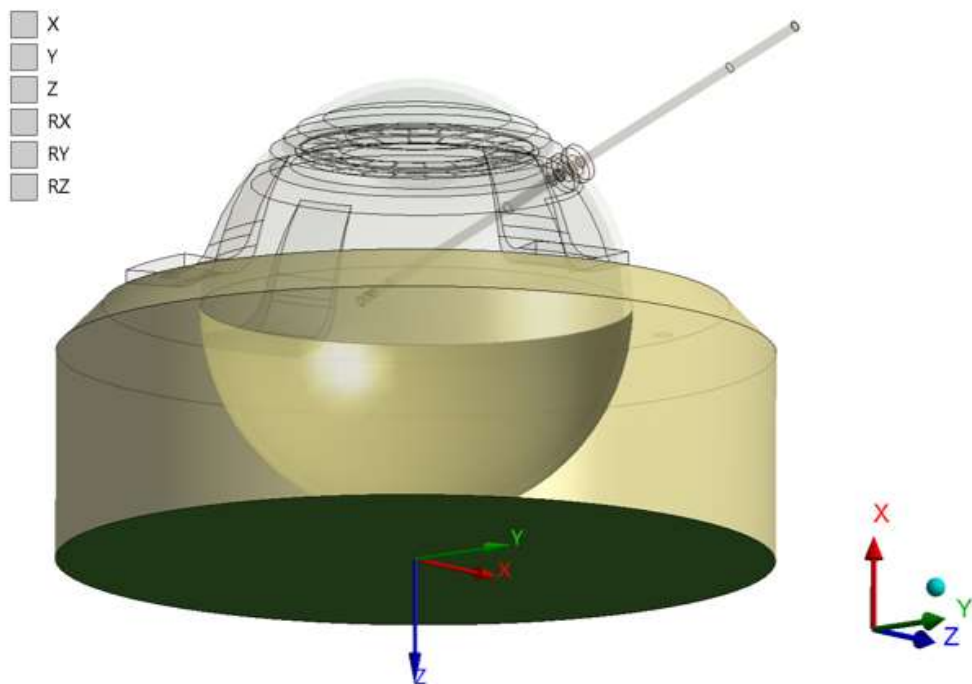


Figure 34. Joint constraint.

3.8 Solver

In FE analysis programs usually provide few different solver types to choose from. They can be divided into two main categories, direct and iterative -solvers. In the direct method, the program tries to solve the whole problem at once, and iterative solver chooses initial guess and then gradually move towards the correct solution until it satisfies the residual tolerance value.

In direct solver, the problem is usually described as in equation (8) in the previous chapter (2.1.4). The direct solver tries to find the inverse matrix $[K]$ and then multiply it with $\{F\}$ vector. Because the method involves inverting the stiffness matrix, it is usually considered for the problems which are less expensive in the computational matter. Although, this is highly depending on the capacity of the physical memory allocated for the solver. Ansys solver uses lower-upper composition for the factorising the stiffness matrix in three pieces lower, diagonal and upper -part [56].

In the thesis problem, the sparse direct solver was used. It is the most used solver type in the program, and it is capable of handling most of the problems associated with FE analysis. A sparse matrix is a matrix where most of the elements are zero. For dealing with a large matrix containing a lot of zeros is not a memory-wise. Therefore, substantial memory requirement reduction can be dealt with storing only non-zero elements in separate arrays. A rule of thumb is that direct solver requires 1 gigabyte of memory per one million DOF's and 10 GB disk space per million DOF's. The problem analysed in this work had (508134) DOF's. The used solver setting can be seen from the following table (17).

Table 17. Used solver settings

Solver	Weak sprigs	Pivot checking	Large deflections	Inertia relief
Direct sparse	NO	NO	YES	NO

3.9 Mesh convergence study

In FE modelling, typically, a finer mesh results a more accurate solution. On the contrary, when increasing mesh density, the calculation time increases. Therefore, it is crucial to know how fine mesh is needed in order to get acceptably accurate results in a balance to the computational resources. For this matter mesh convergence study can be performed.

Usually, the effectiveness of mesh is presented in a convergence curve. The curve is plotted to some critical parameter respect to the mesh density. A minimum of three-point is required to make a fitting to predict the optimal mesh density to reach the full convergence. In this, St. Venant's principle needs to be taken into account. The principle implies that local hotspot stresses do not affect the stresses elsewhere. From this point of view, one should be able to determine the optimal mesh density just by refining the elements in the regions of interest. These local stress concentration points can be caused by bad curvature representation of the current mesh or perhaps a boundary condition. With mesh convergence study, the first option can be easily ruled out.

In this study, the local mesh refinement was more than a convenient approach since the mesh of the eye and rectum muscles are only in the role of transmitting loads and damping the endoscope movement. Hence, those elements can be considerably larger than the stress indicating elements in the endoscope parts. From figure (35), the results of the mesh convergence study can be seen. The mesh convergence study was executed manually to a sub-

model which included only a part of the endoscope probe. The mesh parameters were updated only in the region of interest, and all the numerical data is gathered in the table (18) below.

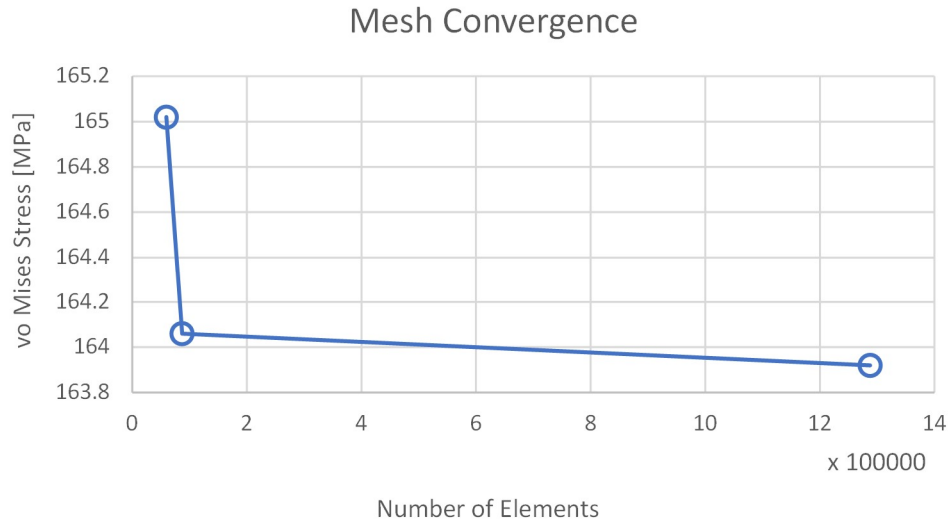


Figure 35. Mesh convergence curve.

Table 18. Mesh data.

Element size [mm]	No. of Elements	No. of Nodes	Stress [MPa]	No. of Elements over the thinnest geometrical feature
0.1	59446	104101	165.02	1
0.08	86981	149663	164.06	1
0.032	1287626	1586260	163.92	2

From the mesh convergence study can be seen that the initial mesh density was sufficient for the calculations, and increasing the density does not increase the stress in the local area of interest.

4 EXPERIMENTAL MEASUREMENTS

The purpose of the experimental measurements was to gather the necessary information about the specimens and to verify the numerical results calculated by FEM. The experimental measurements proceeded in CTU lab on Twenty-first of July, 2020. The experiment concluded three parts. First one was the verification of the FE analysis by using a strain gauge and video data. The second one measured the outer curvatures of the porcine eyes by using 3D scanning. The third one was to examine the wall thickness of the sclera. All the gathered data was used to improve the accuracy of the FEA and to verify the results. All the measurement procedures are described in the following chapter in detail.

4.1 FEA verification setup

In the verification setup, a real-life endoscopic examination procedure was replicated. The setup mimics a situation where a surgeon is examining or operating a human eye with the endoscope. Because the purpose of this work is to study the endurance of the endoscope probe, a worst-case scenario was created. The scenario can be described as following: Surgeon moves the endoscope during the examination a distance of five millimetres. This movement was not limited by force, and the only flexible objects are the eye, terminal and the endoscope probe. The result deformation- and stress data were compared to the FE analysis results to find a hyperelastic material model which corresponds to the modelled situation. A schematic of the situation can be seen from the following figure (36). In the figure, rigid parts are marked with red rectangular areas.

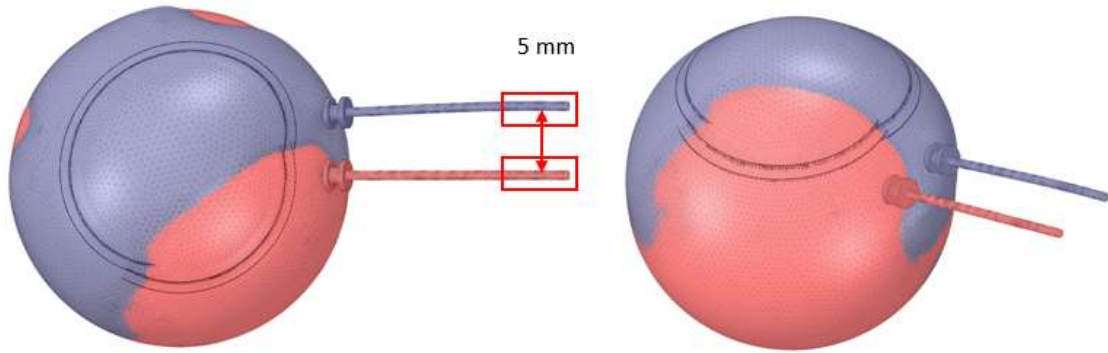


Figure 36. Tested scenario illustration.

The movement was done by using an Igus linear unit and an Applied Motion Products step motor. The motor was connected to a trapezoidal screw with a 2 mm pitch. The screw turned the rotational motion into linear motion of a slide which was running over guide profile made from aluminium. The step motor was controlled with Arduino UNO and an external microswitch. Power to each equipment was taken from a Manson EP-613 power source. The endoscope probe was replaced by standard 23G needle with a Kyowa KFGS (1N-120-C1-11) strain gauge attached to it. The needle and strain gauge can be seen from figure (40). Second strain gauge, acting as a temperature reference, was connected with the stressed gauge in the quarter bridge to the HBM Scout 55 mobile amplifier. The connection diagram is presented in the following figure (37) [57].

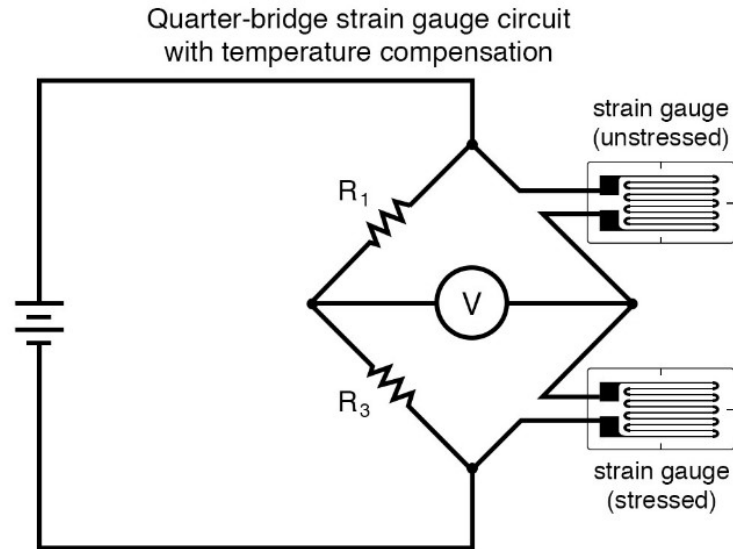


Figure 37. Quarter-bridge connection (All about circuits, modified)

The analogue strain gauge signal was connected to a computer via National Instruments BNC-2120 connector block, and data was logged with the LabView program. The needle was mounted to a metallic holder (figure 40) with a collet so that all the DOF's of the needle were locked. The holder was mounted to a Vertex magnetic dial gauge stage which was fixed to the slide with two M6 thread and aluminium bar like we can see from the figure (39). The specimens were porcine eyes which were delivered fresh from the butchery at the experiment day (21st of July 2020) and were stored in the fridge in six to eight degrees of Celsius. For every test, the sample was prepared and fixed to the silicone cup with needles. After that, the silicone cup was inserted to a holder made from black PLA plastic by 3D-printing. The holder can be seen in the figure (40). Because the position of the needle was pre-set and fixed, the specimen holder was taken out between every test. The holder and specimen were re-attached to the same position by the help of the laser pointer, which pointed out the position of the needle terminal. After this, the holder fixed to the ThorLab Breadboard PBH51501 platform with two M6 Allen bolts and levers and the bolts were tightened up with Allen key.

To ensure the even illumination, Elementrix RG3 24w led light source, was used to lighten the experiment stage. The whole experiment was recorded with two cameras, one for the top view and another one from the side view, parallel to the loading direction. The stage was

covered with green paper from each recorded direction to ensure that the background colour enables easy video data post-processing. Cameras and light accessories were mounted on the extruded aluminium profiles with an external size of 40 mm x 40 mm. The aluminium profiles were mounted to the portable optical board with M6 hardware. The test setup with numbered instruments can be seen from the following figures (38 to 42). Used instruments are labelled in the table (19) below. The sledge movement directions are marked with red arrows in the following figure (38).

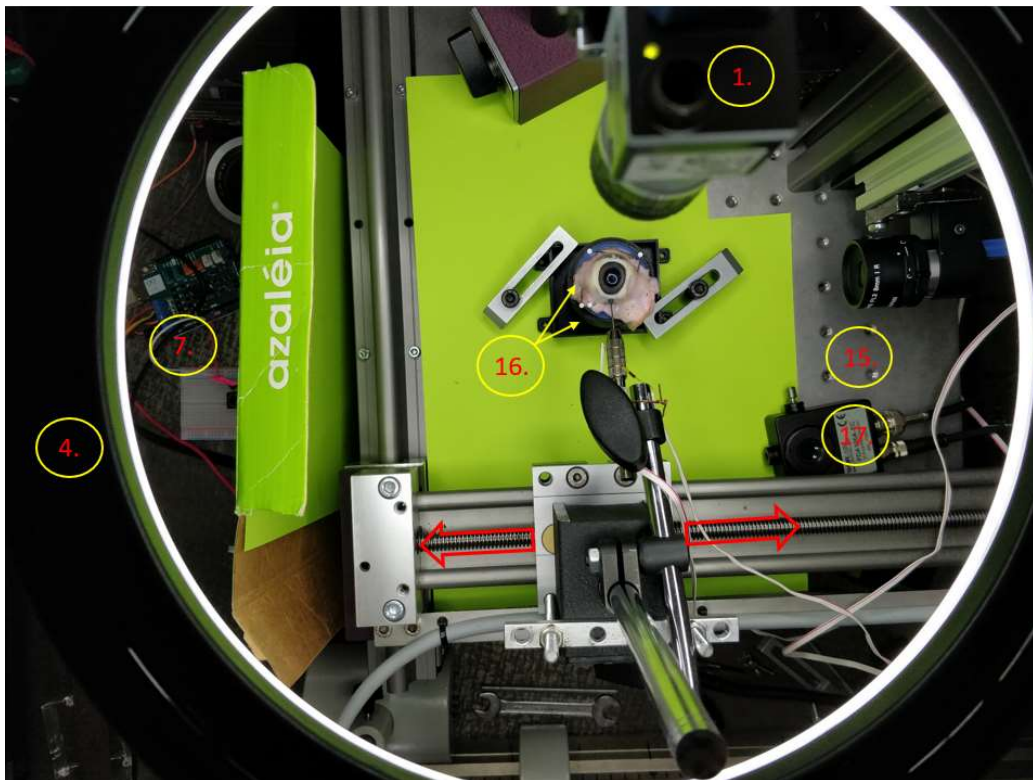


Figure 38. Test setup from up

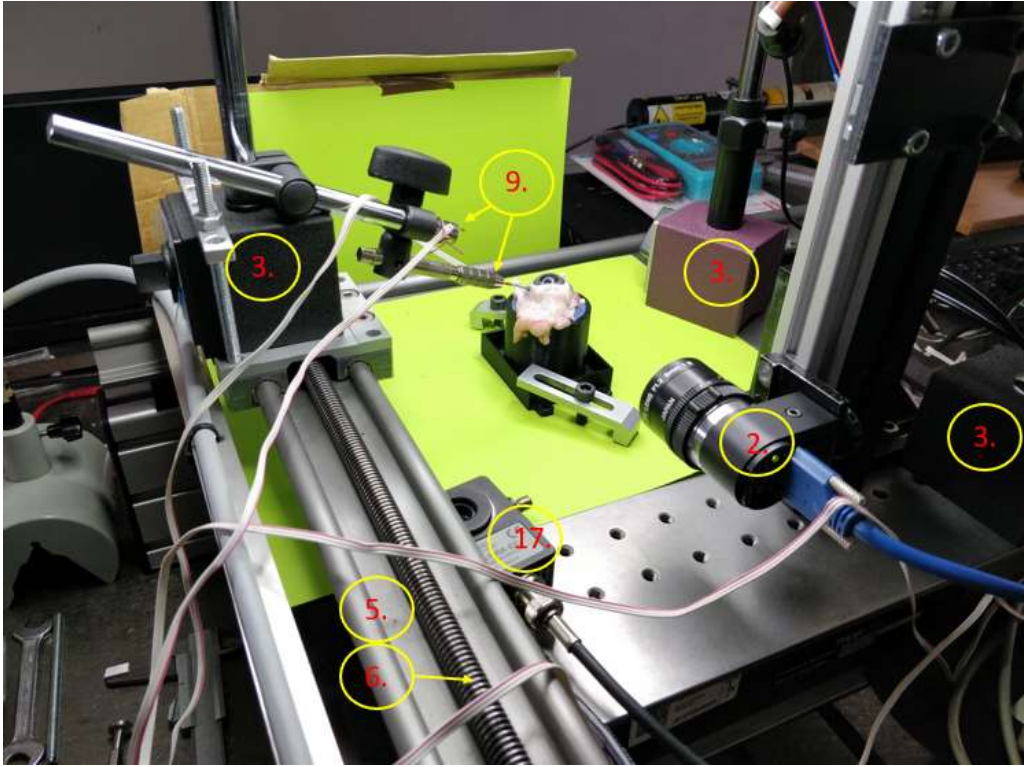


Figure 39. Test setup from upright

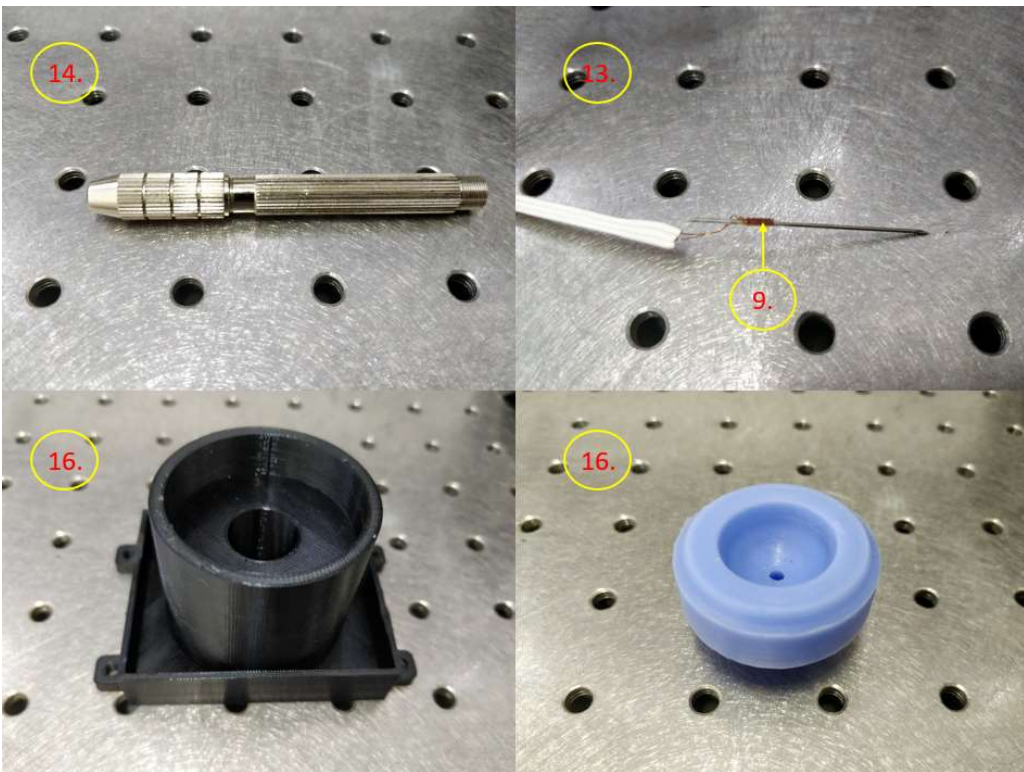


Figure 40. Holder and needle used in the experiment.



Figure 41. Amplifier and power source used in the experiment.

Table 19. Instruments used in the FEA verification

Number	Model (description)
1.	Basler a cA3088-57uc camera
2.	Hummingbird SMX-15M5C camera
3.	3 x Vertex magnetic dial gauge stage VMB-B
4.	Elementrix RG3 24w led light source
5.	Applied Motion Products, Step motor, HW23-753(12/14)
6.	Iigus GmbH, linear unit 4018139 001 002
7.	Arduino UNO and microswitch
8.	HMB Scout 55, mobile amplifier
9.	Strain gauge, Kyowa KFGS 1N-120-C1-11
10.	Computer with LabVIEW and software for recording camera image

11.	Manson EP-613, power source
12.	National Instruments BNC-2120 connector block
13.	23G Hypodermic needle, Deep Blue
14.	Rigid steel needle holder
15.	ThorLabs Breadboard platform PBH51501
16.	Silicone / plastic holder for the specimen
17.	ThorLabs Switchable Gain Detector 340 – 1100 nm, sensor

4.2 Test sequence

In the experiment, a needle with a strain gauge installed on it moved a pre-defined sequence (number 5 in the following figure) programmed in Arduino Uno. The sequence was 5 mm linear movement in both directions with the speed of 1 (mm/s) and 500 (ms) pause following the same sequence with increased speed of 2 (mm/s). From figure (42), we can see the steps of one measuring loop expressed in flow chart form.

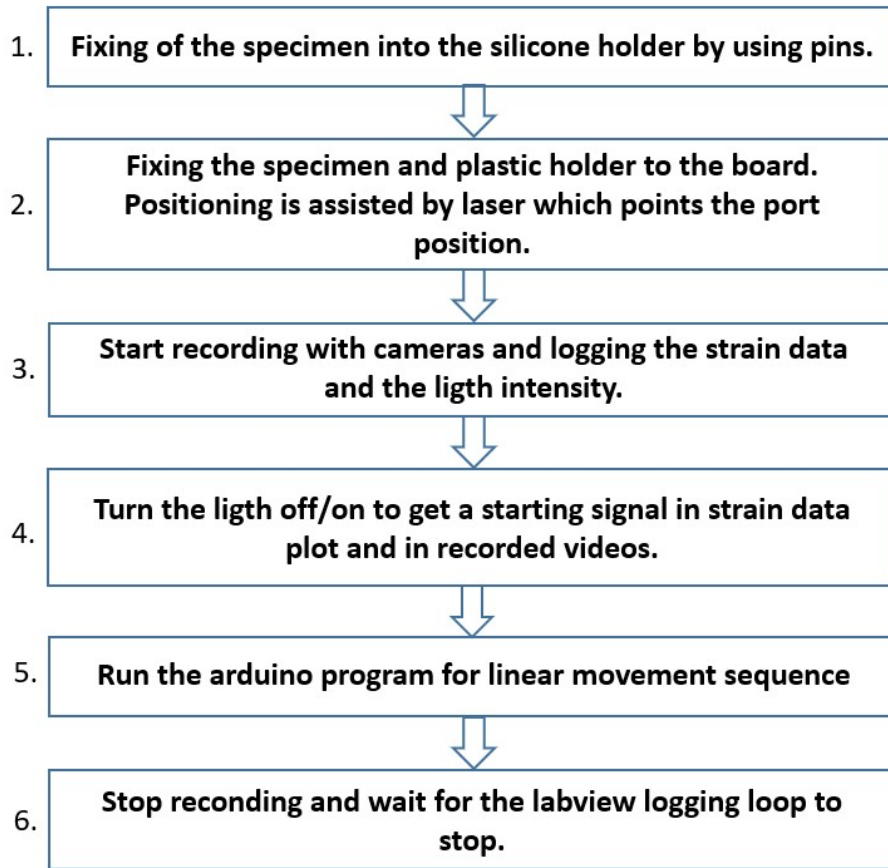


Figure 42. Flow chart of the measuring protocol.

4.2.1 Determination of measurement uncertainty of stress

For determining the strain gauge measurement uncertainty, method of GUF (a guide to the expression of uncertainty framework) uncertainty was used. This method combines statistic processing of the results and the estimated quality of the measurement process. All the possible sources of the measurement uncertainties can be seen from the following figure (43) [58].

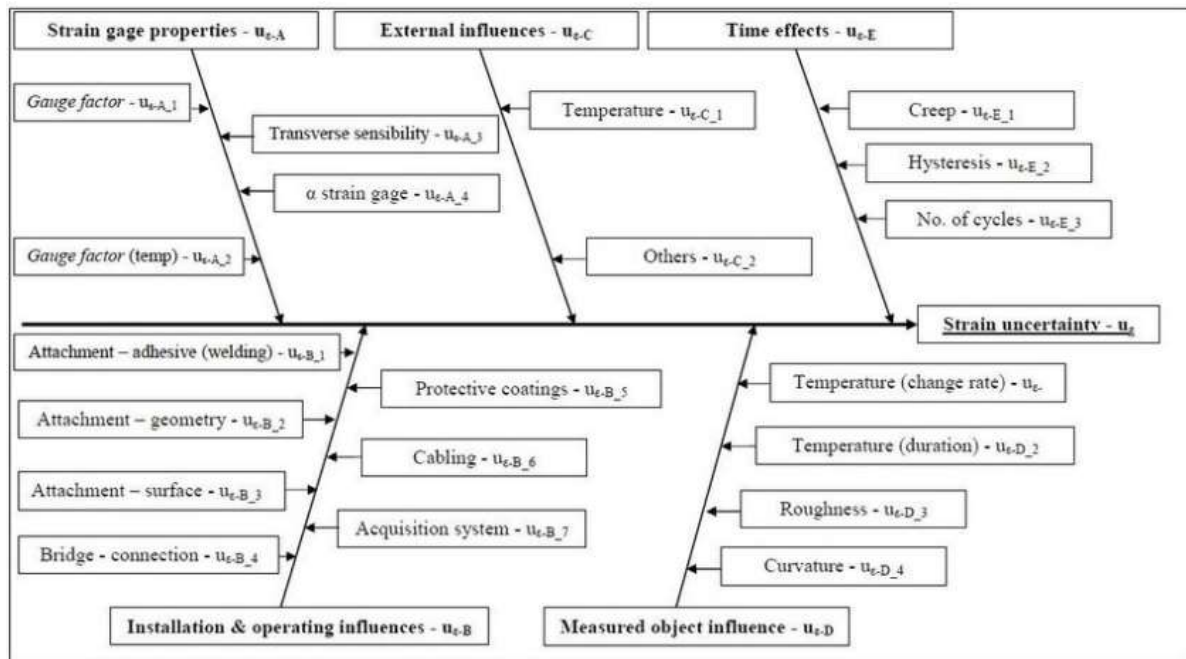


Figure 43. Uncertainty sources for strain measurements (Dokoupil, modified)

The strain was measured with a linear strain gauge, and therefore, the uncertainties are coming from two major sources. These sources are strain uncertainty and the uncertainty of elastic modulus of the measured object. According to Dokoupil, the error of elastic modulus, usually, oscillates between 3 and 15 (%) and cannot be under 3 (%) because of the principle of determination. Also, Dokoupil claims that the error of elastic modulus of common steel and alloy qualities exceeds the limit of 9 (%). He justifies the proposition by the good production techniques and wide knowledge of the materials. Because of linear measurement, most of the branches seen in the figure (43) can be neglected. Time effects were not counted in because the experimental test proceeded with a quasi-static speed (1 mm/s). Also, external influences were neglected because of the use of compensation gauge. All the other uncertainty sources were evaluated by using the following table (20) [58]. The table is following the previous figure ()

Table 20. Sources of strain measurement uncertainties

Uncertainty source	Error		Distribution	
A Strain gauge properties				
1	Gauge factor	δ_K		Uniform
2	Temperature	δ_{K100}	Strain gauge specific. (datasheet)	Uniform
3	Transverse sensitivity	δ_Q		Normal
4	Strain gauge (alpha value)	δ_α		Triangular
B Installation and operating influences				
1	Adhesive	δ_L	0.5-2.5 $\mu\text{m/m}$	Uniform
2	Welding		10-100 $\mu\text{m/m}$	
3	Geometry - attachment	δ_G	1-5 $\mu\text{m/m}$	Normal
4	Surface - attachment	δ_D	1-4 $\mu\text{m/m}$	Uniform
5	Connection (bridge)	δ_B		
6	Coating	δ_O	0-3 $\mu\text{m/m}$	Uniform
7	Cabling	δ_C	0-10 $\mu\text{m/m}$ (0-5 $\mu\text{V/V}$)	Normal
8	Acquisition	δ_{MJ}		Normal
C External Influences				
1	Temperature	δ_T	5-20 $\mu\text{m/m}$	Triangular
2	Others	δ_P	1-20 $\mu\text{m/m}$ (environment)	Uniform

D Measured object				
4	Temperature (rate of change)	δ_M	0-100 $\mu\text{m/m}$	Triangular
5	Temperature (effect duration)	δ_N		Uniform
6	Roughness	δ_R		Normal
7	Curvature	δ_Z		Normal
E Time effects				
1	Creep	δ_V	5-20 $\mu\text{m/m}$ (0.5 – 2 % of measured strain)	Uniform
2	Hysteresis	δ_H	5-20 $\mu\text{m/m}$ (0.25-0.5 % of measured strain)	Normal
3	Number of cycles	δ_U	10 $\mu\text{m/m}$	Uniform

To define the uncertainty of measured stress of uniaxial strain, it is necessary to define sensitivity coefficients C_ε (46) and C_E (47) which are based on Hooke's law [58].

$$C_\varepsilon = \frac{\partial(\varepsilon \cdot E)}{\partial\varepsilon} = E \quad (46)$$

$$C_E = \frac{\partial(\varepsilon \cdot E)}{\partial E} = \varepsilon \quad (47)$$

With the following equation (48) [57] one can define the uncertainty for the strain,

$$u_{\varepsilon} = u_{\varepsilon S} \cdot C_{\varepsilon} \quad (48)$$

where $u_{\varepsilon S}$ was the sum of pre-defined sub-uncertainties from the table (20). With the following equation (49) [58], one can calculate the uncertainty of the elastic properties of the measured material.

$$u_E = \frac{Z_{max}}{\chi} \cdot C_E \quad (49)$$

where χ represents the distribution and Z_{max} is the tolerance of modulus of elasticity of measured material. After this, a resultant of the two previous components (48 & 49) are calculated with the following equation (50) [58],

$$u_{\sigma} = \sqrt{u_{\varepsilon}^2 + u_E^2} \quad (50)$$

And the result is corrected with coverage factor c , which values can be seen from the following table (21)

$$U_{\sigma} = c \cdot u_{\sigma} \quad (51)$$

Table 21. Coverage factor values and corresponding probabilities.

Coverage factor value (<i>c</i>)	Probability
1	68.27 %
2	95.45 %
3	99.70 %

Complete calculations for one measured point can be found from appendices (Appendix 8).

4.3 3D-scanning of the specimens

Because measured specimens were organs, the deviation between characteristic dimensions was expected. Therefore, every measured sample was 3D-scanned to measure the surface curvature without applying any external loading to the specimen. The scanning tool has a resolution low enough to capture the curvature of a relatively small object with a reasonable error. According to the manufacturer the resolution of the 3D-scanner is 0.020 (mm) + 0.025 (mm/m). From the figure (44) below, we can see the actual measuring setup used for scanning. The scanned specimen is encircled in the figure with dashed lines.

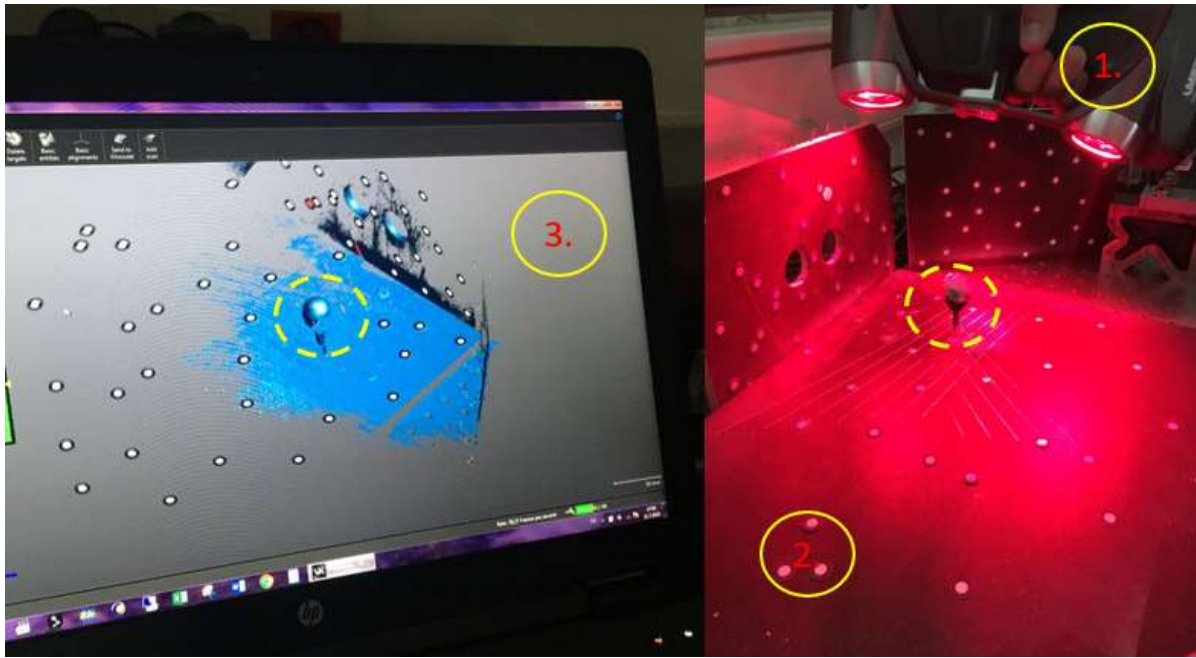


Figure 44. Setup for 3D-scanning.

From the table (22) below, we can see the used instruments and their specifications numbered in the figure (44).

Table 22. Instruments used in curvature measurement

Number	Model (description)
1.	HandySCAN 700 portable 3D-Scanner
2.	Positioning target stickers
3.	VXelements, a program for processing the mesh file

The specimen was scanned with HandySCAN700 portable 3D-scanner to estimate the specimen dimensions. Measurements were done with the program called SpaceClaim, where images were imported in stereolithography (.stl) format. After removing the unnecessary objects from the file, the partial eye model was sliced and measured by using three-point curve fitting. The sliced model can be seen from the figure (45).

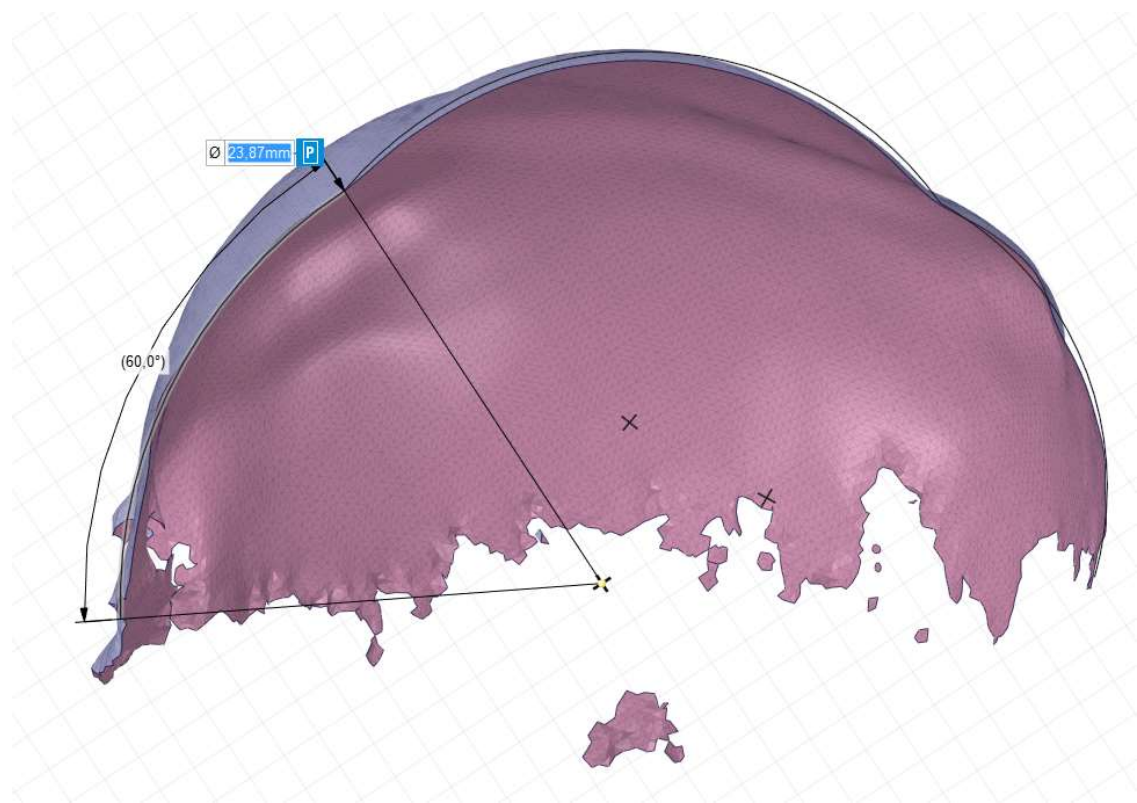


Figure 45. Sliced eye model in SpaceClaim -program.

4.4 Sclera thickness measurement

Because the thickness of the sclera is a variable of age and medical condition because the specimens were adopted from livestock, it means that the eyes were the substantially same age; hence, steady results were expected. The measurements were proceeded optically by measuring from the image. In the measurement setup, the recording camera was mounted to an aluminium profile with M6 hardware. The camera was pointed upwards to a transparent specimen holder made from plastic. The holder was fixed to Vertex magnetic dial gauge stage VMB-B with an M4 bolt and nut. Specimens were prepared to the measurement by cutting them half along the horizontal plane by hand. After preparations, the half-eye was inserted to the plastic holder cut edge towards the camera and against the plastic holder bottom. This was done carefully from preventing them not to fold or distort. For calibration, a control image

was taken from the millimetre paper, and by using that as a reference value. The thicknesses were measured from the cut surface with image processing tool. From the following figure (46), we can see the measurement setup for the sclera thickness measurements. From the following table (23), we can see the instruments used in the measurement.

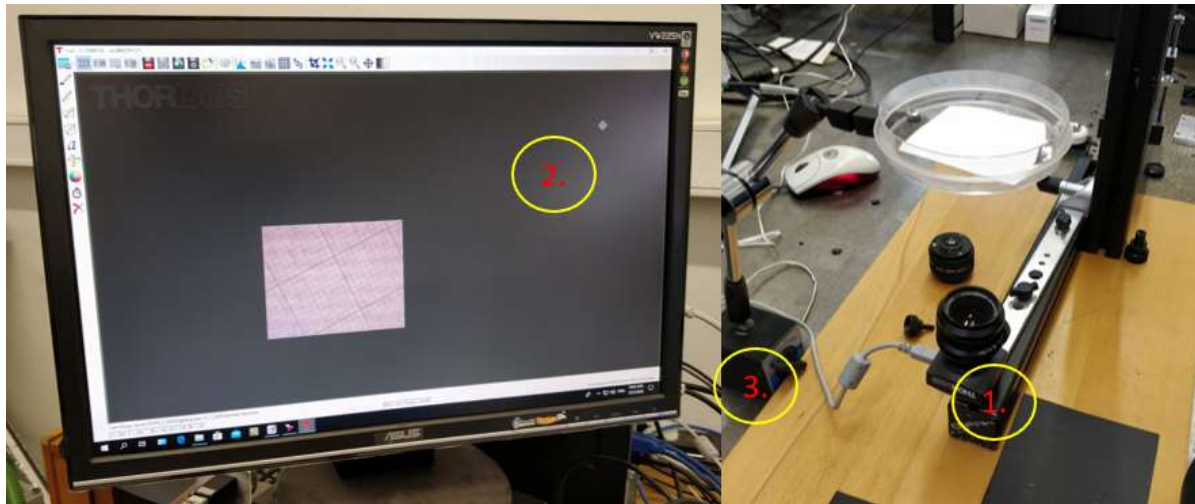


Figure 46. Sclera measurement setup

Table 23. Instruments used in the thickness measurements

Number	Model (description)
1.	ThorLabs DCC1645C-HQ, a camera with 1.4/25 optics
2.	ThorLabs program, for recording the image
3.	Vertex magnetic dial gauge stage VMB-B

5 RESULTS

5.1 Dimensions of sclera and cornea

Measured curvatures of ten specimens can be seen from the following table (24).

Table 24. Measured specimen curvatures.

Sample No.	Sclera curvature (mm)	Cornea curvature (mm)
1.	11.772	10.013
2.	12.678	10.302
3.	12.284	9.889
4.	11.540	9.728
5.	10.805	9.746
6.	11.444	9.422
7.	11.599	10.814
8.	11.239	9.412
9.	11.803	8.893
10.	12.619	10.072
Mean	11.778	9.829
SD	0.597	0.529

The geometry of the analysis model, originally based on the Gullstrand model, was updated to correspond measured values. The radii of curvature for sclera was 11.778 ± 0.597 (mm) and for the cornea is was 9.829 ± 0.529 (mm). According to the measurements, the thickness of the sclera was 0.54 ± 0.12 (mm). According to Olsen et al., the porcine scleral thickness is very similar to human sclera thickness [59]. The thickness of sclera varies across the eye. Olsen et al. discovered that the thickness depends on the physical size of the porcine. They discovered in their paper that the thinnest area is located approximately 5-6 (mm) from the limbus area where the cornea connects to the sclera [59]. According to their measurements, the mean thickness near the equator is 0.56 ± 0.11 (mm), which supports our findings.

5.2 Probe curvatures

The probe curvatures were measured from the recorded videos. A screen captures were taken from the video at the times when the movement sequence reached its extremities, and therefore the probe reaches its maximum deformation. From the still images, the radii of curvatures were evaluated by using three-point fitting in ImageJ, and the results were compared to the FE analysis results. Example fitting can be seen from the figure (47). Results can be seen from the following table (25).

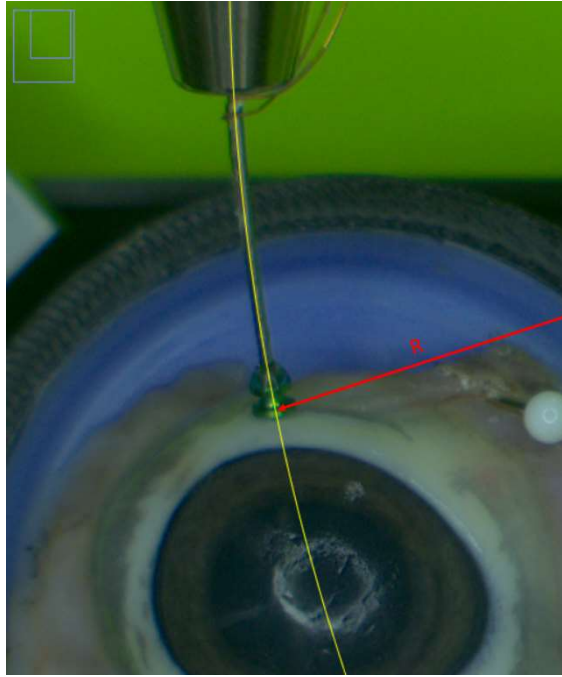


Figure 47. Three-point curve fitting in ImageJ

Table 25. Measured probe curvatures

23G Needle	Radius [pixels]	Radius [mm]	Pixels / mm
Mean	4031.5	179.7	22.43022
SD	2118.9	94.5	
Min	2158	96.2	
Max	10945	488.0	
Phynox tube	Radius [pixels]	Radius [mm]	Pixels / mm
Mean	2762.1	123.1	22.43022
SD	799.5	35.6	
Min	1726.0	76.9	
Max	4110.0	183.2	

While measuring some of the specimens had more freedom to move in the holder than others. Therefore, the results came with such a high standard deviation. Otherwise, the measured values are in line with the analytical theory of a cantilever beam with a point load. Complete calculations can be found in appendices (Appendix 9).

The FEA results were measured from the deformed endoscope probes. This was done by slicing the deformed geometry along the probe axis and then use three-point curve fitting to realise the probe model curvature. The sliced results, fitted on top of each other, can be seen from the following figure (48).

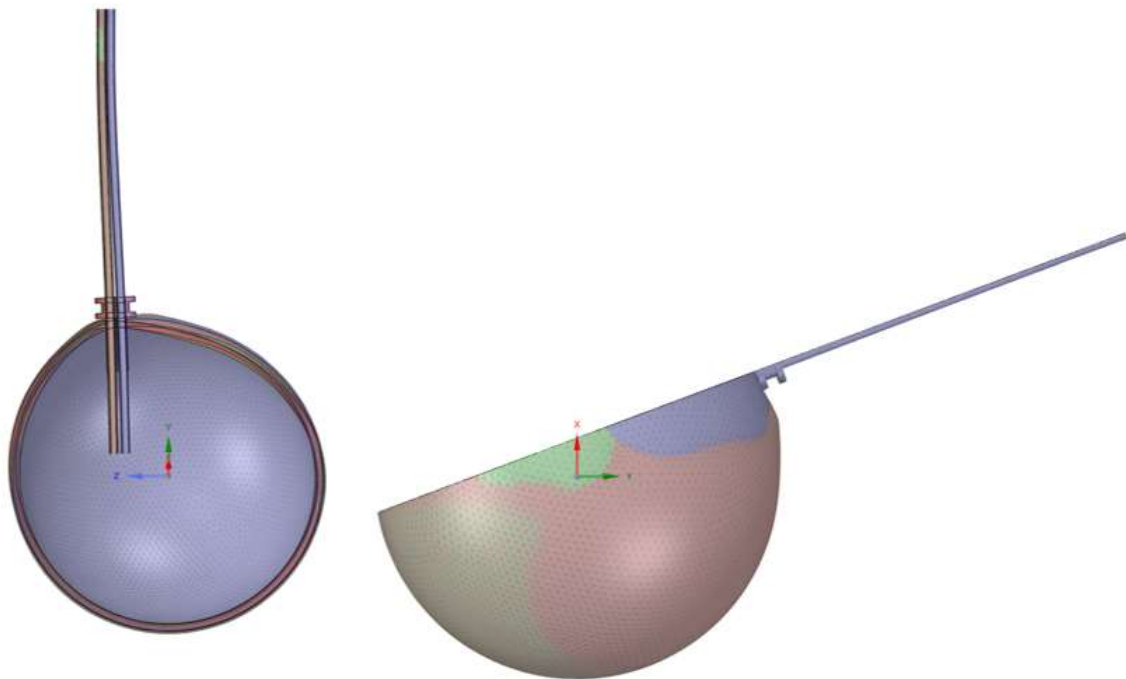


Figure 48. Sliced deformed models.

The fitting was done by using the common axis for each result. These axes were defined to the top part of the probe because the deformation curve is not uniform all across the probe. The non-uniformity is caused by contact formulation between the terminal and probe wall. This contact formulation closes the gap between those two bodies and therefore, stiffens the contact behaviour and makes it easier to converge. On the contrary, the contact type creates a

support which has a contact area instead of point-like support, which would allow the probe to bend more uniformly. With this procedure, local stress hotspots were evaded, and convergence was made significantly easier. The curvature evaluation can be seen from the following figure (49). The common axes are highlighted in the figure with red dashed lines.

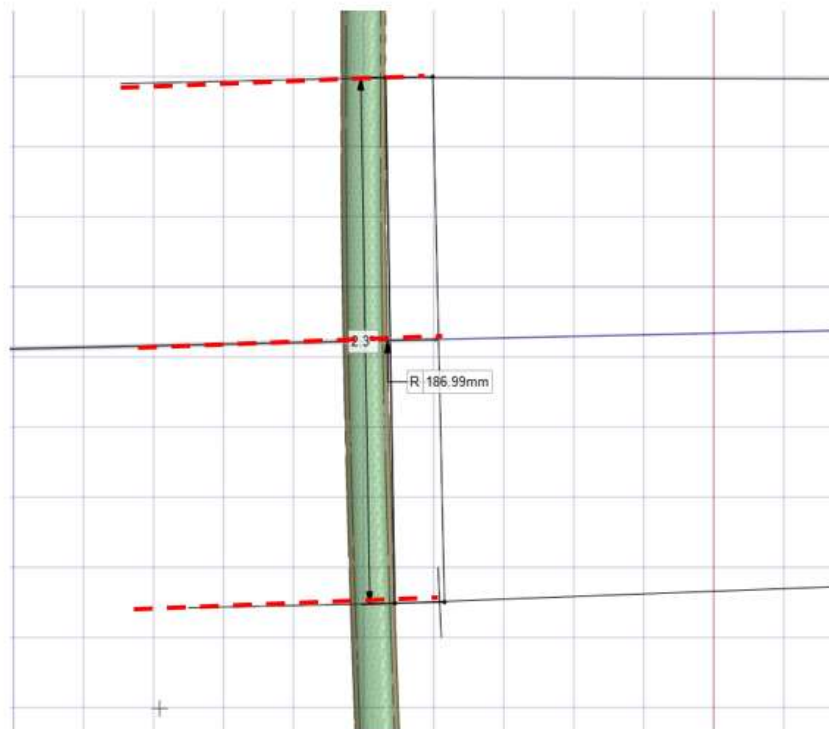


Figure 49. Probe curvature evaluation

The results from the FEA can be seen from the following table (26).

Table 26. Probe deformation results.

	nH	MR calculated	MR fitted
Radius [mm]	191.58	185.82	153.38

5.3 Port dislocation under loading

Port dislocation was measured from the recorded videos by taking a still image on the initial state of the eye before testing and when the needle had reached its extremity (5 mm dislocation). By comparing distances between the port to the holder wall, before and after needle dislocation, one was able to calculate the absolute displacement of the port. The measurement process can be seen from the following figure (50).

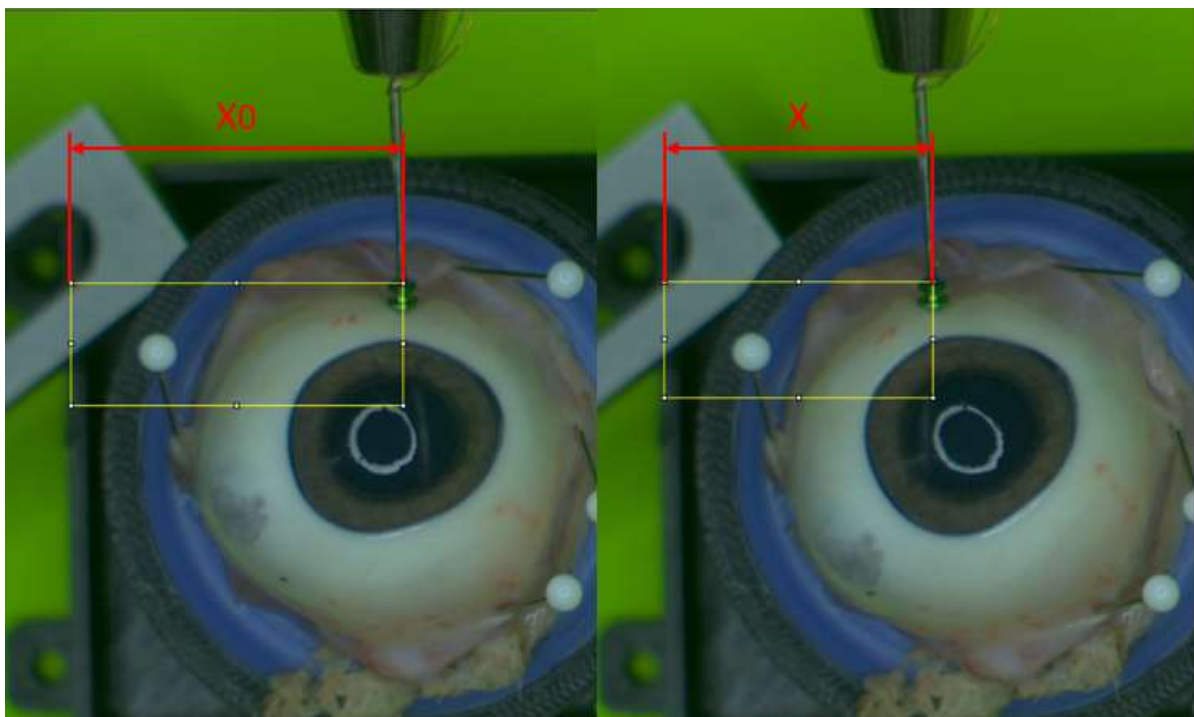


Figure 50. Port dislocation measurement from still image

Results of the measurement can be seen from the following table (27). Complete measurement can be found in appendices (Appendix 10).

Table 27. Port dislocation, measured and FEA

Needle Position [mm]	0	5	Δ
Mean	24.4	20.4	4.0
SD	0.514	0.443	0.496
Min	23.9	19.7	3.39
Max	25.3	21.1	5.08
FEA	Directional Deformation global Z+		
Material Model	MR fitted	MR calculated	nH
Dislocation [mm]	4.1433	4.3929	4.3789

From the results can be seen that the model with fitted MR material model was most stiff and therefore, represented best the actual test situation.

5.4 Reaction forces

The reaction forces are telling the force input to the system. In this case, it is the simplest way to measure the quality of the model. The input is needle dislocation, and output is the reaction force. From the experimental test, the reaction force was defined through the deflection of the probe. The deflection was measured from the still images taken from the recorded video on the time when the needle reaches the dead point of the dislocation. Measurements are illustrated to the following figure (51).

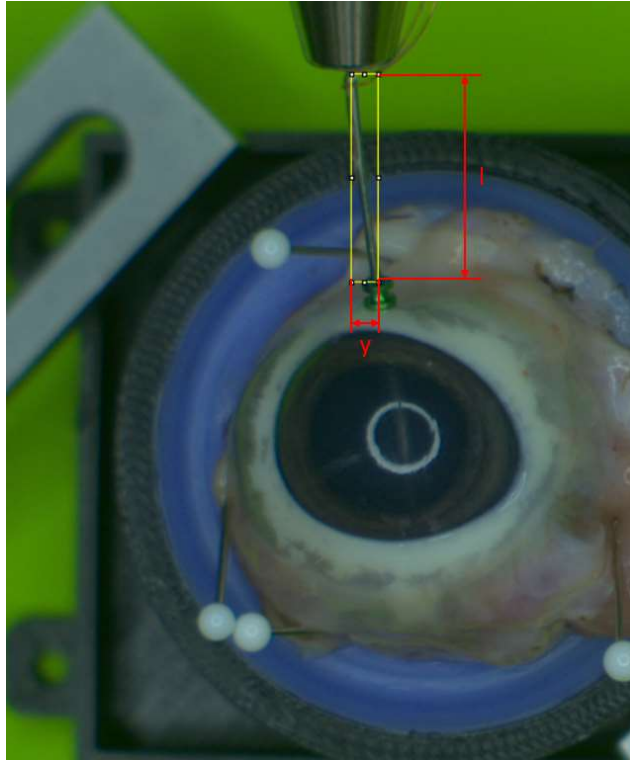


Figure 51. Probe deflection measurement.

Because the needle was located in angle, the measured length (l in the figure) needs to be corrected. This was done by using the cosine of the measured probe angle. The angle was measured from the recorded video. Measuring procedure is illustrated in the following figure (52).

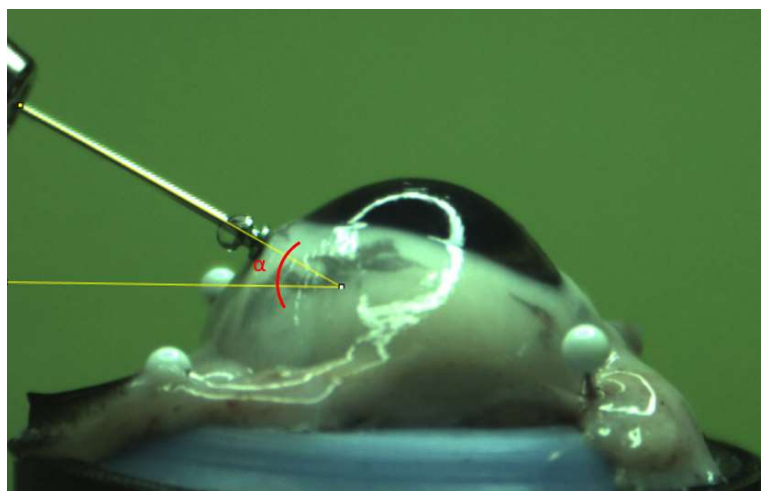


Figure 52. Probe angle measurement

The results of angle measurements can be seen from the following table (28).

Table 28. Probe angle results

	Mean	SD	Min	Max
Angle [°]	23.1	2.0	19.3	28.3

After the deflection length was corrected with the angle of the probe, total deflection could be calculated. This was done by using the following equation (52) [20].

$$y(\text{max}) = \frac{F \cdot l^3}{3 \cdot E \cdot I_z} \quad (52)$$

If we solve the equation (52) for the force F we obtain the following form,

$$F = \frac{3 \cdot E \cdot I_z \cdot y(\text{max})}{l^3}. \quad (53)$$

In the equation I_z represents the second moment of area, $y(\text{max})$ is maximum measured deflection and l is deflection length. By using equation (53), the maximum reaction force was calculated. Summary of the measured values can be seen from the following table (29).

Table 29. Measured deflection and length values.

	Mean	SD	Min	Max
$y(\max)_{Needle}$ [mm]	1.56	0.613	0.490	2.85
$y(\max)_{Phynox}$ [mm]	1.61	0.62	0.85	2.76
l [mm]	15.5	0.70	14.0	16.7
Corrected l [mm]	16.9	0.767	15.2	18.1

To be able to define reaction force from the maximum deflection, one must know the second moment of area of the used geometry. This was calculated by the following equation (54) [20].

$$I_z = \frac{\pi \cdot (D^4 - d^4)}{64} \quad (54)$$

In the equation, D is outer diameters of the probe, and d is the inner diameter of the probe. All the values used for the reaction force calculations are gathered in the following table (30). The values for the elastic modulus and the complete calculations can be found from the appendices (Appendix 11).

Table 30. Geometric and elastic values of the tested probes

	Needle	Phynox tube
E [MPa]	193000	203400
I_z [mm ⁴]	0.007675	0.004913
D [mm]	0.6414	0.635
d [mm]	0.337	0.5

All the calculated reaction forces and FEA results are gathered in the following table (31). The reaction forces from the FE analysis were plotted from the joint constrain of the silicone holder. The joint restraint can be seen from the figure (34) in the chapter (3.7).

Table 31. Reaction forces

	F_{Needle} [N]		F_{Phynox} [N]
Measured	1.44		1.10
Model	MR fitted [N]	MR calculated [N]	nH [N]
FEA	1.9549	1.211	1.2012

As one can see from the results, the measured values are placed somewhere between the MR material models. Fitted MR model was stiffest and model, which was calculated by using the linear elastic values corresponded best to the experimental results. In the analysis, there is plenty of factors which are affecting the reaction force. Material stiffness is one, and the rest of them comes from various sources, like contacts and boundary conditions. In many cases defining these factors are a compromise of accurate modelling and simplifications. Simplifications are a necessary evil when it comes to modelling. In many cases, they are necessary for the convergence and for the cost of the calculations in a matter of CPU time.

In this case, the difference between the FE results was caused by the differences between the material models, since all the models were executed with identical element mesh, boundary conditions and contacts.

5.5 Strain gauge measurement

The induced stress was measured with a Kyowa KFGS 1N-120-C1-11 strain gauge. The gauge was glued to the needle, which was replacing the endoscope probe in the experiment. The gauge was connected to HMB Scout 55 mobile amplifier in a quarter bridge with a temperature reference gauge. The temperature reference was placed right next to the needle holder where the atmospheric temperature is as close as possible to the temperature of measuring event.

The data was logged with LabView, and the total uncertainty of the measurement event was evaluated with the method of GUF, presented in the chapter (4.2.1) in details. Measured strain values can be seen from the following figure (53) where the measured strains are plotted to the respect of time. The measuring frequency was 100 (Hz); hence, every measurement contains 1000 data points. The total measured time was 10 (s)

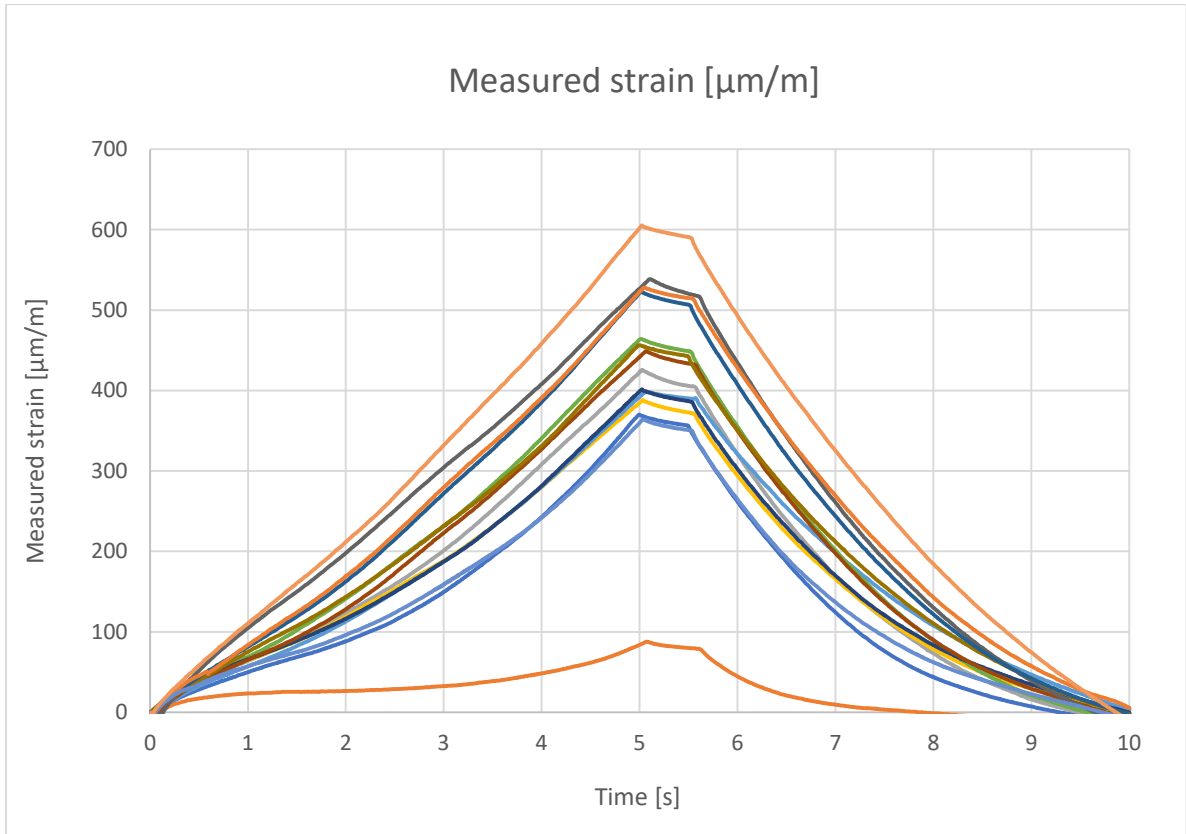


Figure 53. Measured strains from 14 samples

From the following figure (54), we can see the measured stresses plotted to the respect of time. In the figure is calculated the measurement uncertainty for every data point. The uncertainties are presented with the dashed lines in the figure. The values of the stress are averaged from all the logged measurements done in the experiment.

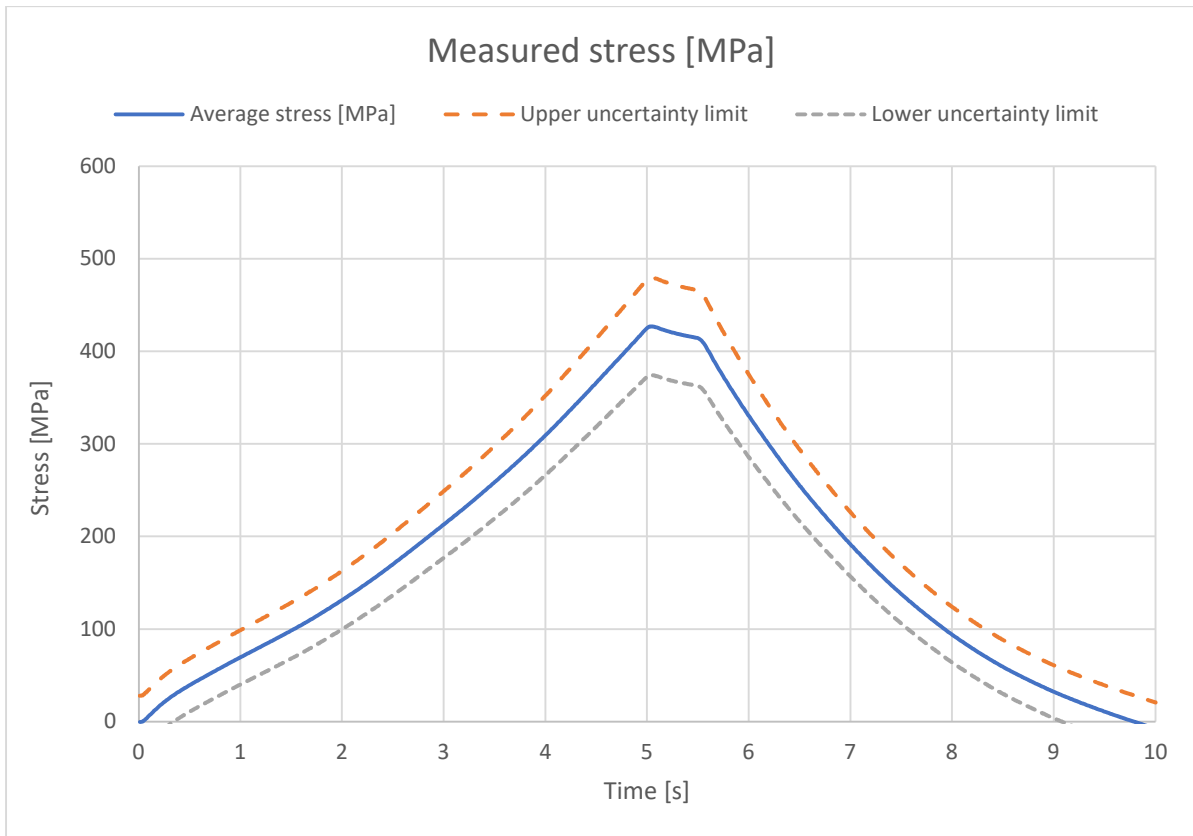


Figure 54. Measured stresses with measuring uncertainties.

The exact placement of the strain gauge was approximated from the recorded videos. The manufacturer gives the external size of the measuring area of the gauge; hence, the location of the stress plot was defined by these two boundaries. Illustration of the gauge place measurement can be seen from the following figure (55).

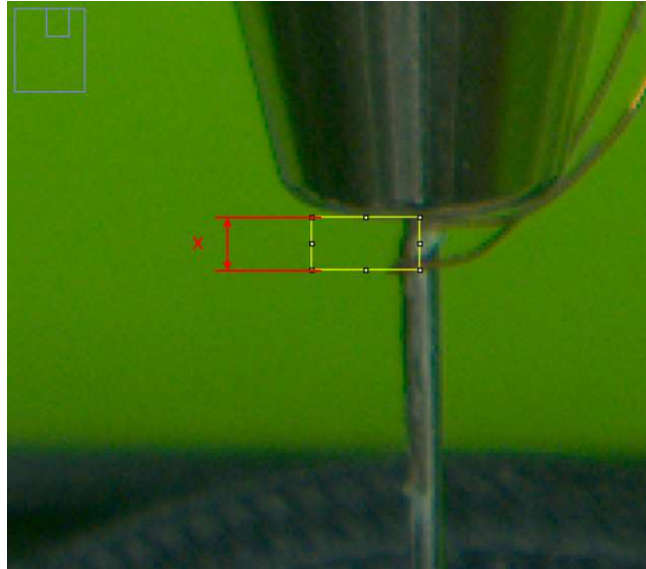


Figure 55. Approximating the position of the strain gauge $x = 0.9 \pm 0.1$ (mm)

From the following figure (56), we can see the von-Mises stresses plotted across the Phynox tube body. In these results, the material model was nH.

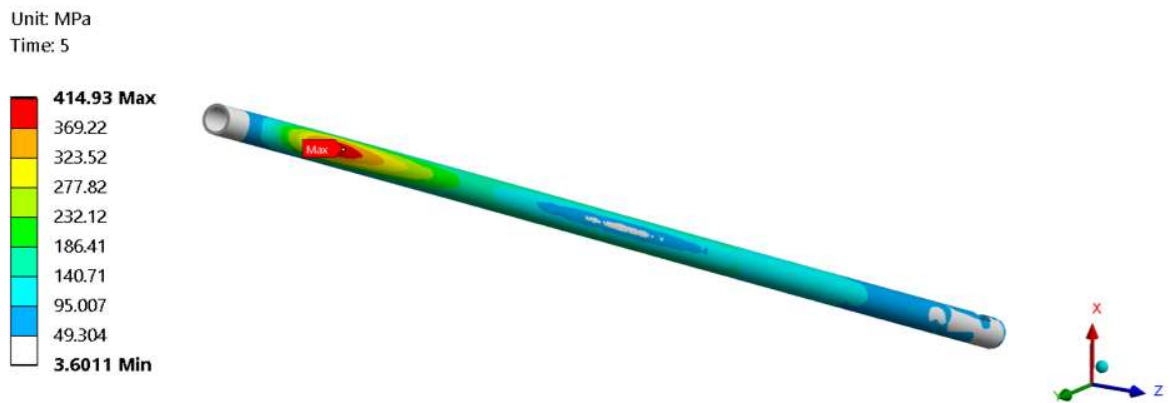


Figure 56. von-Mises stress in Phynox tube, nH (414.93 MPa)

Form the previous plot; we can see that the maximum stress occurs on the area of boundary condition, where the probe is connected to the holder. Since the remote displacement is deformable, the local stress area continues to the inside of the holder. Therefore, no singular

line was created in the plot. From the following figure (57), we can see the stress plotted across the GRIN -lens surface.

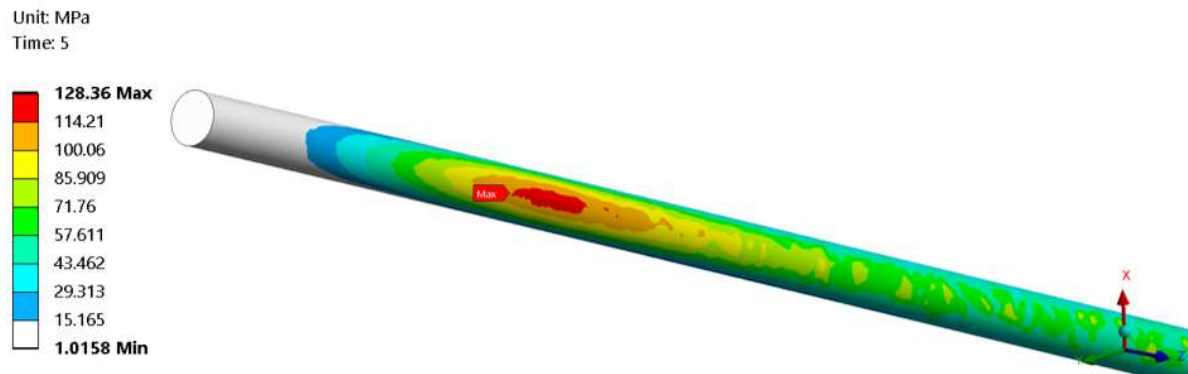


Figure 57. von-Mises stress in GRIN -lens surface, nH (128.36 MPa).

From the previous plot, we can see that the maximum stress occurs at the boundary condition area. The stress is distributed similarly as it does in the previous figure (57). From the next figure (58), we can see the illustration of the area where the strains were measured during the experiment. From the following figure (59), we can see the von-Mises stress plotted across the surface of the Phynox tube on the area where the strain gauge was located during the experiment.

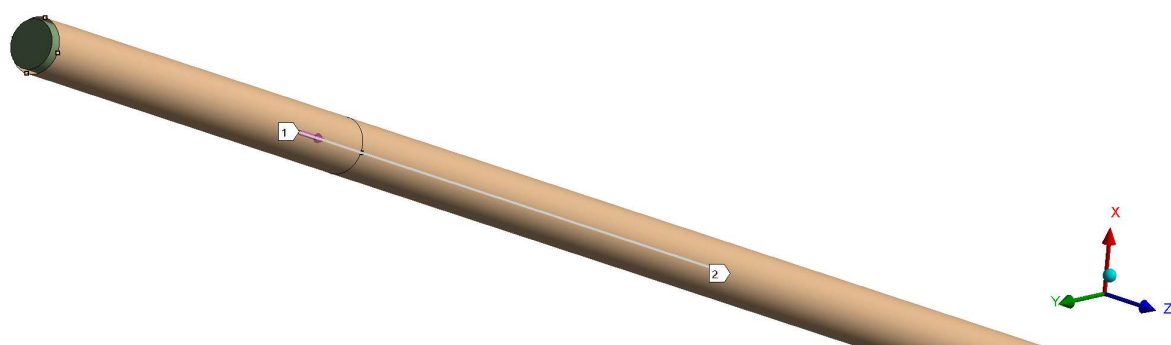


Figure 58. Stress plot area on the level of the probe neutral axis. Plotting direction from 1 to 2.

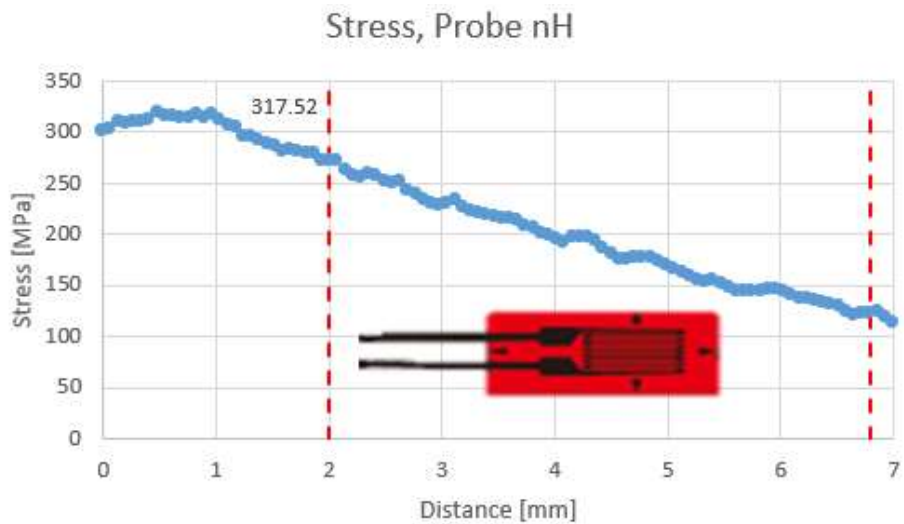


Figure 59. von-Mises stresses plotted along the path (317.52 MPa).

From the previous figure (59) we can see that the plotted area was, intendedly, extended over the strain gauge limits, because the location was just estimated from the videos and may contain some error. The approximated location of the strain gauge is allocated in the previous figure (59) with red dashed lines. The distance is measured from the (previous figure 58) point one to point two. The differences between the results plotted over the body, and path-oriented one can be explained with the asymmetric behaviour of the model. The plot path is colinear with the probe axis and located on the place where the maximum stress should occur in the case of bending. Comparing the body results to the path results quickly reveals that the stress peak is not on the level of the neutral axis. This is proved in the following figure ().

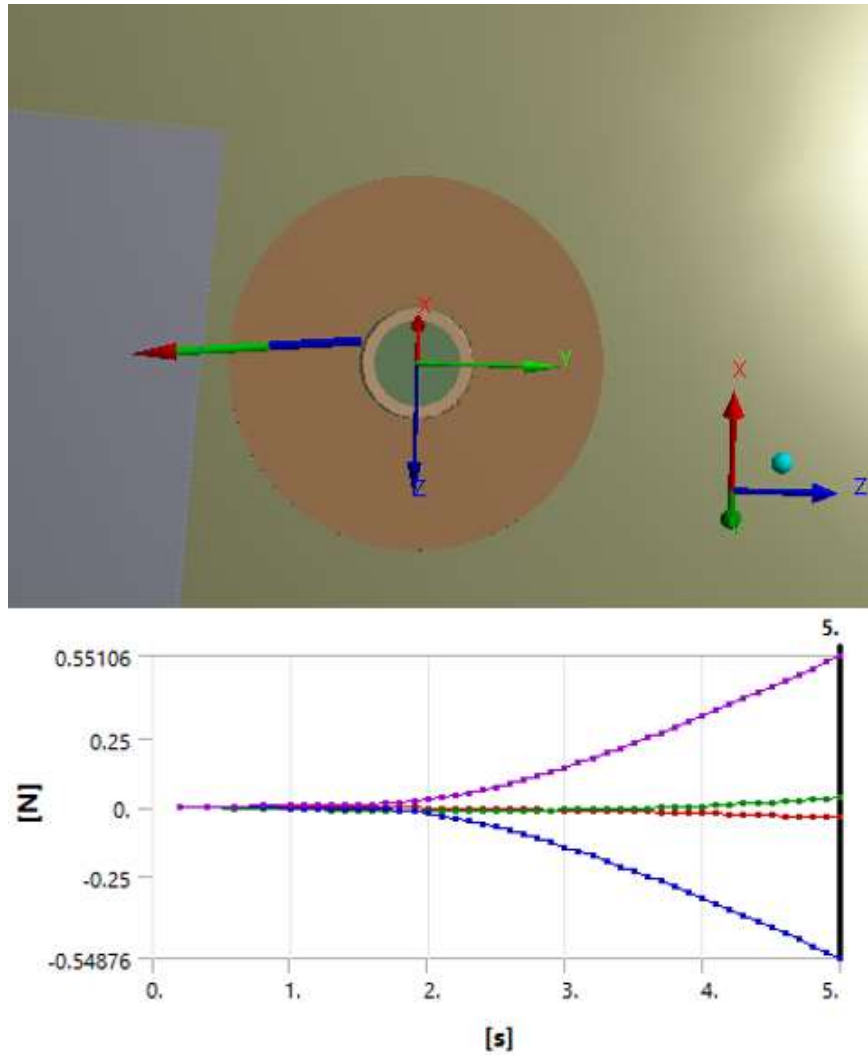


Figure 60. Terminal and probe contact reaction force resultant vector.

From the previous figure (60), we can see that the force reaction resultant is offset when compared to the local (y) coordinate, which represents the direction of the remote displacement boundary condition. The displacement was executed with a constant speed of 1 (mm/s) for a total loading time of five seconds. From figure (60), we can see that the offset between the neutral axis of the probe and the resultant vector is roughly 25 (%) from the total diameter of the endoscope probe. The different colours in the force plot are representing different components of the force vector. From the next figure (61), we can see the von-Mises stress plot across the Phynox tube body. In these results, the material model was calculated MR.

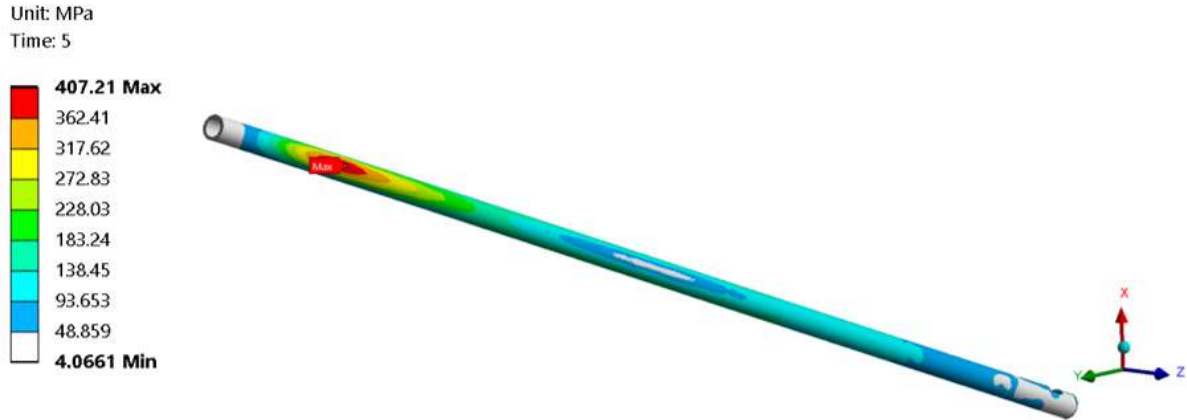


Figure 61. von-Mises stress in Phynox tube, MR.c (407.21 MPa)

From the previous figure (61), we can see that the local peak stress area is plotted on the area of the boundary condition. From the following figure (62), we can see the stress plotted across the GRIN -lens surface.



Figure 62. von-Mises stress in GRIN -lens surface, MR.c (125.19 MPa).

From the previous figure (62), we can see that the maximum stress occurs at the boundary condition area. The stress is distributed similarly as it does in the previous figure (61). From the following figure (63), we can see the von-Mises stress plotted across the surface of the Phynox tube on the area where the strain gauge was located during the experiment.

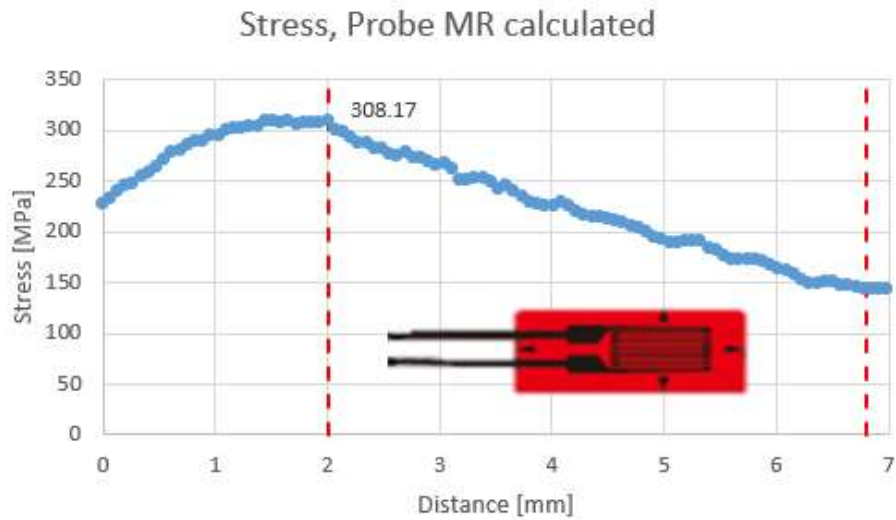


Figure 63. von-Mises stresses plotted along the path (308.17 MPa).

The approximated location of the strain gauge is allocated in the previous figure (63) with red dashed lines. Again, when comparing the path-oriented results to the body stress, we can see the difference between them. From the next figure (64), we can see the von-Mises stress plot across the Phynox tube body. In these results, the material model was fitted MR.

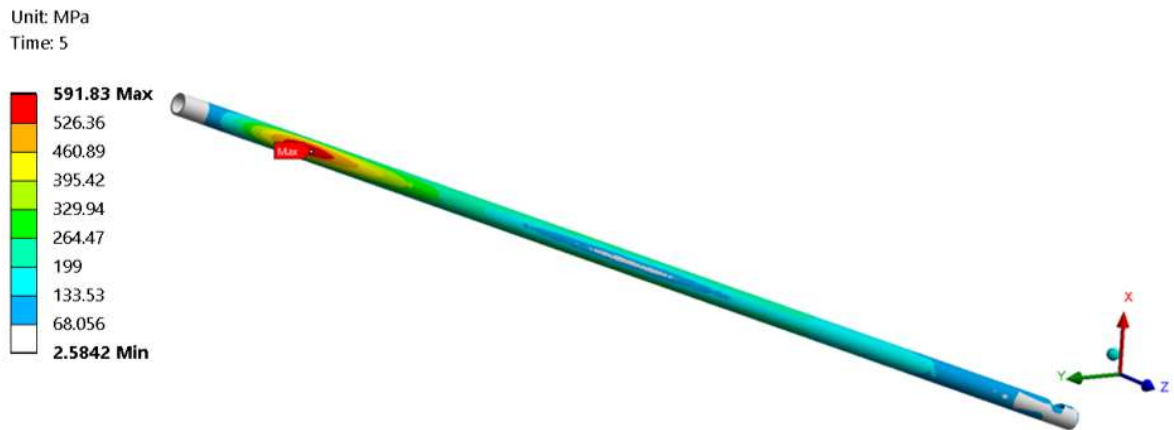


Figure 64. von-Mises stress in Phynox tube, MR.f (591.83 MPa)

From the previous figure (64), we can see that the local peak stress area is plotted on the area of the boundary condition. Because the material model is stiffer than the two previous ones,

the induced stress is also bigger, because of the force reaction. From the following figure (65), we can see the stress plotted across the GRIN -lens surface.

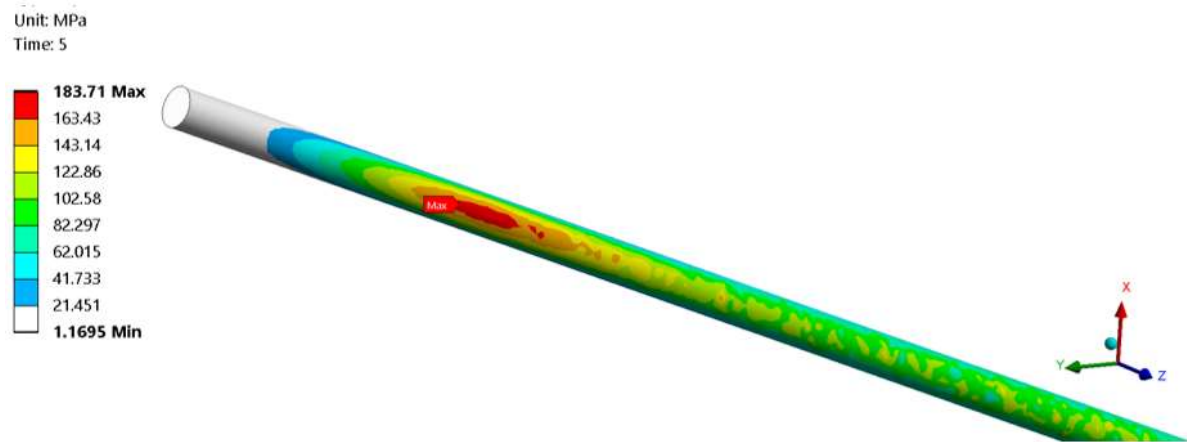


Figure 65. von-Mises stress in GRIN -lens surface, MR.f (183.71 MPa).

From the previous figure (65), we can see that the maximum stress occurs at the boundary condition area. The stress is distributed similarly as it does in the previous figure (64). Because the fitted MR material model is stiffer than the two previous ones, the induced stress levels are way higher than on analyses which used material values from the literature. According to Hošek et al. results, the experimental stress limit under bending load for GRIN lens is $171.1^{+4.2}_{-4.6}$ (MPa) [42]. Therefore, it is safe to assume that the lens would not carry such big local stress without being damaged permanently. From the following figure (66), we can see the von-Mises stress plotted across the surface of the Phynox tube on the area where the strain gauge was located during the experiment.

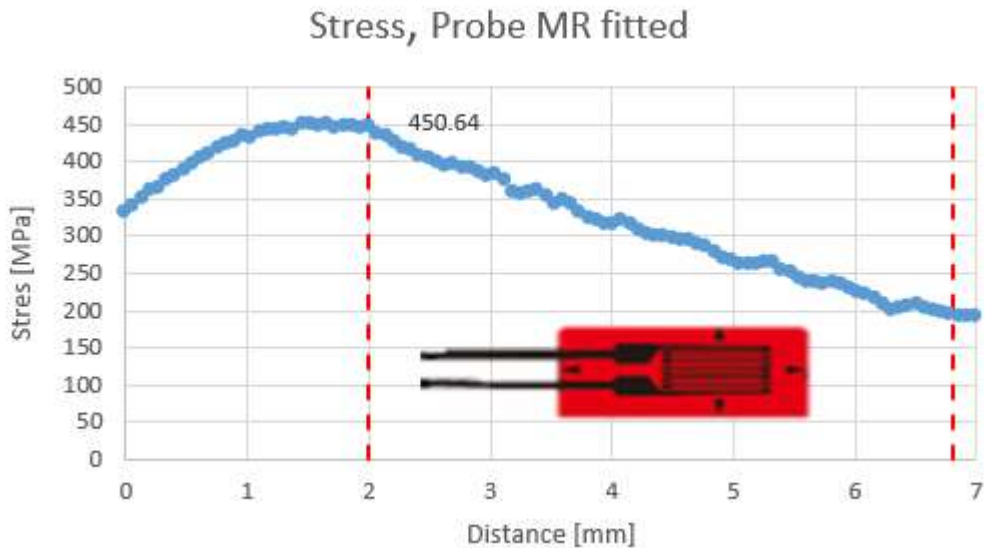


Figure 66. von-Mises stresses plotted along the path (450.64 MPa).

The approximated location of strain gauge is allocated in the previous figure (66) with red dashed lines. From limited area results, we can see that the stress plot of the MR fitted model is most close to the measured one. Although, the strain gauge was, according to the manufacturer, designed for regular steel and not for stainless steel and it was installed over a surface which has a significantly smaller radius than the manufacturer recommends. Also, the strain gauge might be not installed straight along with the needle axis. All these points were tried to take under consideration in the measurement uncertainty calculations by using the biggest possible multiplication factor for the measured object influences.

From the following table (32) is gathered all the numerical results from the stress analysis and the strain measurements.

Table 32. Stress results

	Strain gauge	Probe body	GRIN lens	Uncertainty (95.45 %)
Model	[MPa]	[MPa]	[MPa]	[MPa]
Experimental	427	-	-	±52.7
nH	317.52	414.93	128.36	-
MR calculated	308.17	407.21	125.19	-
MR fitted	450.64	591.83	183.71	-

Because of the big measurement error, we can only consider the experimental value as a directional, which gives the magnitude for the maximum stress occurring in the probe.

Coefficients for the neo-Hookean material model was gathered from the literature [46] [49] [50] [51]. Mooney-Rivlin (calculated) was constructed by derivating the coefficients from linear elastic material properties by using small strains assumption. Mooney-Rivlin (fitted) model was constructed by using uniaxial stress-strain measurement data from the literature [52] [49]. Used coefficients can be found from the tables (13 & 14). All the material properties can be found from appendices (Appendix 4, Appendix 5 and Appendix 6).

6 CONCLUSIONS

This research aimed to identify the critical parts of the endoscope under working load by studying the stresses and displacements in the human eye and in the instrument. This research goal was achieved by the help of numerical simulation methods, verified by a set of experimental measurements. In the numerical simulations, hyperelastic material models were applied to achieve a response matching the experimental results. Two different constitutive material theories were applied to the numerical analysis, neo-Hookean and Mooney-Rivlin. From these two, the Mooney-Rivlin was constructed in two different ways. First one was to find the coefficients by using small strain assumption and the second way was to find the coefficients by using material test data from the literature.

The data gathered from the experimental measurements were used to update the model to match it with the measured samples. All the values, affecting the geometry, was taken as an average of ten to fifteen samples. For some measurements, it was possible to use even bigger sampling, like with the outer curvature or thickness measurements. In those cases, the sample was measured from multiple points, and the results were averaged after that. The FE model was compared to the measured values of four different quantities. First was the probe curvature under loading, the second was the dislocation of the terminal, third was reaction forces, and last was stress on the probe. By using those values, it was possible to find the best matching model and use that to determine the actual stress affecting the GRIN lens inside of the phynox tube.

All of this started from finding an appropriate material model to describe the behaviour of soft tissue. This was a fairly complicated task since most of the material models are developed on industrial purposes, and the rest remaining requires some seminal material testing and requires a vast amount of computational capacity. Researchers have successfully applied some hyperelastic material models, originally developed for rubber, to model organic soft tissues like in the Ayyalasomayajula et al. study shows [23]. Some of those models are working good in some limited boundaries; hence, are capable of catching the high deformations what occurs in these types of materials. It is good to realise that the hyperelastic models do not carry any physical information about the material itself, unlike linear-elastic or plastic-elastic models which are based on the elastic properties of the material. Since the neo-

Hookean model is fairly common when estimating the hyperelastic behaviour, there was plenty of sources for the coefficients in the literature. Although this model is fairly simple and stable in any conditions, it can describe relative strains only till 100 (%) and will not account strain stiffening behaviour. Therefore, Mooney-Rivlin two-term and three-term models were used to compare the results and see which one manages to match the experimental results. By the rule of thumb, every degree in the material model needs a separate material test; otherwise, the model might turn to unstable under multiaxial loading. The material model instability occurs in the analysis as convergence problems due to the highly distorted mesh elements or non-physical stress-strain behaviour. For setting up the neo-Hookean model, literature values were used. For the second model, two-term Mooney-Rivlin both coefficients were derived from the elastic literature values analytically with a small strain assumption. For the third model, uniaxial tension test data from literature was used to make the fitting.

In this thesis material model played a significant role since it was the only variable between different models. By using the results of this work, it can be concluded that even a small change in the material model can make a great difference in the results and therefore, should be considered carefully when simulating soft tissues behaviour. In many cases, the non-linear simulations suffer convergence problems of various sort. Contacts are usually the main cause of these convergence issues. The contact stiffness is considered as the most important value in contact modelling. If the contact stiffness is too high, it causes the elements to bounce off from each other between the iterations. This phenomenon causes oscillation in the model and eventually causes instability. Too low contact stiffness allows the contact elements to penetrate, and this causes convergence issues too. In many cases, the optimal stiffness coefficient is found by trial and error method. On modern FEA programs, the initial contact stiffness is set automatically with the help of contact formulation, but the initial guess is only general and does not apply in analyses with multiple non-linear factors. In this research, the contacts played a vital role in stabilising the sclera behaviour. On the early versions, the sclera tissue tended to locally buckle around the terminal when loaded. The problem was fixed by adding more stiffness to the contact elements between the probe surface and the terminal. Together with the frictional contact, it stabilised the area, and on the later models, the buckling was not a problem even under higher loading.

The initial assumption was that the endoscope probe, a glass-steel composite, might be the most critical part in the endoscope. According to Hošek et al., the maximum bending

radius of GRIN lens is 97 ± 6 (mm) and therefore the probe should not be bent in any smaller radius than 105 (mm) [42]. If the results from the curvature fittings and FE analyses are compared, it can be seen that the model which uses MR material with analytically estimated coefficients provided the best matching results 185.82 (mm) curvature of the radius. In the experiment, we measured the value of 179.7 (mm) as a radius of the curvature for the 23G needle. However, the measurements were done with standard 23G needle, and the analysis was proceeded with the geometry of the real endoscope probe, which is a composite. Also, in the FE analysis, a bonded contact was used between the lens and the tube body. This method is artificially stiffening the probe and therefore providing optimistic results. If the second moment of area of the endoscope probe and 23G needle are compared, we obtain a difference of 4.0 (%) (Appendix 9) between the values. The second moment of area value for the endoscope probe assumes that the lens is also calculated in the area and therefore, corresponds to the FE analysis approach. Hence, one can conclude that the analytically defined MR model corresponds with the measured values of the needle deflection.

When comparing the dislocation of the terminal between the experimental and numerical results, we obtain much bigger differences than in curvature measurements. This is mainly caused by the inaccurate material model since the stiffness of the other bodies are almost neglectable and can be contrasted as rigid bodies. From these values, the best matching numerical results come from the MR, which was fitted in Wollensak et al. [52] and Uchio et al. [49] uniaxial test results. This confirms the assumption of complex material behaviour.

As seen between the dislocation comparison, the same scattering of the results is seen in the case of force reactions. This is also highly depending on the material model of the eye tissue. The overall stiffness of the material defines the rate of how much the applied boundary condition is absorbing the deformation of the eye tissue and how much it resists the deformation. According to the numerical results, the MR with calculated coefficients corresponded best to the experimental values with a 19 (%) difference.

If the force reaction is looked, one can clearly see that there is a huge gap between the analytically derived coefficient models and data fitted model. This is due to the small strain assumption done in the analytically derived MR model. The model cannot simply describe the strains accurately enough. An example can be seen from the following figure (67) [60].

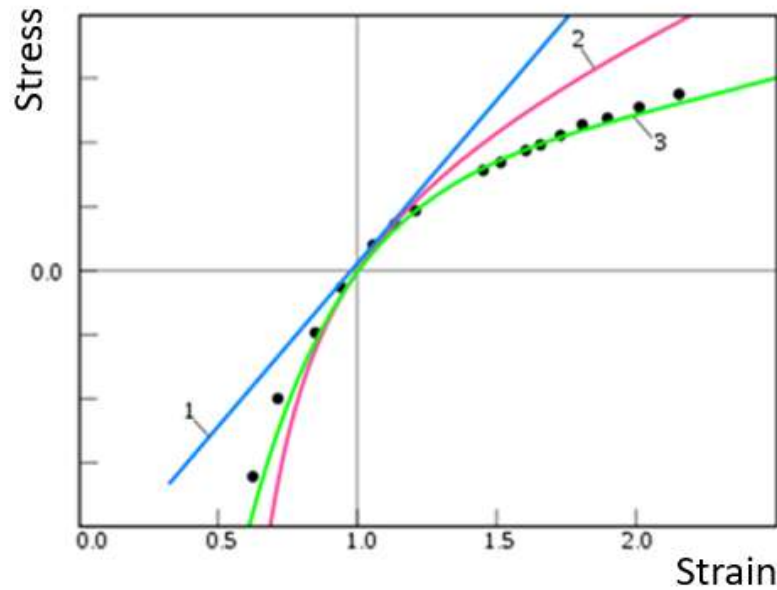


Figure 67. Stress-strain behaviour between linear elastic model and Mooney-Rivlin solids (Wikipedia, modified).

From the previous figure (67), we can see Hookean linear elastic material (1), neo-Hookean model (2) and Mooney-Rivlin model (3). Because of the small strain assumption in the analytically derived MR model, the stress-strain curve closes to the neo-Hookean curve, and therefore, it is not capable of describing the material hyperelasticity. This effect can be seen in the force reactions since the model is too stiff. This provides a significantly bigger reaction force because there is not so much deformation in the eye body than there should be.

While the data fitted model gave maximum von-Mises stress value of 591.83 (MPa) on the outer surface of the phynox tube the nH model and MR with analytically defined coefficients gave peak stress corresponding only $2/3$ of the biggest value. The measured peak stress was 427 ± 52.7 (MPa). The uncertainty was evaluated with the method of GUF, presented in the chapter (4.2.1). The estimated uncertainty is so big because the strain gauge type was for common steel while the measured material was stainless steel. Also, the gauge was glued on the surface, which falls below the manufacturer recommendations of minimum radius of 3 (mm). For this measurement, both analytically defined models provided reasonable peak stresses plotted across the body of the probe when compared to the measured values.

The similar behaviour between nH and estimated MR models can be explained due to the reduction of the strain energy density function. From the following equation (55) [24] we

can see that when the two-term MR model first coefficient (C_{10}) goes to zero it cancels out the second strain invariant.

$$W = C_{10} \cdot (I_2 - 3) \cdot C_{01} \cdot (I_1 - 3) + D_1 \cdot \left(\frac{V}{V_0} - 1\right)^2 \quad (55)$$

Thereby, we obtain a neo-Hookean solid. The differences between the data fitted analysis model, and nH model was the material in the sclera, which also accommodated a small value first term. From where we can conclude that soft tissue simulations are extremely sensitive to the quality of the used material model. Although, in some cases, the analytically constructed model provided matching results when compared to the experimentally measured values. This perception supports the guideline given for different hyperelastic materials on their capacity to model relative strains.

7 RECOMMENDATIONS

Based on the conclusions, future researchers should consider making a profound material test to build a good material model for future simulations of eye tissues. For this purpose, at least the following three tests should be done. The tests are uniaxial tension, biaxial tension and planar shear, which are all presented in the previous table (3). One widely studied and suitable model for capturing the behaviour of the soft tissue could be the Ogden model. It was developed by Dr Ogden in 1972

One aspect which also needs to be taken under consideration, if accurate results wanted, is the anisotropy of the tissue material. From the following figure (68) [61], we can see a second-harmonic image taken by Ing. Daniel Hadraba, PhD. From the image, we can see the collagen fibres running down from the limbus area towards the optical nerve. These fibres are being greatly crosslinked to each other, and this creates the anisotropic nature of the sclera tissue. This crosslinking can be described with the analogy to polymer chains. Just like polymer chains, the collagen fibres tend to lock against each other when the material is exposed to large deformations.

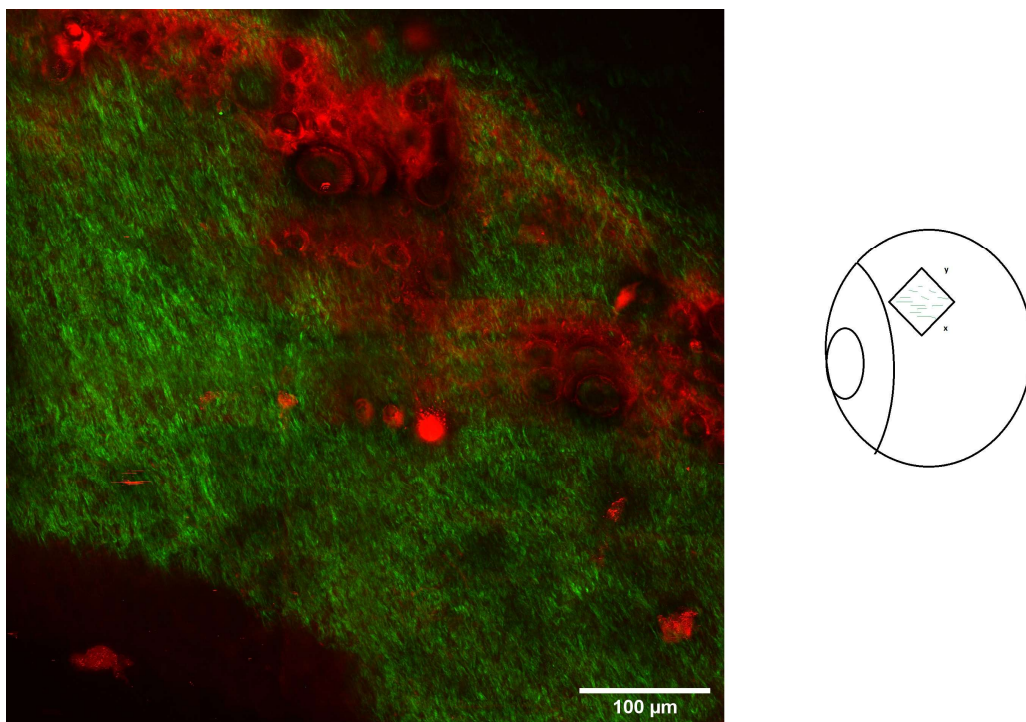


Figure 68. Collagen fibres orientation in the measured eye (Hadraba, Modified)

Almost all commercial FEA programs are providing a platform to create an individual stiffness matrix for the anisotropic materials. In principle, this matrix is rotated with a special transformation matrix to achieve a wanted structure in the material model.

During this work, it was also noted that the surface quality of the GRIN lens was significantly worse than a regular optical fibre with similar dimensions. After a careful discourse with Dr Ivan Kašík from the Czech Academy of Sciences, Institute of Photonics and Electronics. It was found out that with high probability, the flaws on the surface of the GRIN lens was due to the manufacturing process. According to Grintech GmbH, the lenses are produced by drawing from preforms, and the graded-index is done by ion-exchange [8]. Dr Kašík supposed that after this process, the extra silica cover was removed from the lens by etching. This can be done either, chemically where the surface is etched out by using hydrofluoric acid, or mechanically. On the chemical etching, the hydrofluoric acid slowly eats out the glass. This leaves a relatively poor surface quality for the lens which can be recovered, partially, in the drawing process when the fibre is heated again. From the figures (69 & 70), we can see scanning electron microscope images (further SEM) taken from the GRIN lens and a regular, well-aged optical fibre with similar dimensions.

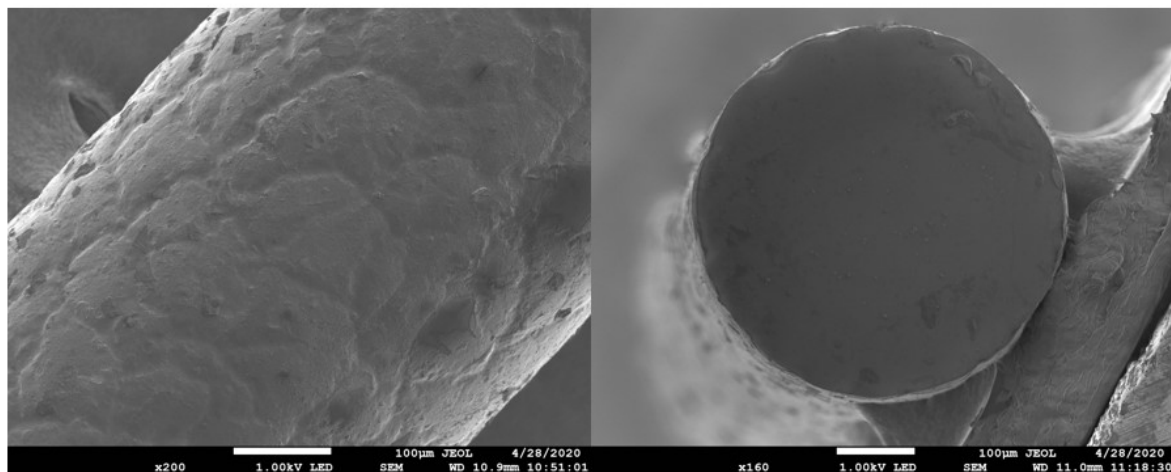


Figure 69. SEM picture of GRIN lens

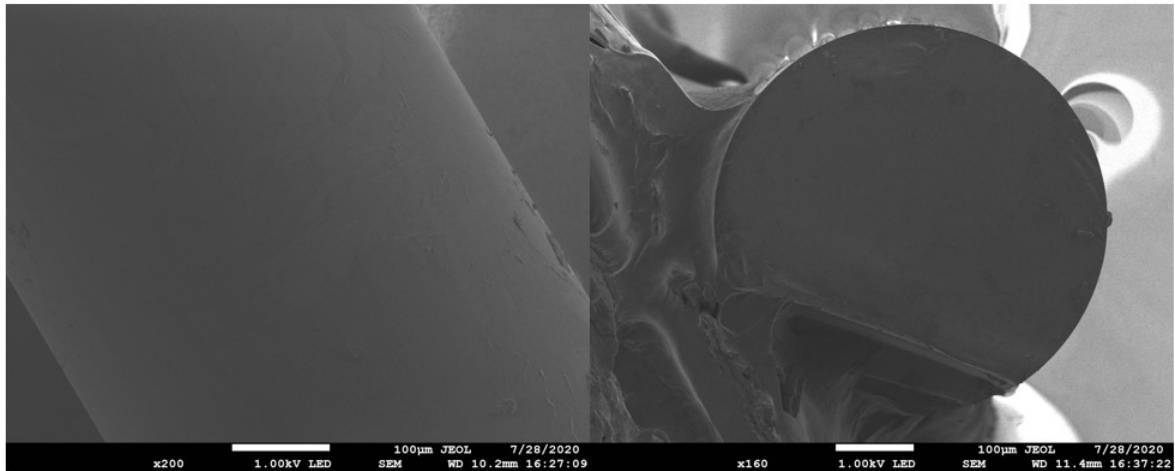


Figure 70. Regular optical fibre in SEM.

According to Dr Kašík, some mechanical testing has been done with freshly drawn fibres in the institute of photonics and electronics and a significant change in the tensile strength between the fibres was obtained. According to him the typical tensile strength of 125 (μm) optical fibre is round 4 (GPa) while fibres, drawn from etched preforms, are typically round 1-2 (GPa). Part of this can be explained by the change in the geometrical properties of the fibre [62]. If the strength of the fibres is looked only in a geometrical point of view, it can be seen that the reduction of the effective diameter by 4 (%) of the total diameter can reduce the ultimate strength by 13 ± 3.4 (%) when compared to the results of Hošek et al. paper [42]. Calculations for this can be found from appendices (Appendix 12)

The quality of the lens surface might affect the static mechanical strength of the endoscope probe. The surface quality is also known to affect the fatigue of the instrument. Therefore, future studies of improving the surface quality of the optical parts of the endoscope are given. This is due to the precautionary principle because the instrument should handle the worst-case scenario loading.

8 References

- [1] Society, Pittsburgh Ophthalmology, “Harvey E. Thorpe, MD,” 2019. [Online]. Available: www.pghoph.org. [Accessed February 2020].
- [2] T. H., “Ocular endoscope: instrument for removal of intravitreal nonmagnetic foreign bodies.,” *Trans Am Acad Ophthalmol Otolaryngol*, vol. 39, pp. 422-424, 1934.
- [3] J. L. Norris and G. W. Cleasby, “An endoscope for ophthalmology,” *Am J Ophthalmol*, vol. 85, pp. 420-422, 1978.
- [4] V. V. Volkov, A. V. Danilov, L. N. Vassin and Y. A. Frolov, “Endoscope for Intraocular Surgery,” *Arch Ophthalmol*, vol. 108, pp. 1037-1038, 1990.
- [5] M. Uram, “Ophthalmic laser microendoscope endophotocoagulation,” *Ophthalmology*, vol. 99, pp. 1829-1832, 1992.
- [6] K. V. Marra, Y. Yonekawa, T. D. Papakostas and J. G. Arroyo, “Indications and techniques of endoscope assisted vitrectomy,” *Journal of ophthalmic & vision research*, vol. 8(3), pp. 282-290, 2013.
- [7] Applied Image Inc., “T-20 USAF 1951 Chart Standard Layout Product Specifications,” [Online]. Available: https://www.appliedimage.com/wp-content/uploads/2017/09/USAF-1951-Test-Target-T-20_v1-04.pdf. [Accessed February 2020].
- [8] Grintech GmbH, “Gradient index (GRIN) lenses,” [Online]. Available: www.grintech.de. [Accessed February 2020].
- [9] Thorlabs Inc, “Single Wavelength Graded-index (GRIN) Lenses,” [Online]. Available: https://www.thorlabs.com/NewGroupPage9.cfm?ObjectGroup_ID=1209. [Accessed February 2020].

- [10] A. r. o. G. G. Kraeplin, Interviewee, *Questions about your product for thesis, email message*. [Interview]. 12 February 2020.
- [11] J. R. Hensler, "Method of Producing a Refractive Index Gradient in Glass". U.S. Patent 3873408A, 25 March 1975.
- [12] M. M. Nemčoková, Interviewee, *Ophthalmological surgery*. [Interview]. 24 January 2020.
- [13] D. A. Atchison and L. N. Thibos, "Optical Models of the Human Eye," *Clin Exp Optom*, vol. 99, no. 2, pp. 99-106, 2016.
- [14] D. A. Atchison and G. Smith, *Optics of the Human Eye*, 1 st. ed., Oxford: Butterworth-Heinemann, 2000.
- [15] S. Vurgese, S. Panda-Jonas and J. B. Jonas, "Scleral thickness in human eyes," *PloS one*, no. 7, 2012.
- [16] E. Custer, "Anatomy of the Eye: Human Eye Anatomy," [Online]. Available: www.owlcation.com/stem/Anatomy-of-the-Eye-Human-Eye-Anatomy. [Accessed February 2020].
- [17] M. J. Turner, R. W. Clough, H. C. Martin and L. J. Topp, "Stiffness and Deflection Analysis of Complex Structures," *Journal of the aeronautical sciences*, vol. 23, no. 9, 1956.
- [18] E. Madenci and I. Guven, *The Finite Element Method and Applications in Engineering Using ANSYS®*, Springer, 2015.
- [19] Autodesk Inc, "Nodes and Elements," [Online]. Available: http://download.autodesk.com/us/algor/userguides/mergedProjects/getting_started/Introduction_to_Algor/Nodes_and_Elements.htm. [Accessed February 2020].

- [20] M. Mäkelä, L. Soininen, S. Tuomola, J. Öistämö and M. Kulmala, Technical Formulas, Tampere: Tammertekniikka (Amk Publishing Ltd), 2013.
- [21] A. Ahmad and V. Genberg, Optomechanical Engineering Handbook, CRC Press LLC, 1999.
- [22] F. Galbusera, M. Freutel, L. Dürselen, M. D'Aiuto, D. Croce, T. Villa, V. Sansone and B. Innocenti, "Material models and properties in the finite element analysis of knee ligaments," *Frontiers in bioengineering and biotechnology*, vol. 2, no. 54, pp. 1-11, 2014.
- [23] A. Ayyalasomayajula, R. I. Park, B. R. Simon and J. P. Vande Geest, "A porohyperelastic finite element model of the eye: the influence of stiffness and permeability on intraocular pressure and optic nerve head biomechanics," *Computer Methods in Biomechanics and Biomedical Engineering*, vol. 19, no. 6, pp. 591-602, 2016.
- [24] Ansys, Inc., Hyperelastic Materials, Ansys, Inc., 2005.
- [25] Ansys, Inc., Ansys Mechanical Nonlinear Materials, Module 04: Hyperelasticity, Ansys, Inc., 2019.
- [26] SimScale GmbH, "How to Choose a Hyperelastic Material Model for Your FEA," 11 March 2020. [Online]. Available: <https://www.simscale.com/blog/2016/06/how-to-choose-hyperelastic-material/>. [Accessed June 2020].
- [27] M. Mooney, "A theory of large elastic deformation," *Journal of Applied Physics*, vol. 11, no. 9, pp. 582-592, 1940.
- [28] R. S. Rivlin, "Large elastic deformations of isotropic materials," *Philosophical Transactions of the Royal Society of London. Series A, Mathematical and Physical Sciences*, vol. 241, no. 835, pp. 379-397, 1948.

- [29] Ansys, Inc., Ansys Mechanical Nonlinear Materials, Appendix 4A: Hyperelasticity, Ansys, Inc., 2019.
- [30] B. McGinty, "Continuum Mechanics," [Online]. Available: <https://www.continuummechanics.org/index.html>. [Accessed February 2020].
- [31] T. Pence and K. Gou, "On compressible versions of the incompressible neo-Hookean material," *Mathematics and Mechanics of Solids*, vol. 20, no. 2, pp. 157-182, 2014.
- [32] A. F. Bower, *Applied Mechanics of Solids*, Boca Raton: Scitech , 2010.
- [33] J. Hošek, *private communication*, Prague, 2019.
- [34] M. M. Penčák, Interviewee, *Material for the Thesis Work*. [Interview]. February 2020.
- [35] Ansys, Inc., Ansys Module 05: Mesh Control, Ansys, Inc., 2017.
- [36] Budapest University of Technology and Economy, Faculty of Mechanical Engineering, "ans_help_v182," 2018. [Online]. Available: https://www.mm.bme.hu/~gyebro/files/ans_help_v182/. [Accessed June 2020].
- [37] Ansys, Inc., Lecture 7: Mesh Quality & Advanced Topics, Ansys, Inc., 2015.
- [38] H. A. Weeber and R. G. Van Der Heijde, "Internal deformation of the human crystalline lens during accommodation," *Acta Ophthalmologica*, vol. 86, no. 6, pp. 642-647, 2008.
- [39] M. I. Kaczurowski, "Zonular Fibers of the Human Eye," *American Journal of Ophthalmology*, vol. 58, no. 6, pp. 1030-1047, 1964.
- [40] J. Šepitka, "Sample Analysis Report," Laboratoř nanoindentačních, Prague, 2014.
- [41] R. Grytz, M. A. Fazio, M. J. Girard, V. Libertiaux, L. Bruno, S. Gardiner, C. A. Girkin and C. J. Downs, "Material Properties of the Posterior Human Sclera," *Journal of the Mechanical Behaviour of Biomedical Materials*, vol. 29, pp. 602-617, 2014.

- [42] J. Hošek and Š. Němcová, “Measurement of mechanical properties of GRIN rod lens,” in *Optics and Measurement International Conference*, Liberec, 2019.
- [43] Alloy Wire International, “Technical Datasheet AWS 100 Rev.1,” Alloy Wire International, Brierley Hill, 2020.
- [44] Becton Dickinson and Company, BD Medical, Technical Data Sheet, BD Microlance 3 hypotermic needle, Eysins: BD Switzerland Sarl, 2017.
- [45] R. Lehman, Introduction to Glass Technology The Mechanical Properties of Glass Specific Strength and Stiffness of Selected Bulk Materials, New Jersey: Rutgers University.
- [46] T. R. Friberg and J. W. Lace, “A comparison of the elastic properties of human choroid and sclera,” *Experimental eye research*, vol. 47, no. 3, pp. 429-436, 1988.
- [47] R. F. Fisher, “Elastic constants of the human lens capsule.,” *The Journal of physiology*, vol. 201, no. 1, pp. 1-19, 1969.
- [48] R. F. Fisher and J. Wakely, “The elastic constants and ultrastructural organization of a basement membrane (lens capsule).,” *Proceedings of the Royal Society of London. Series B. Biological Sciences*, vol. 193, no. 1113, pp. 335-358, 1976.
- [49] E. Uchio, S. Ohno, J. Kudoh, K. Aoki and L. T. Kisielewicz, “Simulation model of an eyeball based on finite element analysis on a supercomputer,” *British Journal of Ophthalmology*, vol. 83, no. 10, pp. 1106-1111, 1999.
- [50] K. E. Hamilton and D. C. Pye, “Young’s modulus in normal corneas and the effect on applanation tonometry.,” *Optometry and Vision Science*, vol. 85, no. 6, pp. 445-450, 2008.
- [51] D. Overby, J. Ruberti, H. Gong, T. F. Freddo and M. Johnson, “Specific hydraulic conductivity of corneal stroma as seen by quick-freeze/deep-etch.,” *J. Biomech. Eng.*, vol. 123, no. 2, pp. 154-161, 2001.

- [52] G. Wollensak, E. Spoerl and T. Seiler, "Stress-strain measurements of human and porcine," *Journal of Cataract & Refractive Surgery*, vol. 29, no. 9, pp. 1780-1785, 2003.
- [53] Ansys, Inc., Module 06: Connections and Remote Boundary Conditions, Ansys, Inc., 2017.
- [54] Ansys, Inc., Workbench - Mechanical Structural Nonlinearities, Ansys, Inc., 2009.
- [55] Ansys, inc., Ansys training manual, Advanced Contact, Ansys, inc., 2005.
- [56] E. W. Weisstein, "LU Decomposition," MathWorld--A Wolfram Web Resource, [Online]. Available: <https://mathworld.wolfram.com/LUDecomposition.html>. [Accessed August 2020].
- [57] EETech Media, LLC., "All about circuits," [Online]. Available: <https://www.allaboutcircuits.com/textbook/direct-current/chpt-9/strain-gauges/>. [Accessed August 2020].
- [58] P. Dokoupil, "Determination of Measurement Uncertainty of Strain and Stress Using Strain Gages," *Transaction of the VSB - Technical University of Ostrava, Mechanical Series*, vol. 63, pp. 9-24, 2017.
- [59] T. W. Olsen, S. Sanderson, X. Feng and W. C. Hubbard, "Porcine Sclera: Thickness and Surface Area," *Anatomy and Pathology / Oncology*, vol. 43, no. 8, pp. 2529-2532, 2002.
- [60] Wikipedia, the free encyclopedia, "Wikipedia, Mooney–Rivlin solid," 27 July 2018. [Online]. Available: https://en.wikipedia.org/wiki/Mooney%E2%80%93Rivlin_solid. [Accessed 19 August 2020].
- [61] D. Hadraba, *Email conversations*, Prague, 2020.
- [62] I. Kašík, *Private communication*, Prague, 2020.

- [63] R. W. Ogden, "Large deformation isotropic elasticity—on the correlation of theory and experiment for incompressible rubberlike solids.," *Proceedings of the Royal Society of London. A. Mathematical and Physical Sciences.*, vol. 326, no. 1567, pp. 565-584, 1972.
- [64] O. H. Yeoh, "On the Ogden strain-energy function.," *Rubber chemistry and technology*, vol. 70, no. 2, pp. 175-182, 1997.

Appendices

Appendix 1. Phynox Data Sheet

1(1)



Chemical Composition			Specifications	Key Features	Typical Applications
Element	Min %	Max %	AMS 5833 AMS 5834 AMS 5876 ASTM F1058 ISO 5832-7 ISO 15156-3 (NACE MR 0175) Designations W.Nr. 2.4711 UNS R30003 UNS R30008 AWS 100	Combination of high strength, ductility and good mechanical properties at ambient temperatures Excellent fatigue life Excellent corrosion resistance in numerous environments Non magnetic Age hardenable (Spring Temper only) Good for sea water applications.	Springs Seal components Medical devices Components for watches Aerospace applications Petrochemical applications Marine engineering
C	-	0.15			
Mn	1.50	2.50			
Si	-	1.20			
P	-	0.015			
S	-	0.015			
Cr	19.00	21.00			
Ni	14.00	16.00			
Co	39.00	41.00			
Mo	6.00	8.00			
Be	-	0.10			
Fe	BAL				

Density	8.3 g/cm ³	0.300 lb/in ³
Melting Point	1427 °C	2600 °F
Coefficient of Expansion	12.5 µm/m °C (20 – 100 °C)	7.0 x 10 ⁻⁶ in/in °F (70 – 212 °F)
Modulus of Rigidity	77 kN/mm ²	11168 ksi
Modulus of Elasticity	203.4 kN/mm ²	29501 ksi

Heat Treatment of Finished Parts					
Condition as supplied by Alloy Wire	Type	Temperature		Time (Hr)	Cooling
		°C	°F		
Annealed	-	-	-	-	-
Spring Temper	Age Harden	520	970	5	Air

Properties				
Condition	Approx. tensile strength		Approx. operating temperature	
	N/mm ²	ksi	°C	°F
Annealed	800 – 1000	116 – 145	-185 to +450	-300 to +840
Spring Temper	1400 – 1900	203 – 276	-185 to +450	-300 to +840
Spring Temper + Aged	1900 – 2200	276 – 319	-185 to +450	-300 to +840

The above tensile strength ranges are typical. If you require different please ask.

Becton Dickinson and Company
BD Medical,
Medication and Procedural Solution

BD Switzerland Sàrl
 Terre Bonne Park - A4
 Route de Crassier 17
 1262 Eysins,
 Switzerland



bd.com

Microlance needles, version March 2017

REGULAR NEEDLES

BD Reference	Description Gauge/Inches	Length	Wall	Color code	Box (units)	Case (units)
302200	27G x 3/4"	19 mm	Regular	Grey	100	5.000
300635	27G x 1/2"	13 mm	Regular	Grey	100	5.000
304300	26G x 5/8"	16 mm	Regular	Brown	100	5.000
303800	26G x 1/2"	13 mm	Regular	Brown	100	5.000
300300	26G x 3/8"	10 mm	Regular	Brown	100	5.000
300400	25G x 1"	25 mm	Regular	Orange	100	5.000
300600	25G x 5/8"	16 mm	Regular	Orange	100	5.000
304100	24G x 1"	25 mm	Regular	Violet	100	5.000
300700	23G x 1 1/4"	30 mm	Thin	Blue	100	5.000
300800	23G x 1"	25 mm	Thin	Blue	100	5.000
301000	22G x 1 1/2"	40 mm	Thin	Black	100	5.000
300900	22G x 1 1/4"	30 mm	Thin	Black	100	5.000
304727	22G x 1"	25 mm	Thin	Black	100	5.000
304432	21G x 1 1/2"	40 mm	Thin	Green	100	5.000
301156	21G x 1"	25 mm	Thin	Green	100	5.000
301300	20G x 1 1/2"	40 mm	Thin	Yellow	100	5.000
304827	20G x 1"	25 mm	Thin	Yellow	100	5.000
301500	19G x 1 1/2"	40 mm	Thin	Ivory	100	5.000
304622	18G x 1 1/2"	40 mm	Thin	Pink	100	5.000
301155	21G x 2"	50 mm	Thin	Green	100	4.000
300094	22G x 2"	50mm	Regular	Black	100	4.000
301900	18G x 2"	50 mm	Regular	Pink	100	4.000

Becton Dickinson and Company
BD Medical,
Medication and Procedural Solution

BD Switzerland Sàrl
 Terre Bonne Park - A4
 Route de Crassier 17
 1262 Eysins,
 Switzerland



bd.com

Microlance needles, version March 2017

1.3 Material

COMPONENT	MATERIAL
Needle Hub	COLOR CODED POLYPROPYLENE
Needle Shield	POLYPROPYLENE
Bonding Agent	EPOXY
Needle	STAINLESS STEEL AISI 304 (Chromium 18-20%; Nickel 8-12%; Manganese 2%; Silicon 1%)
Lubricant	MEDICAL GRADE SILICONE OIL, <0.25 mg /cm ²

1.4 Material of concern

Materials of concern are chemicals or substances that have been identified as having the potential to cause long term effects on humans or the environment.

MATERIAL	COMMENT
Phthalates	No phthalates intentionally added. No DEHP, CAS number 117-81-1, EC number 204-211-0, intentionally added
Latex	The products do not contain natural latex.
Bisphenol A	Bisphenol A (CAS number 80-05-7, EC number 201-245-8) might be found in very low amount (at a concentration inferior to 5ppm) as a residue from the epoxy synthesis processing. Epoxy is used as needle bonding agent.
Substances of animal origin BSE/TSE	BD, Microlance devices utilize very small amounts of tallow or tallow derivatives (e.g. stearates in polymers). Per MEDDEV 2.4/1 Rev. 9 June 2010 and MEDDEV 2.11/1 Rev 2 January 2008, such substances are not considered as derivatives of animal tissues for the purpose of this rule which therefore does not apply.
Polyvinyl chloride (PVC)	The products do not contain polyvinyl chloride

Appendix 3. Probe curvature measurements

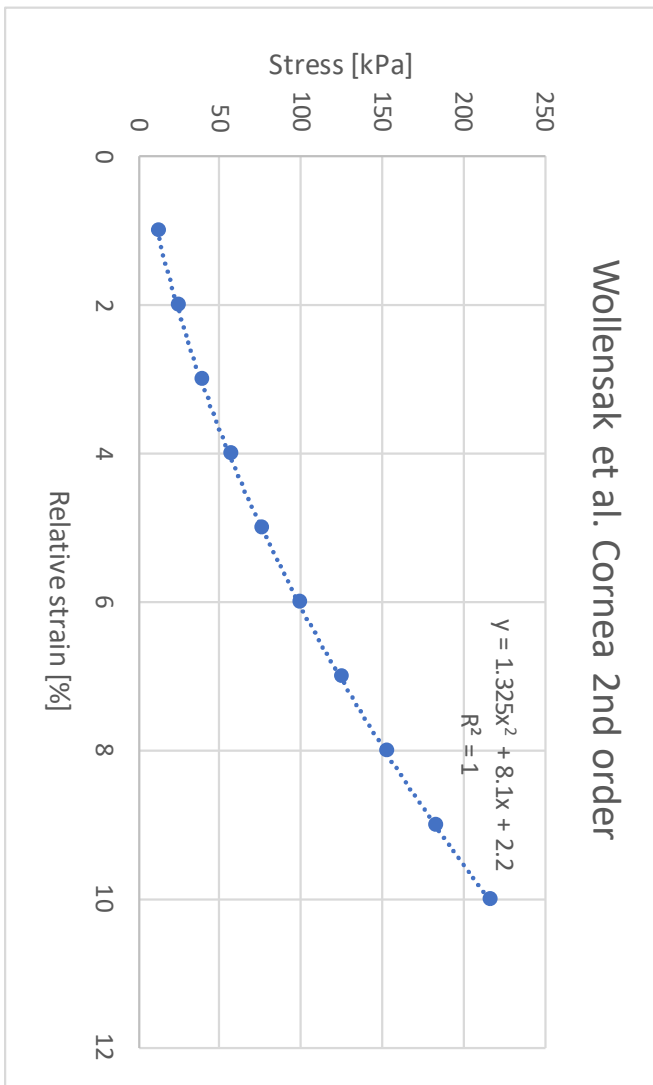
1(1)

	Radius / pix Radius / mm			
1 x: 4899, y: -274, radius:4441	4441	198		
2 x: -6096, y: -38, radius:6813	6813	304		
3 x: 10571, y: -268, radius:10035	10035	447		
4 x: -3334, y: 167, radius:4114	4114	183		
5 x: 3328, y: -77, radius:2791	2791	124		
6 x: -2686, y: 48, radius:3469	3469	155		
7 x: 4696, y: -136, radius:4159	4159	185		
8 x: -1376, y: 80, radius:2158	2158	96		
9 x: 3355, y: -76, radius:2809	2809	125		
10 x: -2442, y: -5, radius:3236	3236	144		
11 x: 4470, y: -114, radius:3920	3920	175		
12 x: -5358, y: 61, radius:6154	6154	274		
13 x: 3763, y: -173, radius:3219	3219	144		
14 x: -3531, y: 64, radius:4327	4327	193		
15 x: 6953, y: -450, radius:6422	6422	286		
16 x: -10144, y: -191, radius:10945	10945	488		
17 x: 3379, y: -92, radius:2828	2828	126		
18 x: -1544, y: 77, radius:2341	2341	104		
19 x: 3753, y: -197, radius:3206	3206	143		
20 x: -2068, y: 105, radius:2868	2868	128		
21 x: 3130, y: -71, radius:2571	2571	115		
22 x: -2353, y: 50, radius:3157	3157	141		
23 x: 2737, y: -24, radius:2175	2175	97		
24 x: -3534, y: -16, radius:4340	4340	193		
25 x: 2845, y: -39, radius:2282	2282	102		
26 x: -2275, y: 5, radius:3083	3083	137		
27 x: 4639, y: -185, radius:4082	4082	182		
28 x: -2142, y: 13, radius:2950	2950	132		
29 x: 3465, y: -193, radius:2910	2910	130 Phynox tube		
30 x: -2331, y: 8, radius:3141	3141	140	Radius / pix	Radius / mm
31 x: 2584, y: -49, radius:2017		2017	2017	90
32 x: -1566, y: 45, radius:2376		2376	2376	106
33 x: 3003, y: -13, radius:2434		2434	2434	109
34 x: -2282, y: 42, radius:3095		3095	3095	138
35 x: 2752, y: 27, radius:2181		2181	2181	97
36 x: -2896, y: 75, radius:3710		3710	3710	165
37 x: 4704, y: -311, radius:4110		4110	4110	183
38 x: -2684, y: -14, radius:3535		3535	3535	158
39 x: 2334, y: -96, radius:1726		1726	1726	77
40 x: -1584, y: 23, radius:2437		2437	2437	109
Average	4031.5333	179.736711	2762.1	123.1419234
SD	2118.8992	94.4662827	799.4659954	35.64236644
Min	2158	96.2095039	1726	76.94977
Max	10945	487.95784	4110	183.234968
FEA	MR.f	MR.c	nH	
	153.38	185.82	191.58	

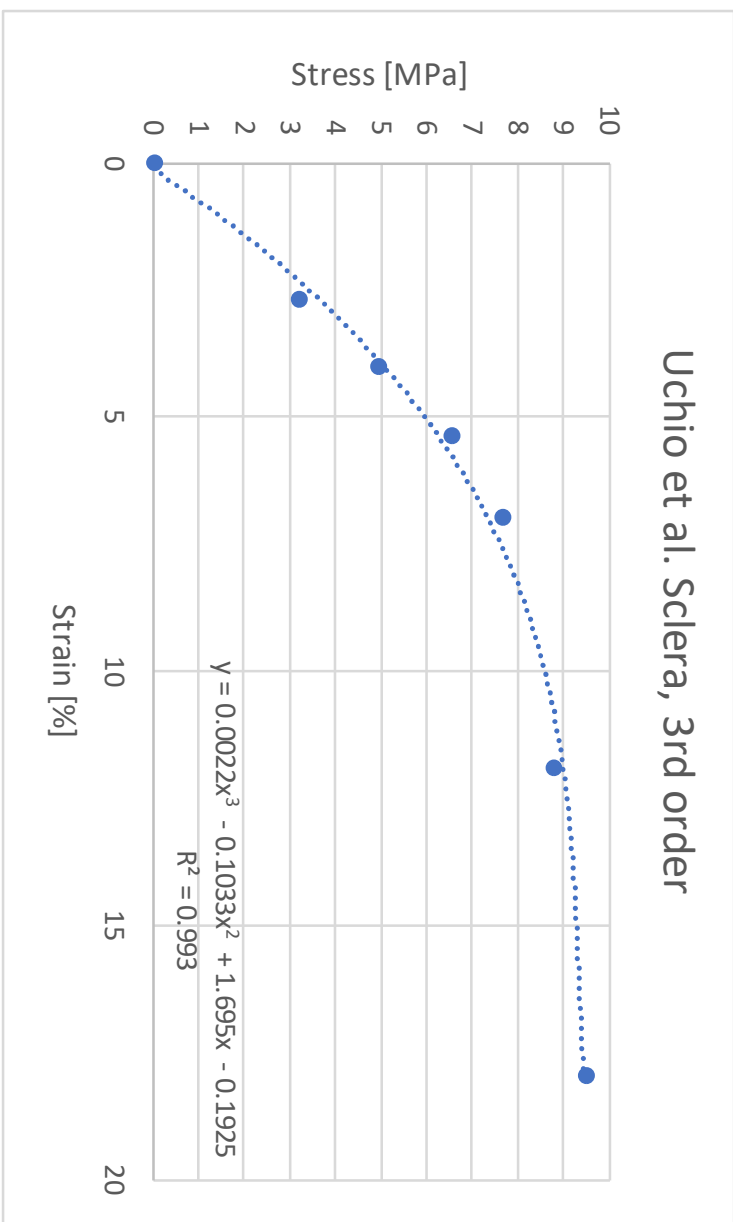
neo-Hookean						
Tissue	Density (kg/m ³)	E (Pa)	Poisson's	C10 (Pa)	D1(Pa ⁻¹)	Source
Choroid	997	600000.00	0.49	100671.14	2.00E-07	[23]
Cornea	997	290000.00	0.42	51056.34	3.31E-06	[49] [50]
Iris	997	9600.00	0.48	1621.60	2.50E-05	[23]
Lamina cribrosa	997	260000.00	0.49	43624.20	4.60E-07	[23]
Lens	997	820000.00	0.47	139455.80	4.40E-07	[47] [48]
Zonule	997	350000.00	0.47	59523.10	1.00E-06	[23]
Post laminar	997	30000.00	0.49	5033.60	4.00E-06	[23]
Sclera	997	2350000.00	0.47	399659.90	1.50E-07	[46] [49]

Literature values	Mooney-Rivlin Density (kg/m ³)	E (Pa)	Poisson's	Lame 1st	B (Pa)	Lame 2nd	C10 (Pa)	C01 (Pa)	G0	D1 (Pa ⁻¹)	G	C10 (Pa)	Source
Choroid	997	600000.00	0.49	9865771.81	10000000.00	201342.28	100671.14	7.42E-10	201342.28	2.00E-07	201342.28	100671.14	[23]
Cornea	997	290000.00	0.42	536091.55	604166.67	102112.68	51056.34	0.00E+00	102112.68	3.31E-06	102112.68	51056.34	[49] [50]
Iris	997	9600.00	0.48	77837.84	80000.00	3243.24	1621.62	1.82E-12	3243.24	2.50E-05	3243.24	1621.62	[23]
Lamina cribrosa	997	260000.00	0.49	4275167.79	4333333.33	87248.32	43624.16	1.82E-10	87248.32	4.62E-07	87248.32	43624.16	[23]
Lens	997	820000.00	0.47	4369614.51	4555555.56	278911.56	139455.78	4.37E-10	278911.56	4.39E-07	278911.56	139455.78	[47] [48]
Zonule	997	350000.00	0.47	1865079.37	1944444.44	119047.62	59523.81	2.33E-10	119047.62	1.03E-06	119047.62	59523.81	[23]
Post laminar	997	30000.00	0.49	493288.59	500000.00	10067.11	5033.56	1.09E-11	10067.11	4.00E-06	10067.11	5033.56	[23]
Sclera	997	2350000.00	0.47	12522675.74	13055555.56	799319.73	399659.86	4.66E-10	799319.73	1.53E-07	799319.73	399659.86	[46] [49]
Trabecular meshwork	997	4000.00	0.35	3456.79	4444.44	1481.48	740.74	0.00E+00	1481.48	4.50E-04	1481.48	740.74	[23]
Uveoscleral pathway	997	4000.00	0.47	21315.19	22222.22	1360.54	680.27	4.66E-12	1360.54	9.00E-05	1360.54	680.27	[23]

Strain [%]	Stress [kPa]
1	11.625
2	23.7
3	38.425
4	55.8
5	75.825
6	98.5
7	123.825
8	151.8
9	182.425
10	215.7



Strain [%]	Stress [MPa]
0	0
2.680784	3.197876
4.010955	4.943583
5.365911	6.514798
6.970703	7.659569
11.93189	8.78661
17.96949	9.487616



Measured			
Position [mm]	0	5	Delta
	25.323	20.241	5.082
	24.788	20.686	4.102
	23.896	19.706	4.19
	24.075	20.597	3.478
	24.075	20.151	3.924
	23.985	20.597	3.388
	24.342	20.151	4.191
	24.877	21.132	3.745
	23.896	19.884	4.012
Mean	24.36189	20.34944	4.012444
SD	0.513785	0.442918	0.496272
Min	23.896	19.706	3.388
Max	25.323	21.132	5.082
FEA			
Deformation, directional +Z [mm]	4.1433	4.3929	4.3789

Strain Gauge measurement uncertainty

Hooke's Law	$\sigma = \varepsilon \cdot E$	
Object modulus of elasticity	$E := 193000 \text{ MPa}$	
Measured stress	$\sigma := 420 \text{ MPa}$	
Calculated strain	$\varepsilon := \frac{\sigma}{E} = 2176.1658 \cdot \frac{\mu\text{m}}{\text{m}}$	
Coverage factor	$k := 2$	From the table
Tolerance	$e_E := 9\% \quad [58]$	
Total tolerance	$Z_{\text{max}} := E \cdot e_E = 17370 \cdot \text{MPa}$	
Distribution	$\chi := \sqrt{3}$	
standard strain uncertainty	$u_\varepsilon := 73.6 \cdot \frac{\mu\text{m}}{\text{m}}$	From the table
Sensitivity coefficient, E	$c_E := \frac{d}{d\varepsilon}(E \cdot \varepsilon) = 193000 \cdot \text{MPa}$	
Sensitivity coefficient, ε	$c_\varepsilon := \frac{d}{dE}(E \cdot \varepsilon) = 2176 \cdot \frac{\mu\text{m}}{\text{m}}$	
Uncertainty, strain	$u_{B\varepsilon} := u_\varepsilon \cdot c_\varepsilon = 14.205 \cdot \text{MPa}$	
Uncertainty, elastic	$u_{BE} := \frac{Z_{\text{max}}}{\chi} \cdot c_E = 21.824 \cdot \text{MPa}$	
Resultant	$u_{B\sigma N} := \sqrt{u_{B\varepsilon}^2 + u_{BE}^2} = 26.04 \cdot \text{MPa}$	
Corrected resultant	$U_{\sigma N} := k \cdot u_{B\sigma N} = 52.079 \cdot \text{MPa}$	
Measurement limits	$\text{Tolerance} := \sigma + \begin{pmatrix} U_{\sigma N} \\ -U_{\sigma N} \end{pmatrix} = \begin{pmatrix} 472.079 \\ 367.921 \end{pmatrix} \cdot \text{MPa}$	

Deflection comparison

Second Moment of Area

Measured

Needle

Phynox

Endoscope

Dimensions:

$$D_n := 0.6414\text{mm}$$

$$D_p := 0.635\text{mm}$$

$$D_e := 0.635\text{mm}$$

$$d_n := 0.337\text{mm}$$

$$d_p := 0.5\text{mm}$$

Needle

$$I_{zn} := \frac{\pi \cdot (D_n^4 - d_n^4)}{64} = 7.675 \times 10^{-3} \cdot \text{mm}^4$$

Endoscope

$$I_{ze} := \frac{\pi \cdot D_e^4}{64} = 7.981 \times 10^{-3} \cdot \text{mm}^4$$

Phynox

$$I_{zp} := \frac{\pi \cdot (D_p^4 - d_p^4)}{64} = 4.913 \times 10^{-3} \cdot \text{mm}^4$$

Maximum deflection

Modulus of Elasticity

Needle

$$E_n := 193000\text{MPa}$$

Phynox

$$E_p := 203400\text{MPa}$$

GRIN

$$E_g := 71600\text{MPa}$$

Load:

$$F_w := 1\text{N}$$

Volume fractions in endoscope probe:

Length:

$$l_w := 16.52\text{mm}$$

Total volume:

$$V_{\text{tot}} := \frac{\pi \cdot D_p^2}{4} \cdot l = 5.232 \cdot \text{mm}^3$$

Diameter of grin lens:

$$D_{\text{grin}} := 0.475\text{mm}$$

Volume of the grin lens:

$$V_{\text{grin}} := \frac{\pi \cdot D_{\text{grin}}^2}{4} \cdot l = 2.927 \cdot \text{mm}^3$$

Volume of phynox tube: $V_{\text{phynox}} := V_{\text{tot}} - V_{\text{grin}} = 2.304 \cdot \text{mm}^3$

Volume fraction of phynox: $V_p := \frac{V_{\text{phynox}}}{V_{\text{tot}}} = 0.44$

Volume fraction of phynox: $V_g := \frac{V_{\text{grin}}}{V_{\text{tot}}} = 0.56$

The rule of mixture: $E_e := E_p \cdot V_p + E_g \cdot V_g = 129651.2 \cdot \text{MPa}$

Maximum deflection

Endoscope $y_{\text{max}_e} := \frac{F \cdot l^3}{3 \cdot E_e \cdot I_{ze}} = 1.452 \cdot \text{mm}$

Needle $y_{\text{max}_n} := \frac{F \cdot l^3}{3 \cdot E_n \cdot I_{zn}} = 1.015 \cdot \text{mm}$

Phynox tube $y_{\text{max}_p} := \frac{F \cdot l^3}{3 \cdot E_p \cdot I_{zp}} = 1.504 \cdot \text{mm}$

Correction factors for deflection

Endoscope $\frac{y_{\text{max}_e}}{y_{\text{max}_n}} = 1.431$

Phynox tube $\frac{y_{\text{max}_p}}{y_{\text{max}_n}} = 1.482$

Maximum stress under point load

Bending stress:

$$W_e := \frac{I_{ze}}{\left(\frac{D_e}{2}\right)} = 0.025 \cdot \text{mm}^3$$

$$W_n := \frac{I_{zn}}{\left(\frac{D_n}{2}\right)} = 0.024 \cdot \text{mm}^3$$

$$W_p := \frac{I_{zp}}{\left(\frac{D_p}{2}\right)} = 0.015 \cdot \text{mm}^3$$

Maximum stress

Endoscope $\sigma_{\text{maxe}} := \frac{F \cdot l}{W_e} = 657 \cdot \text{MPa}$

Needle $\sigma_{\text{maxn}} := \frac{F \cdot l}{W_n} = 690 \cdot \text{MPa}$

Phynox tube $\sigma_{\text{maxp}} := \frac{F \cdot l}{W_p} = 1068 \cdot \text{MPa}$

Correction factors for stress

Endoscope $\frac{\sigma_{\text{maxe}}}{\sigma_{\text{maxn}}} = 0.95$

Phynox tube $\frac{\sigma_{\text{maxp}}}{\sigma_{\text{maxn}}} = 1.55$

Measured 0 s	5 s	Delta	
25.323	20.241	5.082	
24.788	20.686	4.102	
23.896	19.706	4.19	
24.075	20.597	3.478	
24.075	20.151	3.924	
23.985	20.597	3.388	
24.342	20.151	4.191	
24.877	21.132	3.745	
24.431	20.686	3.745	
23.896	19.884	4.012	
Mean	24.4	20.4	4.0
SD	0.5	0.4	0.5
Min	23.9	19.7	3.4
Max	25.3	21.1	5.1
FEA	Deformation Z+		
	MR.f	MR.c	nH
	4.1433	4.3929	4.3789

Appendix 11. Probe reaction forces

1(1)

	Needle (l)			needle (y)							
	16.674					2.14					
	16.496					0.847					
	15.426					0.936					
	15.247					0.49					
	14.891					1.783					
	14.668					0.892					
	15.515					1.605					
	16.139					1.694					
	16.451					2.229					
	16.629			Angle		1.65					
	16.05			28.337		1.872					
	16.094			27.334		0.58					
	16.005			22.226		2.363					
	15.827			22.254		0.936					
	15.247			22.718		1.694					
	15.069			24.216		0.713					
	14.623			23.140		1.783					
	14.489	Phynox (l)		22.490		1.293	phynox (y)				
	15.782	16.005		22.177		2.452	1.382				
	15.47	16.005		21.611		1.115	2.764				
	15.47	15.871		23.676		2.14	1.694				
	15.247	15.559		23.051		1.204	1.516				
	15.069	13.598		23.412		2.185	1.025				
	15.158	14.222		19.339		1.115	1.605				
	15.292	13.999		23.712		2.185	0.847				
	16.273	14.177		19.923		1.605	2.185				
	14.4	16.273		24.960		1.56	1.115				
	13.999	16.585		23.503		1.248	2.452				
	16.005	13.954		22.571		2.853	1.115				
	16.005	14.579		22.179	radians	Needle	Phynox		Phynox	Needle	
Mean	15.507069	15.06892		23.141	0.403894	1.55731	1.609091	E	203400	193000	Mpa
SD	0.6996028	1.074011		2.017757	0.035217	0.612549	0.620777	Iz	0.004913	0.007675	mm^4
Min	13.999	13.598		19.339	0.337529	0.49	0.847	D	0.635	0.6414	mm
Max	16.674	16.585		28.337	0.494574	2.853	2.764	d	0.5	0.337	mm
	Hypotenuse							Force reactions			
Needle	16.864								1.10	1.44	
Phynox	16.387										

Maximum stress on the GRIN lens surface

Maximum bending moment: $M_{\max} := \begin{pmatrix} 1.7 \\ 1.8 \\ 1.9 \end{pmatrix} \text{N}\cdot\text{mm}$ All the initial information from Hosek et al. [42]

Measured diameter: $D := \begin{pmatrix} 0.475 - 0.0047 \\ 0.475 \\ 0.475 + 0.0047 \end{pmatrix} \text{mm}$

Second moment of area: $I_z := \frac{\pi}{64} \cdot D^4 = \begin{pmatrix} 2.401 \times 10^{-3} \\ 2.499 \times 10^{-3} \\ 2.599 \times 10^{-3} \end{pmatrix} \cdot \text{mm}^4$

Position of neutral axis: $y := \frac{D}{2} = \begin{pmatrix} 0.235 \\ 0.238 \\ 0.24 \end{pmatrix} \cdot \text{mm}$

$S_{\max} := \frac{I_z}{y}$ $S = \begin{pmatrix} 0.0102 \\ 0.0105 \\ 0.0108 \end{pmatrix} \cdot \text{mm}^3$

Maximum bending stress: $\sigma_{\max} := \frac{M_{\max}}{S} = \begin{pmatrix} 166.465 \\ 171.077 \\ 175.325 \end{pmatrix} \cdot \text{MPa}$

Reduction in effective diameter: $D_{\text{eff}} := (0.475 - 0.96) \text{mm}$ 4% estimated from the picture with ImageJ

M_{max} = 1.8N·mm Assumed that the maximum moment stays constant.

Reduced second moment of area: $I_{z_{\text{eff}}} := \frac{\pi}{64} \cdot D_{\text{eff}}^4 = 2.122 \times 10^{-3} \cdot \text{mm}^4$

New position of neutral axis: $y_{\text{eff}} := \frac{D_{\text{eff}}}{2} = 0.228 \cdot \text{mm}$

$S_{\text{eff}} := \frac{I_{z_{\text{eff}}}}{y_{\text{eff}}}$ $S = 9.3088 \times 10^{-3} \cdot \text{mm}^3$

New maximum bending stress: $\sigma_{\text{max}} := \frac{M_{\max}}{S} = 193.365 \cdot \text{MPa}$